2008

Study of Capacity Fade of Lithium-Ion Polymer Battery with Continuous Cycling & Power Performance Modeling of Energy Storage Devices

Pedro L. Moss

THE FLORIDA STATE UNIVERSITY

COLLEGE OF ENGINEERING

STUDY OF CAPACITY FADE OF LITHIUM-ION POLYMER BATTERY WITH CONTINUOUS CYCLING & POWER PERFORMANCE MODELING OF ENERGY STORAGE DEVICES

By

PEDRO L. MOSS

A Dissertation submitted to the
Department of Electrical and Computer Engineering
in partial fulfillment of the
requirements for the degree of
Doctor of Philosophy

Degree Awarded:
Spring Semester, 2008

The members of the Committee approve the dissertation of Pedro L. Moss defended on April 11, 2008

Jim P. Zheng
Professor Directing Dissertation

Juan C. Ordonez
Outside Committee Member

Yan Xin
Committee Member

Simon Foo
Committee Member

Hui Li
Committee Member

Approved:

Victor DeBrunner, Chair, Department of Electrical & Computer Engineering

The Office of Graduate Studies has verified and approved the above named committee members.

I would like to dedicate this manuscript to my wife Veronica Moss, my son Pedro Moss Jr. and my daughter Petergail Moss. Veronica thanks for the hard work and dedication to our family while I attend graduate school. Petergail and PJ, I hope lessons I have learned I can pass on to you that you may achieve goals greater than those I aspired for. If you invest in your education, it will remain with you for the rest of your life. My greatest contribution I want to leave to you is to passionately follow your dreams, for in them lies your destiny.

I finally dedicate this manuscript to my mother Rachel Miller, my late grandmother Mable Miller, Harolene Wilkinson, and Myrtis Spenser. Thanks for all the love, nurturing and support that you have given to me throughout my life. Love always.

ACKNOWLEDGEMENTS

With greatest gratitude, I would like to thank the members of my graduate committee Dr. Jim Zheng, Dr. Yan Xin, Dr. Simon Foo, Dr. Hui Li and Dr. Juan Ordonez for their time and service on my committee. I am very thankful to my advisor Dr. Jim Zheng for all the non-academic and academic guidance and support that he has given to me during my graduate studies. This work would not have been completed without the substantial support and involvement of Dr. Jim Zheng and Dr. Yan Xin. Apart from the academic portion of my studies my advisor has given me tremendous personal support for which, with great gratitude I would like to say, thank you. I am very grateful to Dr. Foo for always making himself available for fruitful discussions. Dr. Hui Li has been a great inspiration to me and is a personification of what a great teacher should be like.

I am grateful to Dr. Eric Lochner at the Physics Department at Martech for his time taken to train me on how to use SEM and to take x-ray measurements.

I am thankful to have worked with such great colleagues in the lab, Dr. Xu Wang, Dr. Lenwood Fields, Dr. Author Pun, Dr. Young Wang, and Huazhong Wang.

I would also like to thank Mrs. Alison Stuart in the Office of Financial Aid at Florida State University for making sure that I received the necessary financial support while I completed my studies.

Mr. Eric Sapronetti, Ms. Donna Butka, Mr. Donte Ford, and Ms. Andrea Nelson thank you for your wonderful service to the Electrical and Computer Engineering department.

TABLE OF CONTENTS

LIST OF TABLES

LIST OF FIGURES

ABSTRACT

Thus far, capacity fade has been ascribed to various mechanisms that include (i) the dissolution of highly resistive surface films on the electrode surface which result from side reactions; (ii) loss in active electrode materials; (iii) phase change in the electrode structure; (iv) loss of electrode contact with the current collector that can lead to complete cell failure. If accurate dynamic prediction models for batteries are to be achieved through the incorporation of the mechanisms of capacity fade, it is important to quantify the contribution of capacity fade to each mechanism. To quantify capacity fade to various mechanism to the overall impedance of the cell, we investigate a complete electrochemical cell for morphological change at the electrode/electrolyte interface and the change in electrode structural after prolong cycling using scanning electron microscopy (SEM), transmission line microscopy (TEM), x-ray diffraction (XRD). Analyses were performed using commercial lithium-ion polymer cell UP383562A (Sony Co.). The electrochemical charge discharge performance was studied using conventional galvanostatic/potentostatic techniques. Fitting techniques using an electrical equivalent circuit was applied to the electrochemical impedance spectra (EIS) using the method of non linear least square fitting (NLLS). Parameter evaluations from the equivalent circuit show that with extended cycling there is a large increase in the impedance of the solid electrolyte impedance, charge transfer resistance and ionic impedance. SEM analysis on the individual electrodes shows that during charge-discharge cycling, thick surface films are deposited on the negative (graphite) electrode surface. These surface films including LiF, Li_2CO_3 etc. are known to increase the internal impedance of the cell which result in reduce cell performance. No surface films were observed on the cathode ($Li_{1-x}CoO_2$) electrode surface, however, XRD analysis show the development of some structural defects which are believed to contribute

significantly to the overall increase in cell impedance with continuous insertion and extraction of Li ions.

The equivalent circuit model obtained from the EIS in the frequency domain can be mapped to a time domain equivalent circuit to accurately represent the dc non-linear behavior, dynamic and transient response of the lithium-ion polymer and electrochemical double layer capacitors (EDLC). More importantly, these models demonstrated that an accurate estimation of the power and energy density relationship in terms of Ragone plots can be obtained.

CHAPTER 1

INTRODUCTION

1.1 Background

Modern society has become particularly dependent on portable electronic technologies for both commercial and civilian applications. These devices are required to have the substantial support of electrical energy storage devices, namely, batteries and supercapacitors. During the past century much of the world's energy demands have been met by burning the available fossil fuels such as oil coal and natural gases, with the adverse affects of increase green house gases (e.g. CO_2) that contributes to global warming, severe environmental health impact and significant reduction in sustainable energy supplies. This dependency on fossil fuels, particularly petroleum imports for vehicle transports, pose a grave threat to the national economy in addition to global security [5]. These concerns have spurred significant interest in the development of cleaner and renewable energy sources. The development of diverse applications for portable and stationary energy sources has also resulted in an enormous undertaken to develop energy storage devices with higher volumetric energy and power densities.

One of the main target applications for rechargeable battery technology includes its usage as the main energy source in electric and hybrid electric vehicles to conform to low emission standards set by the government and the zero emission standards set by the states like California [6]. Zero emission electric and ultra low emission hybrid electric vehicles are solutions that can eliminate or significantly reduce pollutants associated with the internal combustion engine. However, much work remain that will assure performance standards for these batteries and that safety guidelines are met.

Much ongoing research and development (R&D) in academia and industry seeks to understand the electrochemical processes and transport mechanisms that led to decrease cycle performance of lithium secondary cells. A significant amount of this research is focused on the interfacial phenomena's at the electrode-electrolyte interface and phase change in the positive electrode material that with continuous cycling, result in increase overpotential voltage which reduce cell performance. A current trend, but not limited to, is to use batteries made with gel polymer electrolytes. The use of polymer electrolyte has several advantages over electrochemical systems made with liquid electrolytes which include, i) a significant reduction in potential leakage that can result serious injury to the user; ii) The ability to attain various cell shapes and geometries. Significant research is focused on new electrode materials with the ability to deliver higher capacity and electrolytes with greater electrochemical stability. However despite all these efforts we have yet to achieve optimum battery performance. This dissertation focus on the long term stability of lithium polymer cells and seeks to identify critical interfacial parameters such as morphology, structure, and compositional change that control cell performance in both positive and negative electrode during continuous charge/discharge cycling. A dynamic battery model is developed from impedance data that is mapped from the frequency domain which can accurately represent the battery/supercapacitor response to constant power demands and varying load currents.

1.2 Dissertation Outline

The focus of this dissertation is to investigate the capacity fade and reduce cell performance in lithium polymer batteries due to various mechanisms. Electrochemical analysis and equivalent circuit modeling is conducted to elucidate the performance characteristic with continuous cycling. Transmission electron microscopy (TEM) and scanning electron microscopy (SEM) analysis are used to understand the morphological change at the electrode/electrolyte interface and the structural changes in the electrode material respectively. An equivalent circuit model is developed to validate the use of ac impedance spectra in the dynamic prediction of battery performance and electrochemical capacitors under various current loads.

Chapter 2 Review various component of the lithium polymer and its effect on performance and storage capability. The most widely used electrochemical structure consist Li_xC_6|salt-Solvent|$Li_{x-1}CoO_2$. Graphite carbon is commonly used as anode due to its relative stability and performance and had a theoretical capacity of 372mAhg^{-1}. Despite the advantageous use of cobalt as cathode material, its limited availability and negative environmental impact will require an alternative replacement.

Chapter 3 focuses on the mathematical analysis of charge transport process using electrochemical impedance spectroscopy and electrical equivalent circuit analogy.

Chapter 4 Simulating the dynamic behavior and power performance of an electrochemical capacitor from EIS spectra. The result shows that a dynamic and accurate model can be ascertained from EIS spectra including the prediction of the optimum energy vs. power relationship for electrochemical double layer capacitors.

Chapter 5 focuses on investigating the kinetics of lithium-ion charge transport using SEM, TEM, XRD and electrical equivalent circuit analysis. From the analysis possible reasons for capacity degradation are suggested.

Chapter 6 presents a dynamic performance of Li-polymer battery which takes into account non-linear electrode characteristics to accurately model electrode diffusion and charge transfer resistance at the electrode electrolyte interface. An equivalent circuit is developed that can accurately describe battery dynamic, transient and power performance.

Chapter 7 Discuss avenues for future research which include investigating mechanisms of capacity fade using NMR spectroscopy, and STRAFI NMR spectroscopy to study Li^+ ion migrations in lithium polymer battery during initial charge/discharge process and during extended charged/discharge cycling.

CHAPTER 2

LITHIUM SECONDARY BATTERIES

2.1 Introduction

A battery is a simple electrochemical device that can efficiently store and convert chemical energy into electrical energy via oxidation-reduction reactions. Alessandro Volta, an Italian physicist, was the first in 1800 to demonstrate and quantify his invention the *voltaic pile,* for which he proved the relationship between chemical reactions and electricity by immersing two distinct metal, zinc and silver disk with cardboard as porous separator in a solution of salt water that resulted was a controlled steady current flowing externally between the two metal electrodes [7-9]. Since Volta's invention, the battery has become an essential part of modern society ranging in application from PDA's, cell phones, lap tops, medical implantations devices, and for future use in hybrid electric vehicles (HEVs) and in aerospace applications, etc. There are two types of battery chemistries, *primary chemistry* and *secondary chemistry*. Cells made with the primary chemistry are used once and discarded which presents the problem of depletion of natural resources as well as the potential for environmental hazards. Cell made with the secondary chemistries are renewable and can provide very good economic and environmental impact. With the increasing dependency on small portable technologies, the demand for power sources with good energy and high volumetric densities that can operate under wide temperature ranges and load conditions with good electrochemical stability will continues to grow.

2.2 Lithium-ion and Lithium Polymer Batteries

Lithium metal for the past few decades has been the most attractive and suitable material for use as anode in the secondary rechargeable battery industry. This demand for lithium metal is attributed to its relatively low electronegativity of standard potential (*-3.045V vs. standard hydrogen electrode*), a high specific capacity of 3860mAh•g^{-1} [10-12] and low energy density, which allow for a very light weight and compact power source. The first commercial utilization of lithium metal as negative electrode for rechargeable batteries led to significant problems with safety and poor cycling performances. Continuous dissolution and deposition of lithium metal led to the formation of dendrites[1] [11, 12] which caused these cells to short circuit resulting in overheating, thermal runaway and poor cycling performance. There were also concerns that abuse of these cells by over charging and over discharging, in addition to compromising the cell structure may lead to serious injuries. The use of lithium metal anode was then quickly abandoned when Sony Corp (Japan) in the early 1990's, introduced the first practical lithium-ion secondary battery that used graphite carbon as anode in a '*rocking chair'* configuration. This new cell structure included a transitional metal oxide such as $LiCoO_2$ as cathode, wherein lithium could be reversibly de-intercalated and intercalated into the crystalline structure forming lithiated graphite intercalation compounds (Li-GIC). This new anode has a reduction potential close to that lithium metal, a maximum theoretical specific capacity of 372mAh•g^{-1} [11], and exhibited excellent cycling performance while avoiding the problem of dendrite formation during lithium deposition-dissolution. Other advantages of using Li-GIC intercalation compounds over pure lithium metal included limiting the rate limiting step to the diffusion of lithium-ion into the porous material. Lithium-ion batteries also have additional advantages over traditional secondary batteries such as Nickel cadmium (Ni-Cd) and Nickel metal hydride (Ni-MH) batteries because of the overall increase energy density, no memory effects and relatively benign environmental impact [10, 13]

---

[1] *Dendrites are "Branch like" lithium structures that extend from anode to cathode through the electrolyte and separator resulting in undesirable safety effects and performance*.

Figure 2.1 show the comparison of various battery chemistries using a Ragone plot, which typically display the energy density and power density relationship between various energy storage devices (ESD). From this plot it can clearly be observed, the high power and energy density makes lithium metal as anode material preferable over traditional battery systems. However, chemistries such as lithium ion (Li ion) and lithium polymer (PLiON) have shown comparable energy and power densities to lithium metal with exceptional stability.

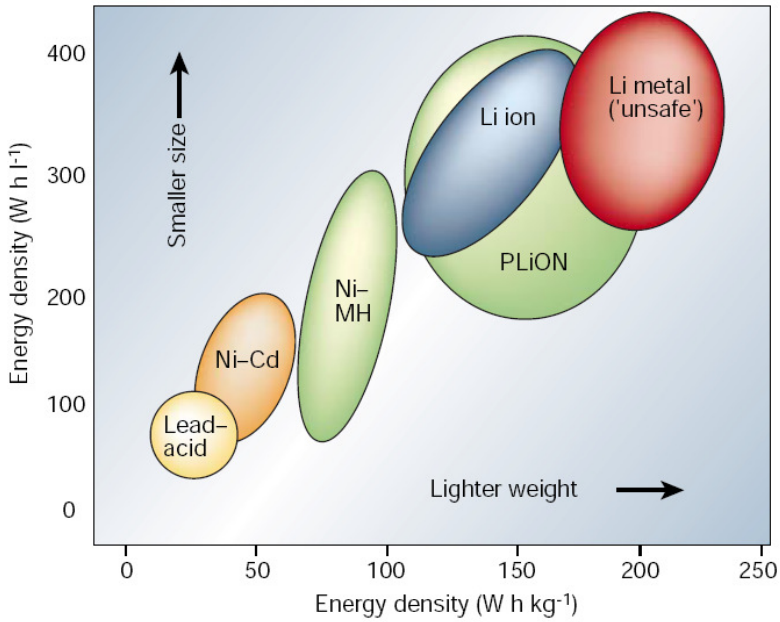

Figure 2.1: The comparison of the energy density and power density for various secondary battery chemistries. Source [1]

Since its commercial introduction, lithium-ion batteries have proliferated in applications ranging from power tools to the small portable electronic dcevices. With the increasing cost for petroleum imports and the ever decreasing availability of fossil fuels in the transportation sector, the need for environmentally friendly and efficient alternative energy sources have been attracting significant attention and will continue over the long term. Figure 3.2 represents the secondary battery sales statistics by volume from Japan [14] for the past two decades. After its commercial introduction lithium-ion battery shows a sharp increase over the years from 29,722 units in 1995 to

1,072,501 units in 2006, largely as the result of the proliferation of cell phones and other portable electric devices.

The current interest is to use Lithium-ion batteries technologies in high powered and high energy density applications such as in the telecommunications industry, military, aerospace, electric vehicles (EVs) and hybrid electric vehicles (HEVs) where extensive cycle and calendar life will be required. The objectives for scientist in research and development (R&D) is to find cathode and anode materials that meets the requirement of low cost, has the ability to delivered much higher specific capacity and energy densities, remain chemically and mechanically stable during high current drain application, work under wide operating temperatures and have prolong service usage with reduce irreversible capacity loss. For EV and HEV applications the USABC (United States Advance Battery Consortium) have set the goals for long term battery performance (Table 2.1) in competition with gasoline powered vehicles [15]. For transportation it is required that HEV's an EV's have a calendar life-time of 15 years and 10 years for the 42V battery systems respectively [16]. These rules were adopted in direct response to the zero emission vehicle (ZEV) standard set by California in 1990. However, before the goal of the full electric vehicle is achieved, where large-scale lithium-ion batteries are required, a comprehensive understanding of the kinetic mechanism of lithium-ion transport that relates to cell safety, efficiency and stability is therefore critical for HEV's and EV's application.

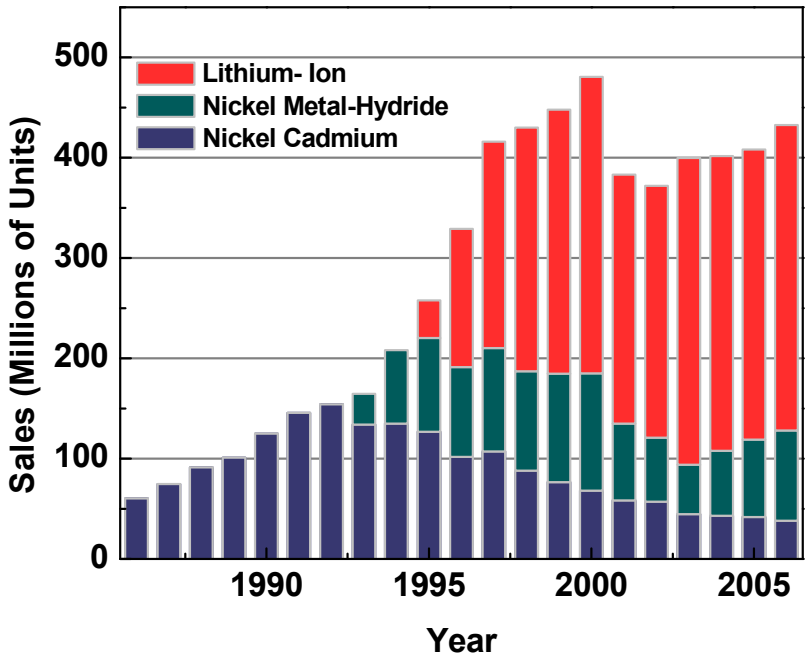

Figure 2.2: The comparison of trend in secondary battery sales exported from Japan from 1986 to 2006.

Figure 2.3 illustrates a schematic representation of a typical secondary rechargeable battery. The porous negative electrode consist graphite carbon (most widely used), filler (carbon black) used to increase the electrode conductivity and binder (PVDF-polyVinylidene difluoride) to attach the electrode to the copper current collector. The positive electrode is usually a lithiated cobolt oxide (Li_xCoO_2) compound with similar construction as the anode but aluminum as current collector. During the assembly process the cell is usually assembled in the discharge state. The electrolyte consist an organic liquid solvent with lithium salt along with microporous separator or polymer electrolytes for which solvent-salt is contain within the polymer matrix [16, 17]. It is known that for lithium-ion batteries the anode electrode is highly reactive to electrolyte solutions which result in the formation of surface films and reduction in cell efficiency. During initial intercalation-deintercalation, it is believed that these films form a solid electrolyte interphase (SEI) layer over the electrode surface that allow for Li^+ ions to intercalate-deintercalnate in "*rocking chain*" mode while simultaneously preventing further dissolution of the electrolyte on the electrode surface . These surface films are

believed to be ionically conductive but at the same time electronically non conductive making them critical in determining cell performance. Continuous dissolution of surface film will eventually lead to increase interfacial impedance resulting in decrease performance.

Table 2.1: USABC objectives for advance batteries for Electric Vehicles [18].

USABC Objective	Mid-term goal	Commercialization	Long-term goal
Specific energy, Wh kg^{-1}	80	150	200
Energy density, Wh L^{-1}	135	230	300
Specific Power, W kg^{-1}	150	300	400
Specific power (regen)	75	150	200
Power density, W L^{-1}	250	460	600
Recharge time	< 6	6 (4 desired)	3 to 6
End-of-life	20% degradation of power and capacity specification	20% degradation of power and capacity specification	20% degradation of power and capacity specification
Calendar life, years	5	10	10
Life, cycle	600@ 80% DoD	1000 @ 80% DoD 1600 @ 50% DoD 2670 @ 30% DoD	1000 @ 80% DoD
Life, urban miles	100,000	100,000	100,000
Ultimate cost, US$/kwh	< 150	< 150 (75 desired)	< 100
Operating environment, °C	-30 to +65	20% loss at extremes of -40 & +50 (10% desired)	-40 to +85
Continuous discharge in 1h (no failure), % rated energy capacity	75	—	75

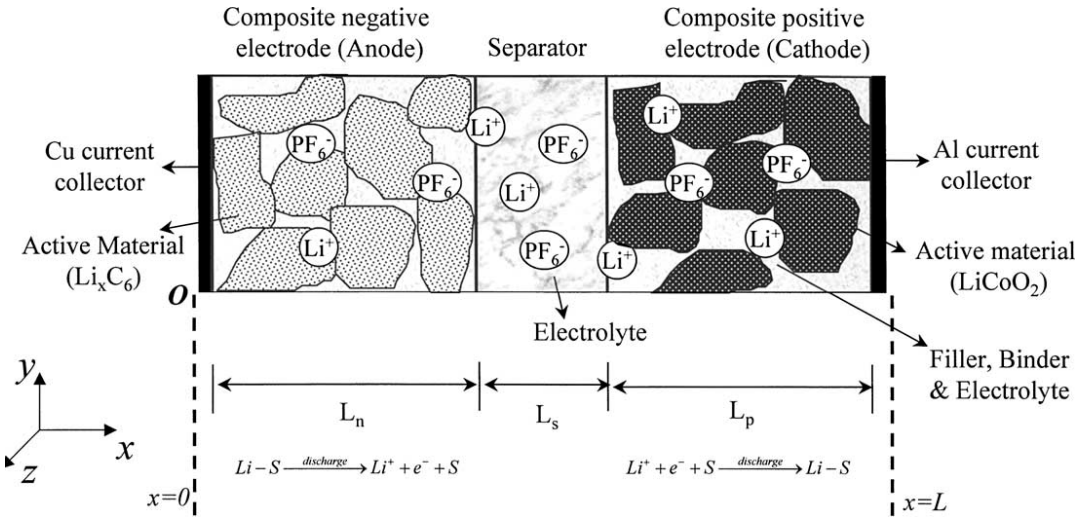

Figure 2.3: Schematic representation of lithium secondary battery. Source [3]

A schematic representation of the charge/discharge mechanism for a lithium-ion battery is illustrated in Figure 2.4. It consists of a positive electrode (Li_xCoO_2), a negative electrode ($Li_{x-1}C_6$) and an ionically conducting electrolyte consisting lithium salt (e.g. $LiPF_6$) in a linear carbonate solution. During the initial discharge state the negative electrode is fully lithiated while actives cites in the positive electrode are available to accept Li^+ ions. Electrons are de-intercalated from the positive electrode (Li_xCoO_2) and pass via external circuit to the anode where they are intercalated between the layered graphene planes. Subsequently Lithium-ions de-intercalated from the metal oxide and travel through the electrolyte and through SEI by migration and diffusion mechanisms. Upon reaching the electrode-electrolyte interphase of the negative electrode, the rate of Li^+ intercalation-deintercalation is governed by concentration polarization and diffusion of lithium into the graphite electrode. The process of intercalation-deintercalation of lithium-ion between the electrodes is term “rocking chair” and is void of lithium platting and stripping that eventually result in dendrite formation. The overall electrochemical reaction can be described by equations (1) - (3).

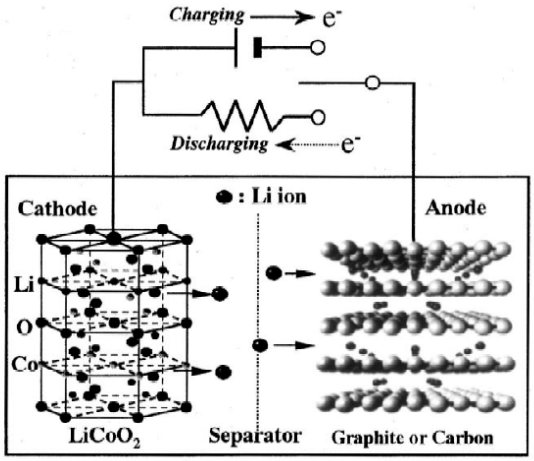

Figure 2.4: Schematic structure and principle of electrochemical operation of Li-ion secondary battery consisting two insertion electrodes during charge/discharge. Source [4]

Anode reaction:

$$6C + xLi^+ + e^- \underset{\text{Discharge}}{\overset{\text{Charge}}{\rightleftharpoons}} Li_xC_6 \quad (1)$$

Cathode reaction:

$$LiCoO_2 \underset{\text{Discharge}}{\overset{\text{Charge}}{\rightleftharpoons}} + Li_{1-x}CoO_2 + xLi^+ + xe \quad (2)$$

The overall cell reaction may be written as:

$$LiCoO_2 + C_6 \underset{\text{Discharge}}{\overset{\text{Charge}}{\rightleftharpoons}} Li_{x-1}CoO_2 + Li_xC_6 \quad (3)$$

2.2.1 Anode Materials

Thus far, graphite carbon is still the only practical anode material for commercial lithium secondary batteries due to its relative good safety, cycling performance, and available structures. Its nearly perfect layered structure allows Li-ions to reversible intercalated/de-intercalate from its lattices structure with a maximum stoichiometric composition of LiC_6. However, graphite anodes suffer from many problems such as material exfoliation and deposition of surface film on the electrode surface [19, 20]. The

microstructure of the anode material, crystallinity, texture and morphology plays a critical role in the anode performance. Thus, several carbonaceous materials have extensively been investigated for use as negative electrode material. They include highly ordered graphite, disordered carbon, soft and hard carbon, meso-carbon micro-bead (MCMB), meso-carbon fiber (MCF), and C-C composite, etc [21].

The crystallographic structure of the most abundant carbonaceous anode material include highly ordered graphite, which consist hexagonal arrangement of carbon atoms arranged in an ABAB…. staking order shown in Figure 2.5. These layered graphene planes along the crystallographic *c-axis* are separated by an interlayer distance of 3.354Å and held together by a weak Van der Waals force. During intercalation, Li-ions are inserted between interlayer of the graphite planes and are aligned between the hexagonal arrays where ionic bonds are form between the layers (as illustrated in Fig. 3.6) [22-24]. Other forms of graphite consist ordering of the less abundant form ABCABC…. which have random translation and rotation between adjacent layers which give rise to the disordered carbonaceous structure [25, 26]. Carbon in its disordered form is also known to intercalate more Li-ions than graphite, resulting in a higher discharge capacity; however these materials suffer poor capacity retention and is not suitable for commercial applications.

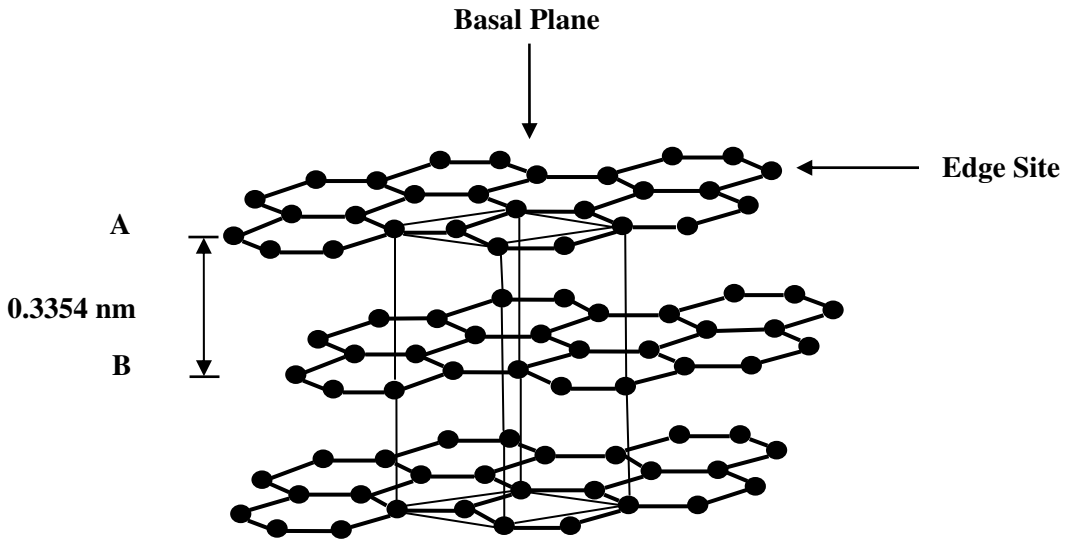

Figure 2.5: Schematic structure and stacking of graphite layer ABAB…

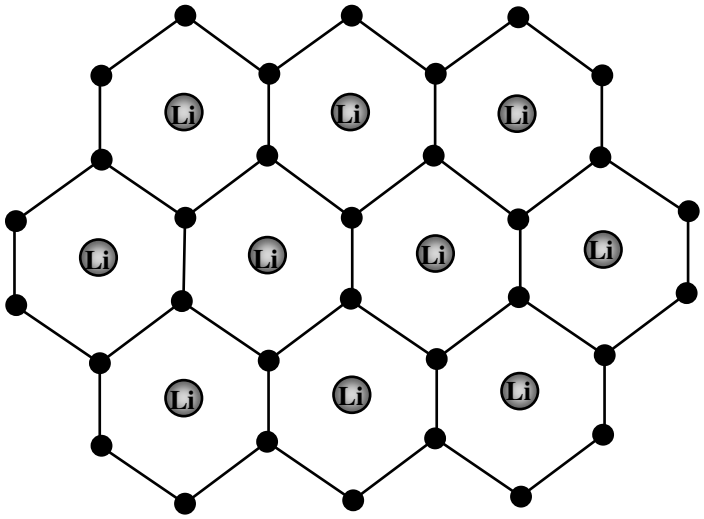

Figure 2.6: Schematic structure and arrangement of Li^+ ions and carbon atom during insertion, LiC_2.

Due to the limited theoretical capacity of 372 $mAhg^{-1}$ for graphite carbon, several alternative anode materials with lower cost and a greater energy storage capability than graphite have been investigated as alternatives. Among the materials are silicon (Si) or tin (Sn) based oxides, nitride and oxides [21]. Thus far, Si has attract the most interest for graphite replacement because of its relatively high theoretical specific capacity of 4200$mAhg^{-1}$ [27] when fully lithiated ($Li_{22}Si_5$). However, during continuous lithiation/de-lithiation poor capacity retention is observed due to large volume expansion and shrinkage that result in crack in material and the lost of electronic contacts [28-31]. In recent reports [31] several authors suggest possible solutions that may improve the overall electrochemical performance of the silicon based anodes including the use of composite material comprising Si-Carbon, Si-Ni-Carbon, and Si-Mn-Carbon. These material shows improve electrochemical performance with cycling.

2.2.2 Cathode materials

Lithium cobalt oxide ($LiCoO_2$) is still the most widely used active cathode material in commercial secondary lithium-ion batteries due to its relative stability, performance and high energy density compared to other cathode materials. The crystal structure,

shown in Figure 3.7, is a layered rhombohedra (R3m space group) structure with Li^+ ion and Co cation occupying alternating edges-sharing sites between oxygen planes [26]. The typical intercalation/de-intercalation of lithiated $LiCoO_2$ in the range 3.0V to 4.2V ($0 < x < 0.5$) resulted in a corresponding maximum reversible capacity of approximately $150mAhg^{-1}$ [22, 26]. Additionally, it has been reported [32] that the layer $LiCoO_2$ structure degrades with additional extraction of lithium-ions from the lattice structure during over charge conditions (Cathode. greater than 4.2V versus Li).

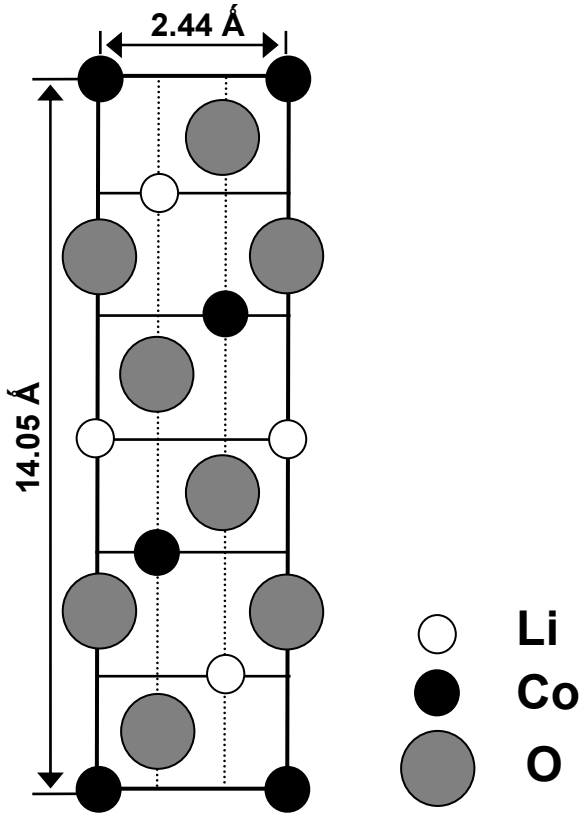

Figure 2.7: Schematic structure of $LiCoO_2$ for lithium-ion batteries, (110) plane.

Due to the cost of cobalt, its limited availability and adverse environmental effects, several alternative materials have been investigated as replacement for cobalt. In particular transitional metal oxides such as lithium-nickel oxide ($LiNiO_2$) [23], lithium-manganese oxide ($LiMn_2O_2$) and several novel structures (e.g. $LiFePO_4$, $FeSO_4$ etc.) have been identify as possible positive electrode replacement. Lithium nickel oxide

($LiNiO_2$) is known to have specific capacity (~200 $mAhg^{-1}$) superior to $LiCoO_2$ (~140 $mAhg^{-1}$) [33]. However, $LiNiO_2$ suffers thermal instability, show significant capacity lost during Li^+ ions insertion/extraction and is costly to synthesize. Phase transition is also known to occur which cause a breakdown in the oxide structure during insertion/extraction of Li^+ ions [34]. Partial substitution of nickel with cobalt has shown improved stability and performance. More recently $LiNi_{0.8}Co_{0.2}O_2$ has been proposed as possible alternative to $LiCoO_2$. Electrode samples prepared via sucrose combustion process show improve cycling stability and a high discharge capacity of 171 $mAhg^{-1}$ [35]. The replacement of Cobalt by Manganese (Mn) is also considered due to several advantageous features: (1) manganese is cheaper and is abundantly available; (2) manganese is environmentally benign. However $LiMn_2O_2$ suffers from low energy density (150-160 $mAhg^{-1}$) [36, 37] as well as cycling and structural instability with temperature and storage [38]. Mn readily dissolves in electrolyte solution due to the reaction with hydrofluoric acid (HF) which result from reactions between $LiPF_6$ salt and trace water [39]. Some solutions that has been proposed to enhance cycling stability include coating the electrode with ZrO_2 [38] or ZnO [40] which act to neutralize HF in electrolyte solutions.

2.2.3 Electrolytes

For effective operation and stability of lithium-ion batteries requires electrolyte solution consisting linear combination of alkyl carbonates including organic solvents of ethylene carbonate (EC), propylene carbonate (PC), Dimethyl carbonate (DMC), diethyl carbonate (DEC), ethyl-methyl carbonate (EMC) etc. [41-43] and commonly used $LiClO_4$ or $LiPF_6$ as electrolyte salt. The electrolyte solution should have good ionic conductivity, have low electronic permittivity to prevent self discharge and remain stable over a wide potential widow. Additionally EC is a necessary component because of its thermal stability and its ability to form an effective protective surface film over the negative anode (graphite) to protect it from further reduction by the electrolyte. Hence, Li^+ ion insertion and the stability of graphite anode in salt solution is strongly dependent on the composition of the electrolyte solution [44].

The long term object is to replace the liquid electrolytes with solvent free polymer electrolytes with the benefits of increase specific power and energy in addition to increase safety, low processing cost and added designs flexibility [45, 46]. Several material including poly(Methyl Methacrylate) (PMMA), Poly(Vinylidene Fluoride) (PVDF), Poly(acrylonitrile) (PAN) and Poly (ethylene oxide) (PEO) has been investigated as polymer matrix [47]. Polymer electrolytes can further be classified into two groups, solid polymer electrolyte (SPE), plasticized or gel polymer electrolyte (GPE) where in; (1) solvent and polymer matrix are mixed to form a single composite homogenous phase; (2) Solvent is non-homogeneously maintained within the polymer matrix [47]. The polymer electrolyte serves both as an ionic conductive path for Li^+ ions transport as well as an electronic separator between the anode and cathode. Other advantageous properties include systems that are void of electrolyte leakage and that are non-flammable. Some remaining issues to be solved with polymer electrolytes [48] include decrease ionic conductivity (10^{-8} to 10^{-5} S cm^{-1}) at ambient temperature [49] compare to liquid electrolytes (10^{-3} to 10^{-2} S cm^{-1}) [50] and small Li^+ transference number (i.e. high transference would lead to high power densities). Despite some short comings the potential advantaged that the used of polymer electrolyte offers for electrochemical systems make them the mostly likely choice for the next generation of power sources. Many additional works in literature [43, 46, 49, 51, 52] can be found on the characterization novel polymer electrolyte for solid state lithium-ion batteries.

2.2.4 Capacity Degradation

Capacity fade with continuous charge-discharge cycling and storage is a major problem that greatly influences the performance of lithium-ion secondary batteries. The capacity loss can be attributed to various mechanisms which include; (i) the increase in interfacial impedance resulting from the precipitation of reduce species on the electrode surface or oxidation of the positive electrode [53]. An additional consequence of this process is the consumption of cycleable Li^+ ions. It is believed that this interaction continues throughout the life of the cell and is responsible for increase irreversible capacity loss with cycling, reduce rate capability and increase over-potential which contributes significantly to the variation in the voltage plateau during charge-discharge;

(ii)The Expansion in the graphite crystalline structure as a result of electrode exfoliation which is associated with the co-intercalation of solvent species between the graphite layers that can destroy the layered structure; (iii) temperature, which plays a critical role in the stability of SEI; (iv) over charge/discharge and charge/discharge rates, which is associated with accelerated capacity loss. Therefore, capacity fade greatly limits the long range performance and application of lithium-ion batteries [54].

Kumaresan et al [55] investigated the cycling performance with temperature for lithium-ion cell with consist lithium cobalt oxide ($LiCoO_2$) as cathode and meso-carbon micro-bead (MCMB) as anode. The electrolyte consist $LiPF_6$ salt in solvent mixture EC, PC, EMC and DEC. The initial charge and discharge capacity increased with increasing temperatures from 5° to 35° C and decrease from 35° to 45° C. The capacity with cycling however is observed to accelerate significantly with temperatures greater than 25° C. After 500 charge/discharge cycles, SEM analysis on the electrodes show minimal change in surface morphology for the cell cycled at 25°C, however the cells that were cycled at temperatures 35° C and 45° C show significant morphological changes on the anode surface. At elevated temperatures the SEI losses its passivation resulting in further reaction between the lithiated carbon electrode and the electrolyte. Arbach et al [56] used Fourier Transform Inferred (FTIR) spectroscopy to study the surface chemistry of graphite in a variety of solution and conclude that a major constituent of these films include $(CH_2OCO_2Li)_2$, Li_2CO_3, and LiF etc. [57] used in-situ ellipsometry, AFM and Roman spectroscopy to characterize SEI formation on different carbonaceous structures. This study show that the structure and morphology of SEI is dependent on the carbonaceous structures and varies significantly with Li^+ ion intercalation.

Zane el al [58] have studied the morphological change on the graphite electrode in contact with various electrolyte solutions containing $LiPF_6$ as salt and EC/PC-DEC or EC/PC-DEC as solvent mixture. It was demonstrated that the formation and stability of SEI is highly dependent on solvent-salt combination. The development of a highly unstable film is formed on the graphite electrode with PC as the main solvent; however, at elevated temperatures good performance can be achieved. From EIS analysis a strong correlation between the thickness of surface films and an increase in cell

impedance is observed which will then result in the hindrance of lithium-ion transport through SEI.

Murphy et al. [59] investigate the cycling performance at a high charge-discharge rate of 1C (i.e. the C-rate defines current which the battery can maintain before becoming completely discharged in hrs) for commercial prismatic cell UF653467 using XRD, TEM (transmission electron microscopy) and SEM (scanning electron microscopy). It was shown using EIS spectra analysis that the cell comprised an inductive component relating to the mechanical properties of the cell design, medium to low frequency semi circles that can be ascribe to SEI and the charge transfer process respectively and a π/4 incline which represent the solid state diffusion process. It was shown that after 286 charge-discharge cycles the low frequency semi-cycle increased in size. SEM analysis on the individual electrodes show no observable morphological change on the cathode with increase cycling, however, cracks were observed on some $LiCoO_2$ particles which was ascribe to strain induced by volume changes. SEM on the graphite anode however, showed the growth of thick surface films with continuous cycling which covered the anode surface. XRD analysis on the cathode show that the characteristic peaks did not change with cycling indicating no new phase was introduced; however the relative intensity of the peak between the (003) and (101) had decreased indicating some structural modification to $LiCoO_2$ with continuous cycling. TEM analysis reveal that the well layered $LiCoO_2$ became disordered .Therefore it was concluded that the main reason for capacity fade with cycling includes electrolyte reduction on the anode surface and change in the structural properties of the cathode.

2.3 Conclusion

Lithium secondary batteries are expected to play a leading role as alternative energy source due to the increase demand and limited supply of available traditional energy sources such as fossil fuels. Before lithium secondary batteries can be considered as a viable alternative energy source to fossils fuels, new cathode and anode materials with superior specific energy and power densities compared to conventional electrode materials are required. Additional issues will also have to be

addressed in regards to environmental concerns and safety characteristic as it related to the scaling-up of cells for electric and hybrid vehicle applications.

CHAPTER 3

ELECTROCHEMICAL CHARACTERIZATION

3.1 Electrochemical Impedance Spectroscopy

Electrochemical impedance spectroscopy (EIS) is a non-destructive analytical technique that allows for the characterization of many complex non-linear electrochemical processes under a variety of conditions (e.g., Temperature, pressure, etc) using relatively simple equivalent electrical circuits (e.g., resistors, capacitors, inductors). The analysis involves the linear excitation of the electrochemical process by application of a small sinusoidal stimulus voltage or current [60].

$$\Delta E(\omega) = \Delta E_{max} e^{j\omega t} \tag{3.1}$$

Then output is a current response that can be given by:

$$\Delta I = \Delta I_{max} e^{j(\omega t + \phi)} \tag{3.2}$$

Where ω is the angular frequency and is ϕ the phase difference between the voltage and current. The equivalent complex impedance with real and imaginary components can then be determined by:

$$Z(\omega) = \frac{\Delta V}{\Delta I} = \frac{\Delta V_{max} e^{j\omega t}}{\Delta I_{max} e^{j(\omega t + \phi)}} = Z' + jZ'' \tag{3.3}$$

And the phase angle is given by:

$$\phi(\omega) = \tan^{-1}\left(\frac{Z''(\omega)}{Z'(\omega)}\right) \tag{3.4}$$

Where, ΔV_{max} and ΔI_{max} are the magnitude voltage and current respectively. The applied current or voltage amplitude in the system tends to show a strong non-linear response. However, when the signal amplitude is less than a defined thermal value, a strong linear relationship between the stimulus input and output is observed [61]. The measured linear current or voltage response can then plotted on a complex plane with real and imaginary components Z'(real) and Z''(imaginary); Here, the components are also a function of frequency. Equivalently Bode plots can also be used to plot absolute impedance ($Z=|Z' + Z''|$) or phase as a function of frequency. The advantages of using EIS are that the equivalent circuit models derive from data collected from EIS can reveal technique insights into the kinetics of mass or charge transport process, such as the Faradaic charge transfer reactions at the electrode-electrolyte interface, diffusive properties of the porous electrodes and surface films as well as the overall cell impedances [62]. The disadvantages of this technique is the ambiguity in the equivalent circuit models that fitted well to the spectra data which may result in incorrect interpretations of the resulting electrochemical process, therefore, careful consideration should be taken in application of circuit elements to a known electrochemical phenomena.

3.1.1 Ohmic Polarization

A steady external flow of current is maintained between the anode and cathode of a battery by the movement of ion in the electrolyte subjected to an electric field when a potential gradient exist between the electrodes. The constant of proportionality between the ionic current and voltage measured in resistance is given according to ohm law [63]:

$$\eta_{ohm} = \phi_{work} - \phi_{ref} = \int_{RE}^{WE} d\phi = -\int_{RE}^{WE} \frac{idx}{\kappa(x)} = \int_{WE}^{RE} \frac{Idx}{\kappa(x)A(x)} \tag{3.5}$$

Where, $\kappa(x)$ is the conductivity of solution in contact with the electrolyte and $A(x)$ is the cross-sectional area of the electrode. When conducting impedance spectroscopy the total real impedance R_s is observed at the intercept of the real axis and can be ascribed to:

- The electrolyte, Porous separator
- Battery contacts,
- Bulk electrode material which include inter-particle binder
- The electronic contacts of the anode and the cathode.

3.1.2 Activation Polarization

Activation polarization is associated the slow kinetic rate of charge transfer at the electrode|electrolyte interface and is denoted by η_{act} . Consider the charge-transfer at the electrode electrolyte interface in which oxidation-reduction occurs.

$$O(soln) \underset{\pm ne^-}{\longleftrightarrow} R(soln) \tag{3.6}$$

The kinetic rate for this reaction is governed by the Butler-Volmer relationship for exchange current density for reduces species according to the following equations below [64]:

$$i = i_0 \left[\exp\left(\frac{\alpha n F}{RT} \eta_{act} \right) - \exp\left(\frac{-(1-\alpha) n F}{RT} \eta_{act} \right) \right] \tag{3.7}$$

$$i_{ox} = i_0 \exp\left(\frac{\alpha n F}{RT} \eta_{act} \right) \tag{3.8}$$

$$i_{rd} = i_0 \exp\left(\frac{-(1-\alpha) n F}{RT} \eta_{act} \right) \tag{4.9}$$

Here, i_0 is the exchange current density, α is the transfer coefficient, n is the number of electrons participating in the reaction, F is faradiac constant, R is the gas constant, T is the absolute temperature and η_{act} is the over potential which is given by:

$$\eta_{act} = \Phi_1 - \Phi_2 - U_{ref} \tag{3.10}$$

Figure 3.1 is a plot of the exchange current density and the activation polarization. Notice that when a low stimulus voltage is applied there is a linear relationship between the current response and the applied stimulus voltage. This region of linear polarization can be approximated (equation 3.7) after a series expansion of equation (3.3). Taking only the first terms result in the following approximation.

$$\eta_{act} \approx \frac{RT}{nF}\left(\frac{i}{i_0}\right) \tag{3.11}$$

Taking the derivative of the activation potential with respect to the exchange current result in the following equation [65].

$$\frac{d\eta_{act}}{di} \approx \frac{RT}{nFi_0} = R_{ct} \tag{3.12}$$

Where R_{ct} is known as the intrinsic charge transfer or faradiac resistance and is indicative of the kinetic rate of charge transfer reactions.

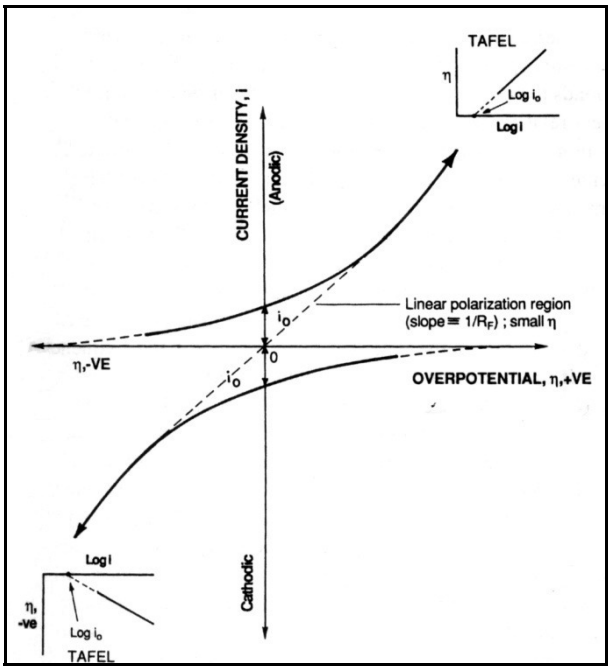

Figure 3.1: Exchange current density vs. activation polarization. Source [66]

3.1.3 The Double Layer Capacitance

Consider a metal electrode in contact with an electrolyte where the electrode remains un-reactive (i.e., Void of deposition and adsorption). The electric charge in the electrode matrix will then be distributed near the electrode surface opposite to charge in the solution phase for which an electric field is established in conjunction with a spatial distribution of oppositely charged ions in the electrolyte; this accumulation of apposing charge at the metal|solution interface is separated on the order of several angstrom [67]. The electrons involved in this process are conductive band electron within the active electrode material, however, when faradaic reactions are involved the electron are attributed to redox reaction.

The Conceptual representation of the electric double layer capacitor (EDLC), Fig 3.2, was purpose by Von Helmoholtz in 1879 [67-69]. Von Helmoholtz's model of the EDLC assumed that excess or deficiency of charge in the electrode is opposed by complementary charge in the electrolyte resulting in linear potential gradient ψ_s, some distance from the electrode and having profile similar to that of a traditional parallel plate

capacitor. The capacitance of the double layer C_{dl} would then be given by the following formula:

$$C_{dl} = \varepsilon_0 \varepsilon_r \frac{A}{d} \tag{3.13}$$

Where, ε_0 is the permittivity of free space, ε_r is the relativity permittivity of the dielectric material that separates the charge in the electrode from the charge in the electrolyte, A is the surface area and d the distance between the opposing charge. However, Gouy and Chapman argued that ions in the electrolyte are not statically distributed as in the Von Helmoholtz's model but should include effects from fluctuates due to thermal vibration [67] according to Boltzmann's and Poisson's (PB) equations of energy and charge distributions respectively. The thermal fluctuation can be characterized by Poisson-Boltzmann distribution [70-74] which in one dimension takes the form of the following equation:

$$\rho(x) = \sum z_i F c_i = \sum z_i F c_i^0 \exp\left(\frac{-z_i F \Psi(x)}{RT}\right) \tag{3.14}$$

Here, $\rho(\mathrm{x})$ is the local volumetric charge density and $\psi(\mathrm{x})$ the potential profile in the solution which is given by:

$$\frac{d^2\Psi(x)}{dx^2} = -\frac{1}{\varepsilon\varepsilon_0} \sum z_i F c_i^0 \exp\left(\frac{-z_i F \Psi}{RT}\right) \tag{3.15}$$

From equation (4.11) the diffuse layer capacitance dependency on potential is characterized as:

$$C_{diff} = \left[\frac{2z^2F^2\varepsilon_r\varepsilon_0 c_i^0}{RT}\right]^{1/2} \cosh\left(\frac{zF\Psi_0}{2RT}\right) \tag{3.16}$$

Here, ε_r is the dielectric constant within the bounded region. Gouy introduce the point charge model (Figure 3.3a), which consider this fluctuation in determining the double-layer capacitance. However, this model failed to predict the correct potential profiles in addition to the prediction of capacitance that was too large. This then led to an accurate interpretation of the double-layer capacitance purposed by stern (Figure 3.3b) in 1924 [66], which combined in series the compact Helmoholtz layer having capacitance C_H and a diffuse Gouy-Chapman layer having capacitance C_{diff}. The total double layer capacitance C_{dl} would then be given by:

$$\frac{1}{C_{dl}} = \frac{1}{C_H} + \frac{1}{C_{diff}} \tag{3.17}$$

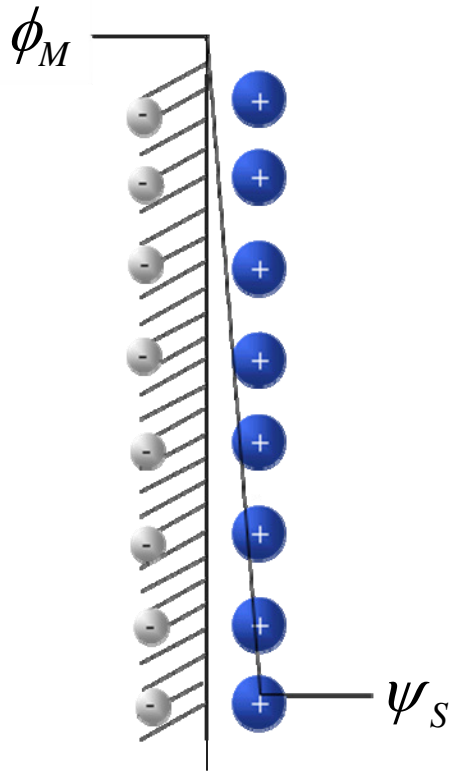

Figure 3.2: Conceptual representation of the Helmholtz double layer apacitance with potential difference at the metal|solution interphase

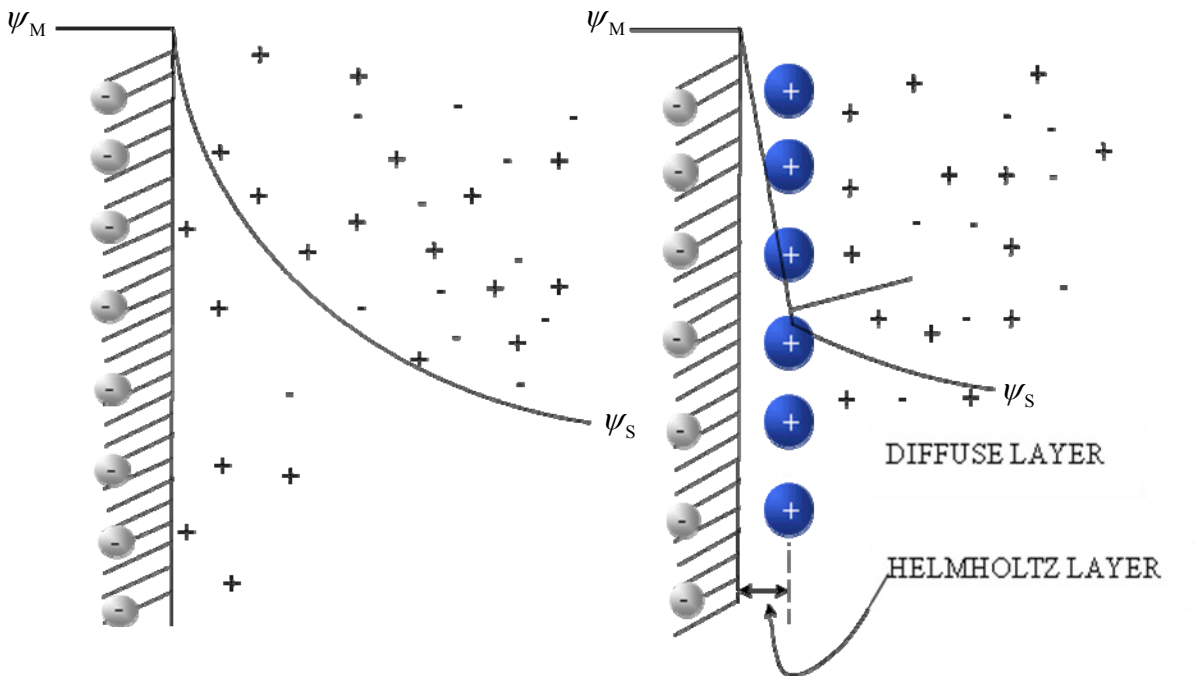

Figure 3.3: (a) Gouy point-charge model, (b) Stern model for finite size with thermal distribution, combining Helmholtz and Gouy models

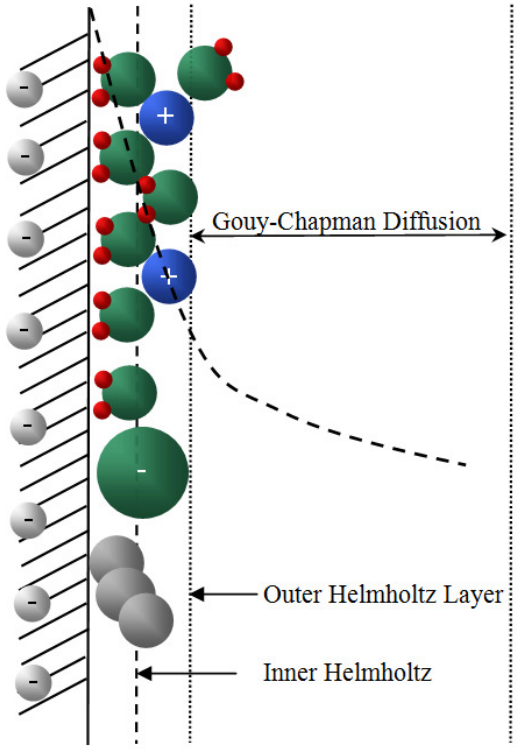

Figure 3.4: General representation of the structure of the double layer showing different regions for adsorption of hydrated cations and less hydrated anions (Grahame model), together with solvent molecules and an adsorbed neutral molecule

3.1.4 Solid Electrolyte Interphase (SEI)

The most commonly used secondary battery composes graphite carbon as anode and $LiCoO_2$ as cathode material in contact with liquid, polymer or gel electrolytes [75]. The electrolyte includes $LiPF_6$ salt in a mixture of alkyl carbonate which requires ethyl carbonate (EC) for stability and linear combination of dialkyl carbonates (DMC, DEC and EMC) to improve the conductivity of the electrolyte [44, 76]. It has been well established that the successful use of lithium metal or carbonous materials as negative electrode in secondary batteries involve *(i)* the passivation of the electrode in contact with liquid or polymer electrolyte by surface films that conduction lithium-ions while inhibiting the conductions of electrons and solution species [26]; *(ii)* have high Lithium-ion conductive properties to limit overpotential polarization; *(iii)* adhered well to the electrode while remaining insoluble in the electrolyte [77]. During the first intercalation/de-intercalation process, Lithium-ion along with solvated ion in the electrolyte reduces to form SEI. Further reduction is hindered when SEI is thick enough to prevent the tunneling of electrons [78]. Therefore, SEI plays the critical role in determining the safety, cycle life, stability and coulombic efficiency of the electrochemical cell.

It is well known that in contact with liquid or polymer electrolyte the anode (e.g. graphite, lithium) is covered with surface films that protect it from corrosion by the electrolyte, Figure 3.5(a). The nature of SEI include a very complex multi-layer structure with varying composition and properties that is composed of soluble and insoluble products of the electrolyte [75]. Previous tools used to investigate the structure and composition of the solid electrolyte interface include Fourier transform infrared (FTIR) spectroscopy, X-Ray Photoelectron spectroscopy (XPS) and atomic force microscopy (AFM) and the results have shown that the solid electrolyte interface include many insoluble products including $(ROCO_2)Li_2$, Li_2CO_3, Li_2O, LiOH, LiF, ROLi, alkoxide and polymer, where R is CH_2 or C_2H_5 depending on the composition of the electrolyte [47, 78].

To gain insight in to complex phenomena of migration Li-ion through SEI, an equivalent circuit below represented by the “voigt-type” element is generally suggested.

The circuit model represents the multilayer surface films that include R_A, R_B, and R_C which represents the ionic Resistance of the microphase and C_A, C_B, C_C the corresponding capacitance of each sub layer [79].

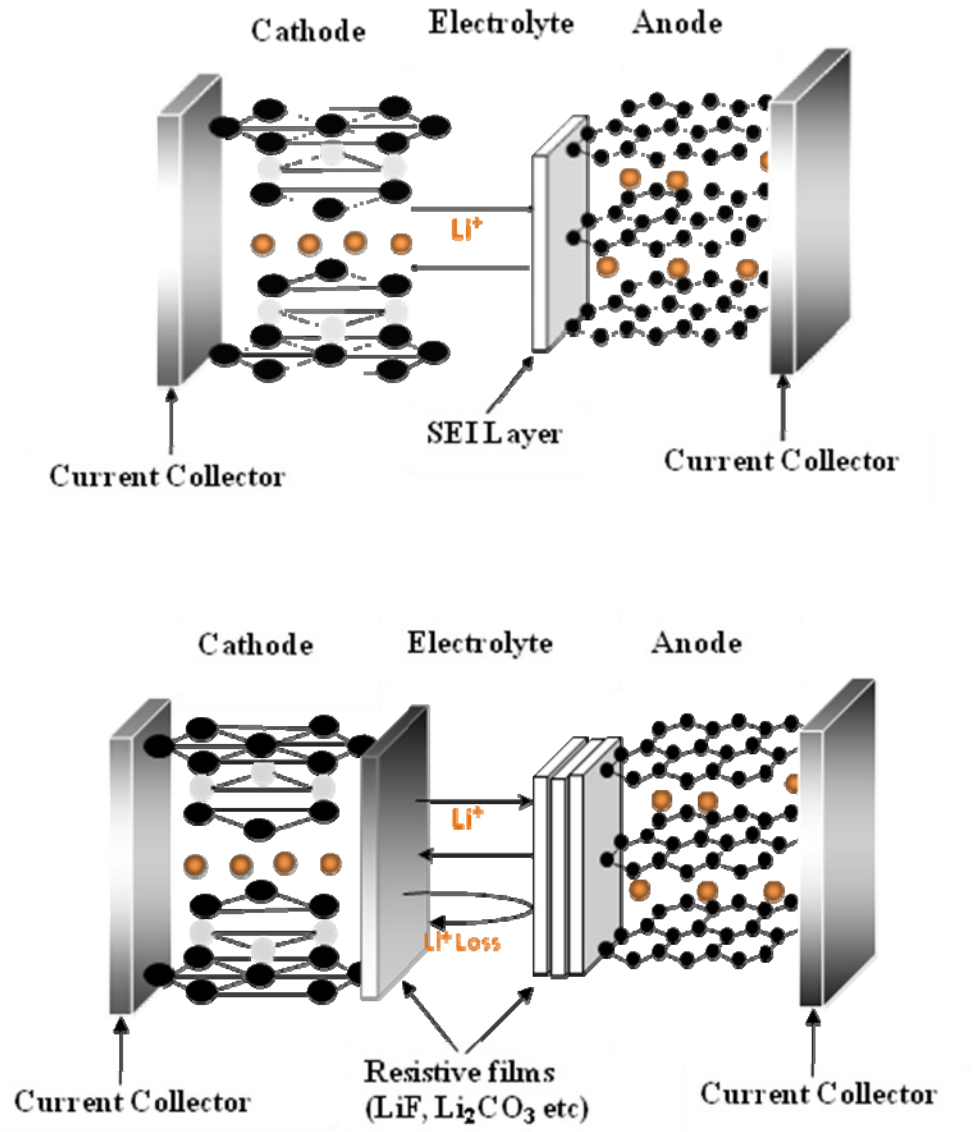

Figure 3.5: Schematic structure of lithium-ion batteries with illustration of reduce species (SEI) on the electrode surface (a) SEI formation on the anode surface on initial contact, (b) SEI growth after aging (e.g. cycling, storage, temperature).

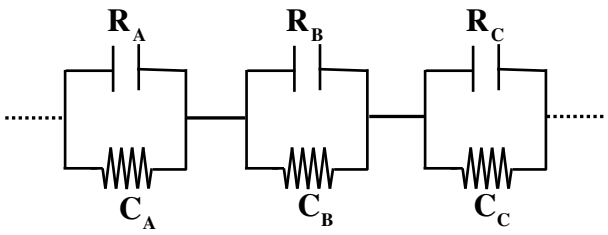

Figure 3.6: Equivalent circuit representation of multi layer SEI. R_A, R_B, R_C and C_A, C_B, C_C represents the ionic resistance and capacitance of each Sub-layer respectively.

3.1.5 The Warburg Impedance Element

Consider the transport phenomenon which represents ordinary diffusion of electro-active species in the porous electrode shown in Figure 3.2. With boundary conditions x = 0 (electrode-electrolyte interface at the pore opening) and x = ℓ (the bottom of the pore) the treatment and modeling by an equivalent electrical transmission line (infinite or finite length), i.e., assuming cylindrical pore and uniform distribution along the pore wall was completed by de Levie [1967]. Consider the circuit shown Figure 3.7, which contains the differential pore resistance r (resistance per unit length) and differential pore capacitance c (capacitance per unit length) along the length z of the pore.

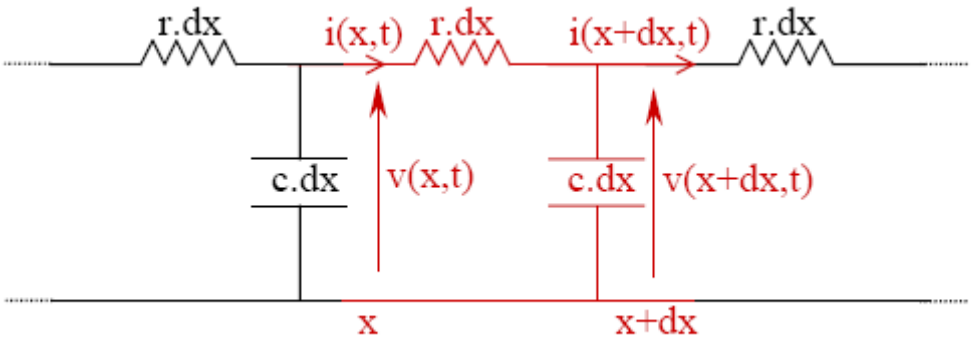

Figure 3.7: Transmission line representation of Warburg diffusion for a highly porous electrode using distributive capacitive and resistive elements.

The differential voltage and current that describes the diffusion process along the pore length is given by:

$$\frac{\partial v(t,x)}{\partial x} = -r \cdot i(t,x) \tag{3.18}$$

$$\frac{\partial i(t,x)}{\partial x} = -c \cdot \frac{\partial v(t,x)}{\partial x} \tag{3.19}$$

If sinusoidal steady state conditions are considered along with low perturbation and linear excitation then

$$v(t,x) = \mathrm{Re}\{\tilde{V}(z)e^{j\omega t}\} \tag{3.20}$$

Inserting this complex function into equations 3.16 and 3.17 then gives

$$\frac{\partial \tilde{V}(x)}{\partial x} + r \cdot \tilde{I}(x) = 0 \tag{3.21}$$

$$\frac{\partial \tilde{I}(x)}{\partial x} + j\omega c \cdot \tilde{V}(x) = 0 \tag{3.22}$$

It follows that differentiating equation (3.19) and (3.20) result in the second order differential equation that describes voltage and current along the entire pore length and is given by:

$$\frac{\partial^2 \tilde{V}(x)}{\partial x^2} - \gamma^2 \tilde{V}(x) = 0 \tag{3.23}$$

$$\frac{\partial^2 \tilde{I}(x)}{\partial x^2} - \gamma^2 \tilde{I}(x) = 0 \tag{3.24}$$

$$\gamma = \sqrt{j\omega rc} \tag{3.25}$$

The solution to these second differential equations is of the form

$$\tilde{V}(x) = V_0^{+} e^{-\gamma x} + V_0^{-} e^{+\gamma x} \tag{3.26}$$

$$\tilde{I}(x) = I_0^{+} e^{-\gamma x} + I_0^{-} e^{+\gamma x} \tag{3.27}$$

If these solution are then substituted back into equations (3.21) and (3.22)

$$\tilde{I}(x) = \frac{V_0^{+}}{Z_0} e^{-\gamma x} - \frac{V_0^{-}}{Z_0} e^{+\gamma x} \tag{3.28}$$

$$Z_0 = \sqrt{\frac{r}{j\omega c}} \tag{3.29}$$

The characteristic impedance for a finite length transmission line with open circuit terminus can then be given by:

$$Z_{oc} = Z_0 \times \left[\frac{e^{-j\gamma x} + e^{+j\gamma x}}{e^{-j\gamma x} - e^{j\gamma x}} \right] = \frac{\tau}{c} \frac{\cot(\sqrt{j\omega\tau})}{\sqrt{j\omega\tau}} \tag{3.30}$$

$$\tau = r \cdot c \tag{3.31}$$

For one dimension linear semi-infinite ionic diffusion this impedance response shown in Figure 3.8(a) is commonly observed at the high end of the frequency spectrum with 45° slope and purely capacitive behavior at low frequencies. If we however consider a transmission line with short circuit terminus the impedance response of the transmission line would then be defined by the following equation:

$$Z_{oc} = Z_{OC} = \frac{\tau}{c} \frac{\tanh(\sqrt{j\omega\tau})}{\sqrt{j\omega\tau}} \tag{3.32}$$

In the case of equation (3.30) this diffusive impedance is typical of an ideal reservoir in the electrolyte with absorption at the boundary of the electrode. The impedance plotted in the complex plane 3.8(b) show the commonly observed Warburg impedance at high frequencies, however, at low frequencies a purely resistive behavior is observed.

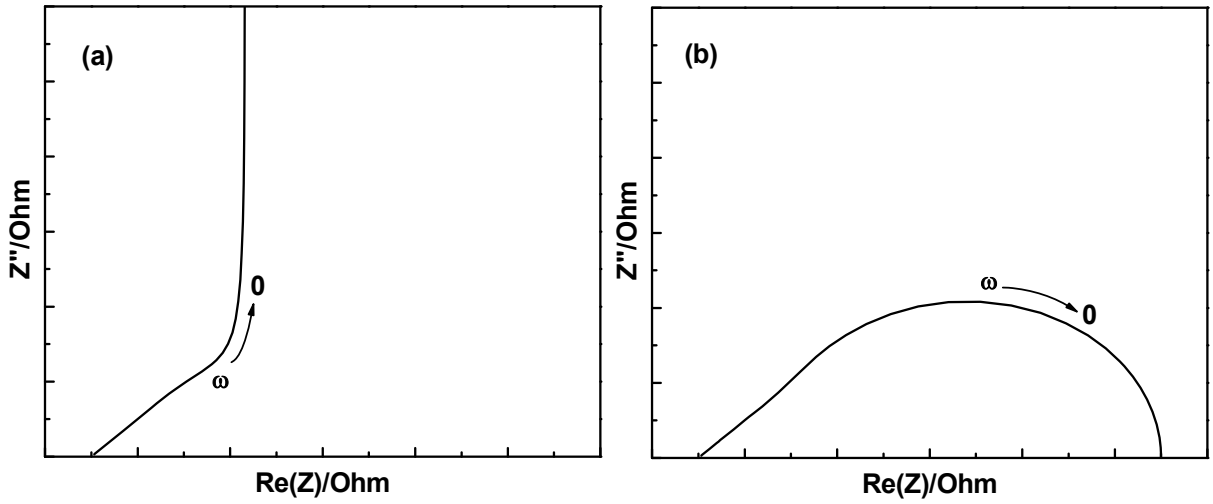

Figure 3.8: Nyquist plot describing diffusion (a) Diffusion under reflective boundary conditions (b) Diffusion under absorption boundary conditions

3.1.6 Equivalent Circuit Modeling

The interpretation of the EIS spectra for an electrochemical cell is commonly based on the Randles equivalent circuit shown in Figure 3.9(a) which includes the simple transport reaction of charge transfer reactions under diffusion control. The circuit includes solution resistance R_s, charge transfer resistance R_{ct} in series with the finite Warburg impedance Z_w and parallel double layer capacitance C_{dl}. Each circuit element is a representation of the multi-step serial or parallel electrochemical process. The result shown in Figure 3.9(b) is the impedance response of the Randles equivalent circuit and When plotted on a complex plane Z'' vs Z', a depress semi-cycle with a Warburg impedance (45° slope line) caused by mass transport process is often observed. Additional circuit elements can also be added to account for a variety of additional electrochemical processes such as the impedance and spatial capacitance associated with surfaces film which covers the electrodes surface, etc.

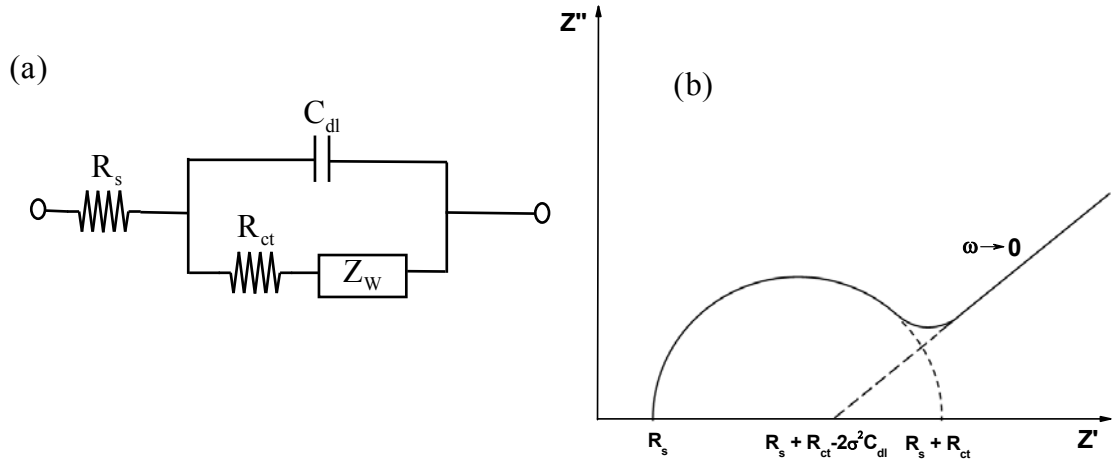

Figure 3.9: (a) Randles equivalent circuit representation of the transport process of an electrochemical cell including mass and charge transport, (b) impedance plot in the complex plane for Randles circuit.

CHAPTER 4

COMPUTER SIMULATION FOR DESCRIBING POWER PERFORMANCE OF ELECTROCHEMICAL CAPACITORS

4.1 Introduction

Improvements in the power and energy density, in addition to the cycling performances of electrochemical capacitors (EC) have increase due to the demand for their use in applications where short term power usage is required. Electrochemical capacitors are passive electrostatic energy storage device that are composed of complementary porous carbon electrodes immersed in an organic electrolyte and are capable of fast charge/discharge [80]. The patent for the first electrochemical appeared in 1957 but was not commercialized until the late 1970's by NEC and Matsushita co. The main advantages that electrochemical capacitors provides over conventional energy storage (e.g. batteries, electrostatic capacitors) systems include very high rate capability (high power density), prolong cycle life in addition to excellent cycling efficiency, a low internal resistance < 1mΩ, and wide operational temperature (-40 °C to 70 °C) [81]. These advantageous properties of the electrochemical capacitor make them suitable for use in many applications such as in hybrid-electric vehicles, military applications and telecommunications systems, etc. Currently, electrochemical capacitors have capacitance 10 to 200 time the capacitance of conventional capacitors and power density in the range ~1000-5000 W/kg and energy density in the range ~1-10 Wh/kg [82-85]. In contrast to electrochemical capacitors, lithium-ion batteries have typical energy densities in the range 50-500Wh/kg and power densities in the range 10-500 W/kg [85]. This makes electrochemical capacitors ideal for use as peak power

source in combination with standalone power sources such as batteries or fuel cells where transient power is needed to assist peak power demands, e.g., such as in vehicle acceleration/de-acceleration and high load operation [67, 81, 86, 87]. Additionally, they are well suited to supply power to the vehicle auxiliary system [82]. Electrochemical capacitors can also be used as energy reservoirs for the recovery and storage of energy during regeneration breaking. Other applications include digital communication systems where high specific power is required (e.g. short pulse duration).

Great efforts have been focused on increasing the energy density of EC capacitors including, optimization of the specific surface area and pore size of the activated carbon for increase double-layer capacitance [88-91]; the development of pseudocapacitance electrode materials for increase energy storage per unit volume [92-97]; and lately, the introduction of asymmetrical cell configuration [98-102]. The theories on energy density of EC capacitors were also developed and successfully applied to double-layer capacitors and asymmetrical cells [103-107]. The theoretical maximum energy density of EC capacitors and asymmetrical cells can be projected based on some basic parameters such as specific capacitance (or capacity) of the electrode, salt concentration in electrolyte, and operational voltage of the cell. The energy density theories can be used not only for predicting the maximum energy density of the EC capacitor but also to provide design parameters for achieving the maximum energy density. The parameters include the mass (volume) ratio between the electrode and electrolyte, porosity of the electrode for double-layer capacitance, and mass ratio between capacitive and battery electrode materials for asymmetrical cells. From the energy density theories, it was found that for most current developed systems, the theoretical energy density was mostly limited by the salt concentration in the electrolyte.

The power density of the EC capacitor is determined by the internal resistances which include the electrical and ionic resistances. The detailed resistance distributions for EC capacitors with both bipolar and spiral-wounded structures were investigated [108, 109]. The sources of electrical resistance originates from the bulk resistance of the electrode material, contact resistance between activated carbon particles, current collector, and contact resistance between the carbon electrode and current collector. The sources of the ionic resistance are separator paper and ionic resistance in the

porous electrode. The experimental results also demonstrated that the ionic resistance was a function of capacitor voltage, because the free ion concentration in the electrolyte decreased with the buildup of double-layer charges as capacitor voltage increase. However, even when the sources of internal resistance can be identified; the power density and the internal resistance of the double-layer capacitors cannot be related. The maximum peak power of the capacitor was sometime defined as the total energy divided by the internal resistance of the capacitor. It is also widely accepted that the best way to define the capacitor's performance is by using a Ragone plot [110, 111], which describes the relationship between the energy density and power density. Currently, Ragone plot can only be obtained experimentally, and no model or theory exists to predict the relation between energy and power densities based on some basic parameters which can be easily obtained experimentally.

In high current drain applications, the electrochemical capacitor will be subjected to a highly dynamic performance behavior which efficiency is of primary concern; therefore, it is important to be able to predict the dynamic behavior of the electrochemical capacitor under various environmental constraints over short periods (e.g. cold start conditions and in cranking application) so that optimum cell design can be achieved. In this paper we evaluate the performance of the electrochemical capacitor during transient and constant power discharge operation. A model implemented in Matlab/Simulink from an electrical equivalent circuit obtained from ac impedance spectroscopy is then compared to the experimental data for validation. The model consists of an ohmic resistance which represents all internal resistance within the capacitor except the ionic resistance from the porous electrode. It will be demonstrated that the total capacitance obtained from the equivalent circuit model is consistent with the capacitance values measured by dc charge-discharge method. It will also be demonstrated that the model can be use to describe the transient behavior of the capacitor, and for the first time to project the energy and power densities relationship.

4.2 Experimental

To evaluate the charge-discharge performance in addition to obtaining the dc capacitance from the slope of the discharge portion of the V-t curve for a Panasonic electrochemical capacitor (2.5V, 10F: ØD = 18mm, L= 35mm) constant current charge-discharge protocol was implemented where the capacitor was charge and discharge between 0 and 2.55V at ±20mA at ambient temperature. The potential dependent capacitance is define as the differential change in charge $\triangle Q$ divided by the differential change in potential $\triangle V$ and can be estimated according to the following formula:

$$C_F = \frac{\Delta Q}{\Delta V} = \frac{i \cdot \Delta t}{\Delta V} \tag{4.1}$$

Where, i is the instantaneous discharge current, $\triangle V$ is the potential step and Δt the differential discharge time. The internal resistance of the electrochemical capacitor which is denoted by the equivalent series resistance (ESR) is determine from the transition between charge and discharge on the V-t curve and is given by:

$$ERS = \frac{\Delta V}{\Delta I} = \frac{\Delta V}{2I} \tag{4.2}$$

Where, ΔV is the change in voltage and ΔI is the change in current. To investigate the transient load response the pulse currents of 1A (2s) and -0.5A (2s) was applied to the electrochemical capacitor respectively.

Electrochemical Impedance spectroscopy (EIS) measurements were carried out using solartron 1250B frequency response analyzer with windows PC control and data acquisition software by zplot (Snibber Associates). All spectra were collected at open circuit voltage (OCV) using 5mV sinusoidal stimulus with frequency ranging from 20 kHz - 10 mHz in potential range 0 to 2.5V with spectra collected in increments of 0.5V. The spectra are then fitted to an equivalent circuit using Zview software.

4.3 Results and Discussion

4.3.1 Galvanostatic charge/Discharge Cycling

From the result of galvanostatic cycling, Figure 4.1(a)(b), it can be seen that the V-t profile is triangular, with little variation in slope during charge-discharge; this indicates good capacitance characteristic with minimal variation in capacitance within this potential window. Based on the discharge portion of the V-t curve the capacitance was calculated using equation (4.1). The variation of capacitance with potential (Figure 4.2) show that within the potential voltage range 0-2.5V the capacitance increase from a minimum of 14.62F at 0V to a maximum of 16.64F at 2.5V. At the beginning of discharge (Figure 4.1(b)) there is a sudden transition in potential between charge-discharge. Using equation (4.2) an equivalent series resistance of 75mΩ was deduced from this transition.

Figure 4.3(a) shows the experimental terminal voltage response for the electrochemical capacitor resulting from the application of a positive (charge) and negative (discharge) pulse current shown in Figure 4.3(b).

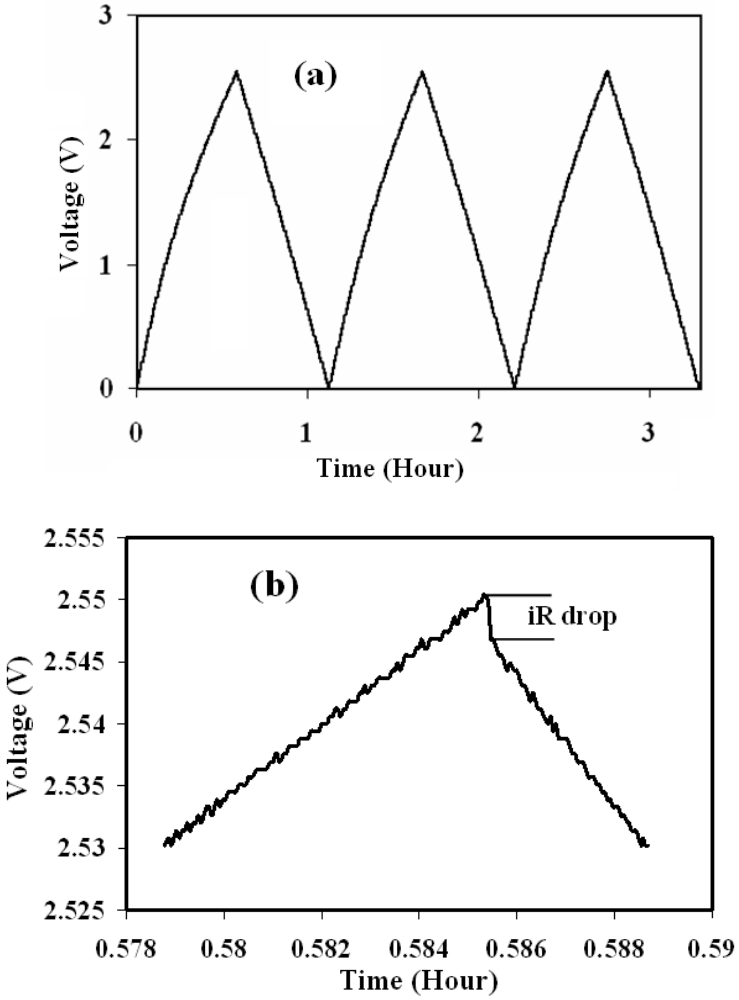

Figure 4.1: (a)(b) DC charge and discharge curves at constant current of 20mA/-20mA

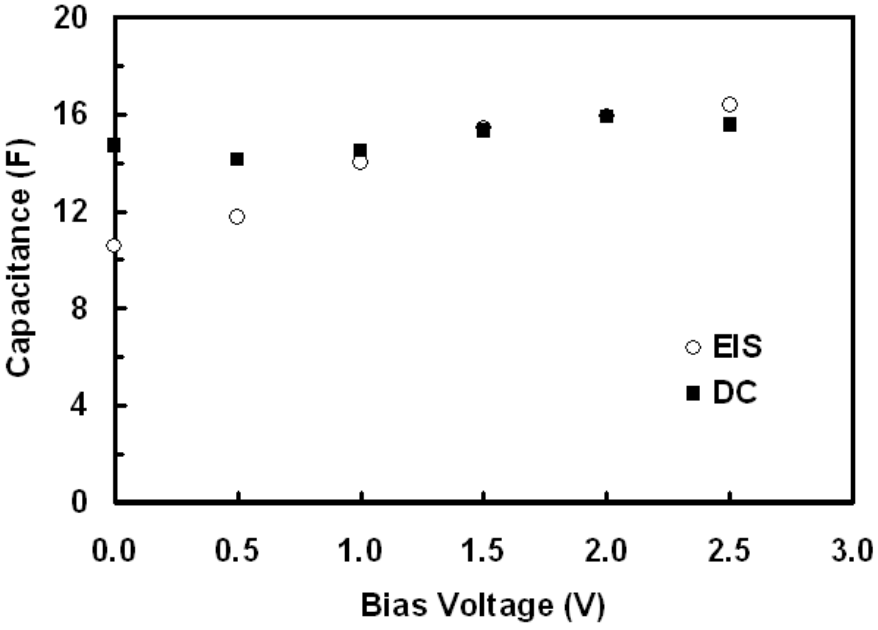

Figure 4.2: Measured dc capacitance as a function of bias voltage

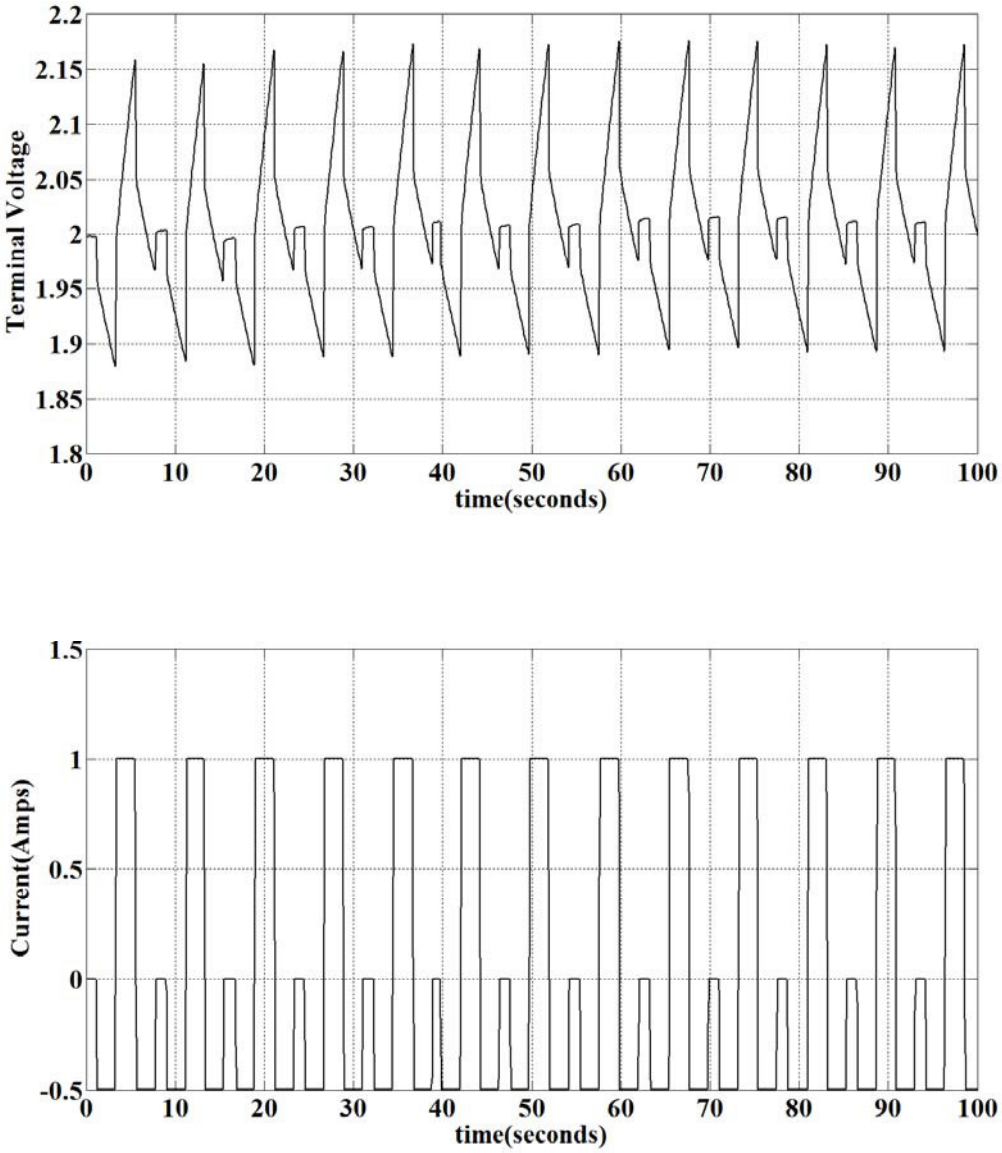

Figure 4.3: (a) Electrochemical capacitor terminal voltage, (b) Experimental pulse load current.

4.3.2 EIS Measurements

EIS spectrum analysis in Figure 4.4 shows that the frequency response of the electrochemical capacitor is similar to that of the Warburg element in series with an inductive element and a solution resistance. The inductive behavior is observed at 20 kHz – 632 Hz and can be ascribed to spiral wounding of the capacitor and leads from the frequency response analyzer, the solution resistance R_{sol} is observed at the Z' intercept of the real axis, and the Warburg element is observed at 624 Hz – 10 mHz with ~45° slop line that represent the Warburg diffusion followed by a vertical line (~90°) that represents the accumulation of charge in the electrode. The accumulated charge at low frequency represents the dc capacitance of the cell and is approximated by the following equation:

$$C_F \approx \frac{1}{\omega Z''} \tag{4.3}$$

Here ω is the frequency in rad/sec and Z'' is the imaginary component of the impedance in the complex plane. The equivalent series resistance observed was ~65.5mΩ which is a little less than what was observed using the constant-current discharge method, however this values is consistent with values obtained by others [112, 113]. Figure 4.5 shows the frequency dependent capacitance at various electrode potentials which reveal that the maximum capacitance is reached at increasing low frequencies. The dc capacitance is deduced from the low frequency region ($\omega \to 0$) of the spectra plot where it is shown that the capacitance measured by EIS is similar to the measurements obtained using galvanostatic measurement except at potentials below 1V. The dc capacitance measured by EIS varied from 10.57F at 0V to 16.37F at 2.5V. Generally, it is believed that the impedance measurements supply slightly lower capacitance value at lower potentials due to the fact that alternating current penetrates into the porous electrode with more hindrance [114].

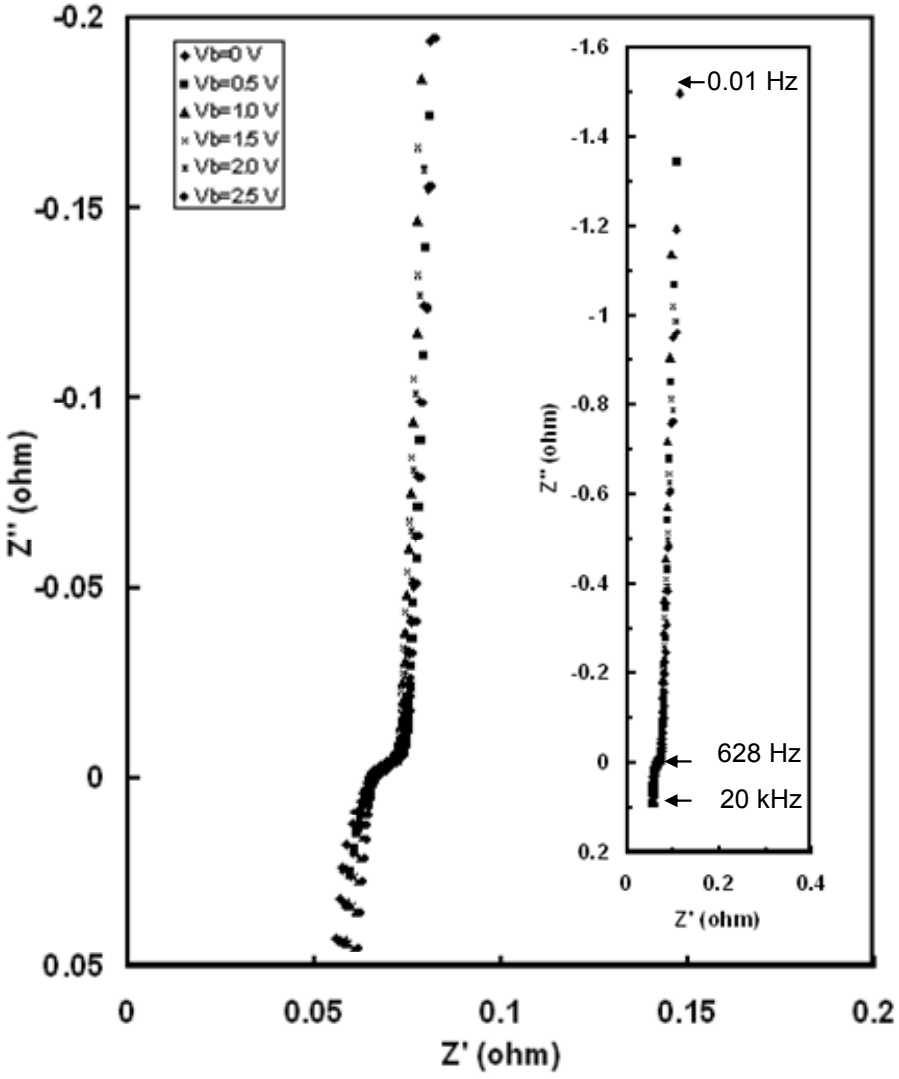

Figure 4.4: Plots of impedance at various potential voltages

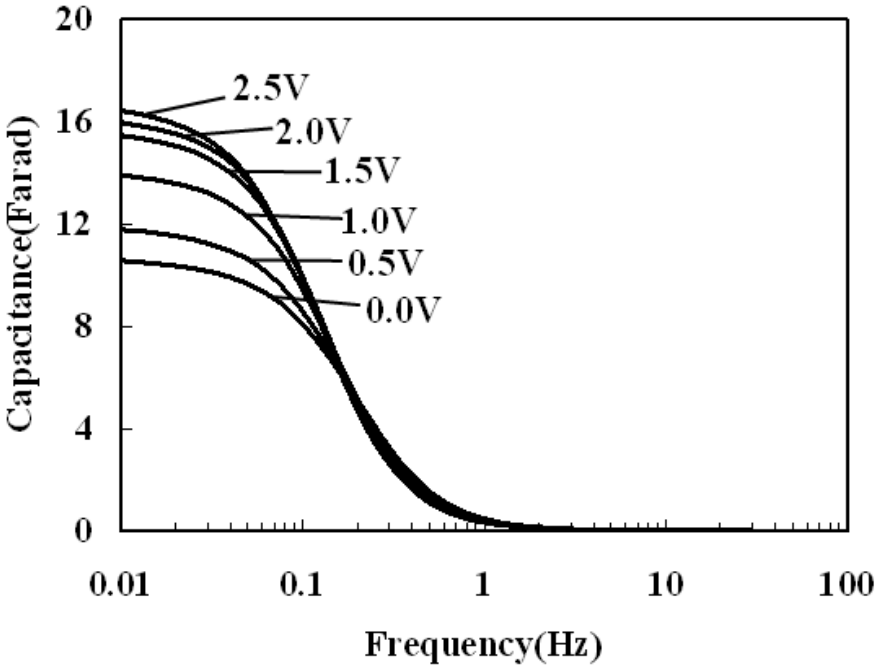

Figure 4. 5: Plot of capacitance as a function of frequency

4.3.3 EIS Measurements

The Electrochemical capacitor voltage behavior in response to a dynamic current profile is commonly modeled using the simple equivalent first order circuit shown in Figure 4.6. This circuit consist three passive circuit elements that result in a first order approximation of the dynamic response of the electrochemical capacitor. The circuit includes the double layer capacitance C_{dl}; R_P, the equivalent leakage resistance that represents the long term capability of the capacitor to maintain charge. The equivalent series resistance (ESR) that represents the energy lost due to the distributive resistance of the electrolyte, electronic contacts and the porous separator. However, advancement in technology has resulted in more complex systems as a result of integration of various energy storage systems with a major component including the electrochemical capacitor. This then, will require more accurate methods of estimating the load profile of the electrochemical capacitor under large load transients during various operating conditions.

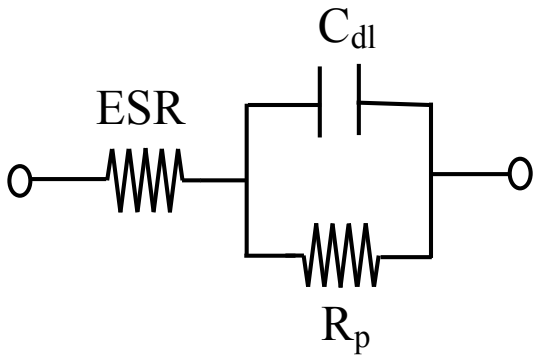

Figure 4.6: First order approximation for electrochemical capacitor equivalent circuit.

Mauracher et al. proposed that the equivalent circuit model of the electrochemical capacitor be taken directly from the ac impedance spectra, which in most cases the porous electrode can be represented in the frequency domain by the Warburg element with open circuit terminus [115]. A time domain representation of the equivalent circuit is then obtained by taking the inverse transformation of the impedance spectra in the frequency domain.

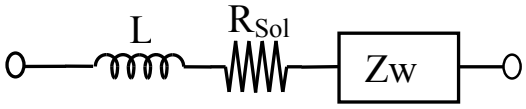

Figure 4.7: Electrochemical capacitor equivalent circuit model in the frequency domain

The impedance of the electrochemical capacitor in the frequency domain can be represented by a series combination of inductor L, ohmic resistance R_{sol}, and a Warburg impedance element Z_w shown in Figure 4.7; in this model it is assumed that the Warburg element exhibits purely capacitive behavior at low frequencies. To acquire a suitable model that represents the dynamic response of the electrochemical capacitor, it is necessary to transformer the Warburg elements in the frequency domain back into the time domain. The response of the Warburg element in the frequency domain is given by the following formula:

$$Z(j\omega) = \frac{\tau}{C_W} \frac{\coth(\sqrt{j\omega\tau})}{\sqrt{j\omega\tau}} \tag{4.4}$$

Where $\tau = R_W C_W$ and R_W and C_W are the sum of resistance and capacitance of the Warburg element shown in Fig.4.8.

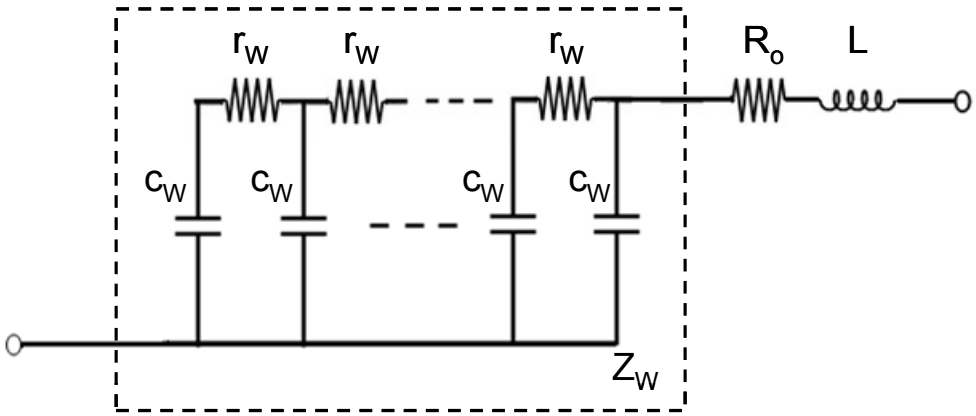

Figure 4.8: Electrochemical capacitor equivalent circuit model in the frequency domain.

The transformation or equivalent time domain representation of equation (4.4) can then be represented by:

$$\frac{k_1}{\sqrt{j\omega}} \coth\left(\frac{k_2}{k_1}\sqrt{j\omega}\right) \bullet\text{-o} \frac{k_1^2}{k_2} + \frac{2k_1^2}{k_1} \sum_{n=1}^{\infty} e^{\frac{n^2\pi^2 k_1^2}{k_2^2} t} \tag{4.5}$$

Where

$$k_1 = \frac{L}{\sqrt{D}} \quad k_2 = \frac{RTL}{cz^2F^2A_eD} \tag{4.6}$$

Comparing the parameters in (4.4) and (4.5) result in

$$k_2 = \frac{RT}{cz^2F^2A_e\sqrt{D}} = \frac{\tau}{C} \tag{4.7}$$

Then considering the impulse response for a parallel RC circuit given below by equations (4.8) and (4.5) it can be conclude that the Warburg element in the frequency domain have an equivalent time domain representation and can be express as a series combination of parallel resistive and capacitive elements.

$$\frac{1/C}{j\omega + 1/RC} \bullet\text{-o} \frac{1}{C}\exp\left(-\frac{t}{RC}\right) \tag{4.8}$$

Also form (5.5)

$$C_0 = \frac{k_2}{k_1^2} = \frac{\sqrt{D}}{I} \times \left(\frac{cz^2F^2A_eD}{RTI}\right) = C_W \tag{4.9}$$

In addition, comparing equations (4.5) and (4.8) equate to the capacitance in each parallel branch given by equation (4.10)

$$C_n = \frac{k_1}{2k_2^2} = \frac{cz^2F^2A_eL}{2RT} = \frac{C_0}{2} \tag{4.10}$$

It can also be deduced from equations (4.5), (4.8) and equation (4.10) that

$$R_n = \frac{2\tau}{n^2\pi^2C_0} \tag{4.11}$$

Finally, Figure 4.9 show the equivalent Warburg element representation of solid state diffusion into the porous electrode material using a series/parallel RC network.

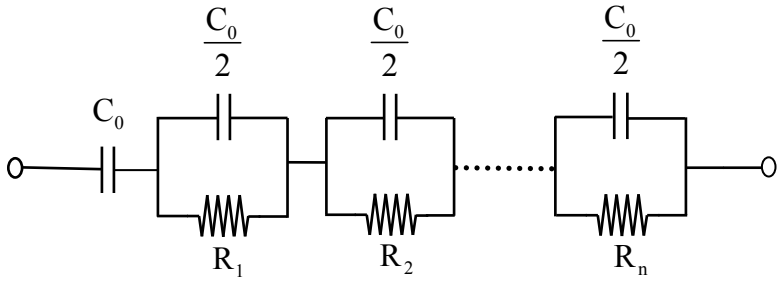

Figure 4.9: Equivalent Warburg element Z_w, represented by series/parallel R-C Network.

4.3.4 Transient Response

The electrochemical capacitor can be represented by the equivalent circuit shown in Figure 4.10. The circuit includes a Warburg equivalent network, an equivalent series resistance R_s and an inductive contribution, L. Note that the leakage resistance is ignored in this model. Consider the condition when the electrochemical capacitor is under constant-current load discharge, then summing the voltage around the loop result in a terminal load voltage given by:

$$v_L(t) = V_w - i_s R_s + L\frac{di_s}{dt} \tag{4.12}$$

Where, V_w is the voltage across the Warburg equivalent network and is given by

$$V_w = \sum^{n} V_n \tag{4.13}$$

The voltage on the capacitor C_0 is the given by:

$$V_0 = V_i - \frac{1}{C_0}\int_0^t i(t)dt \tag{4.14}$$

Where, V_i is the initial voltage on the double-layer capacitor, C_0. The current in each parallel RC network is the given by:

$$i_c = i_s + i_p \tag{4.15}$$

And

$$i_p = \frac{V_n}{R_n} \tag{4.16}$$

Where i_c and i_p are the currents in the parallel RC network respectively. The voltage on each parallel capacitor is then given by:

$$C_n = -\frac{2}{C_0}\int_0^t i_c(t)dt \tag{4.17}$$

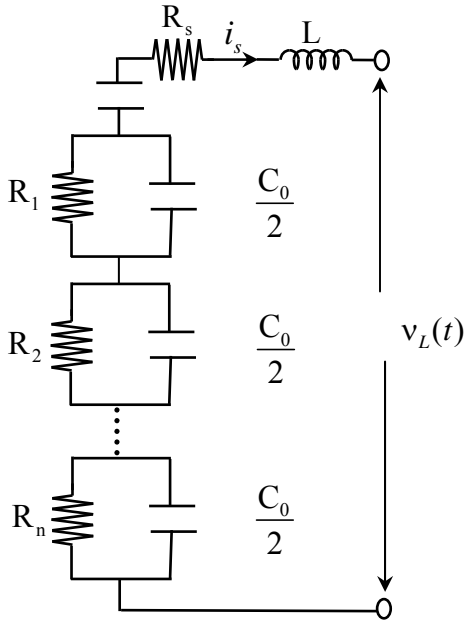

Figure 4.10: Electrochemical capacitor equivalent circuit model

4.3.5 System Model Simulation Matlab/Simulink

In order to validate the behavioral model for the electrochemical capacitor, implementation and simulating of the operational characteristics including the terminal voltage, output power, and energy delivered under various load conditions, equations (4.12)-(4.20) which describes the various characteristics of the electrochemical capacitor were entered into Matlab/Simulink software and compared to the experimental result. The I-t load profile that was used in the actual experiment was saved into a matlab file and used as input to the electrochemical capacitor model in Matlab/Simulink. Figure. 4.11 shows the result of the simulated and the experiment analysis. It is clearly

seen the simulated terminal voltage under pulse current load show good agreement with the terminal voltage from the experiment.

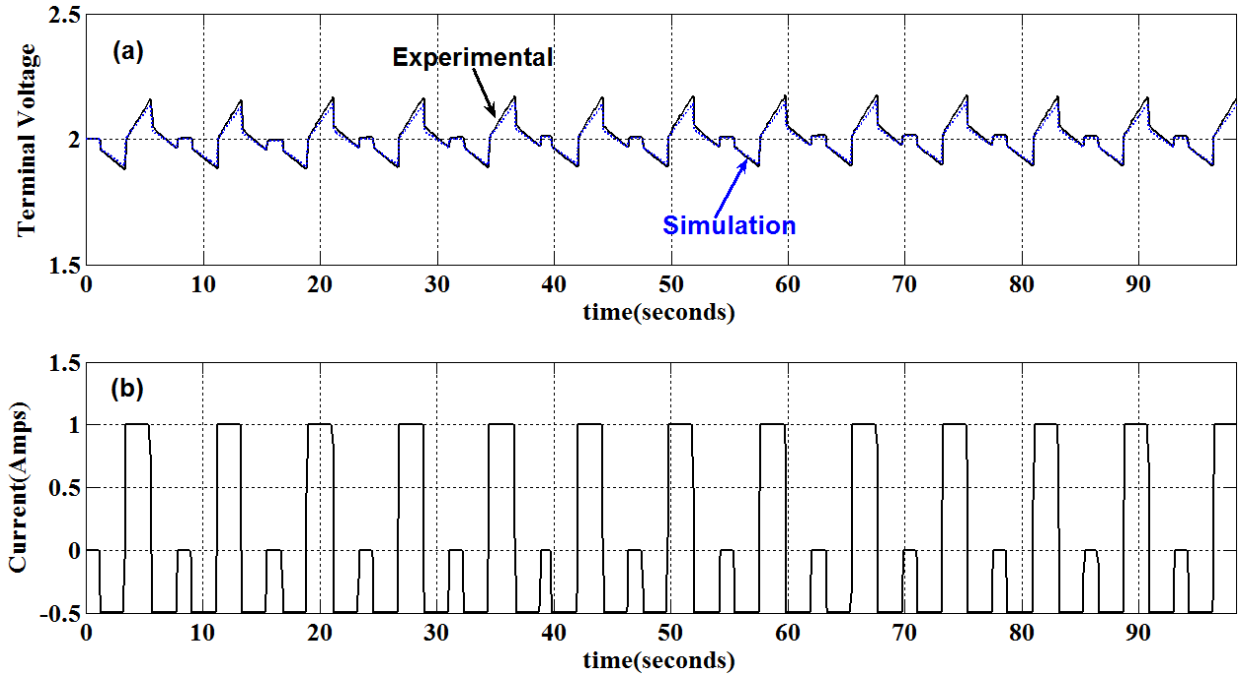

Figure 4.11: Comparison (a) Simulation capacitor and experimental terminal voltage in response to pulse current, (b) The input current profile.

4.3.6 Power Performance

Figure 4.12 show the V-t profile of an EC capacitor discharged at constant power mode. Due to the maximum current limitation of the test system, the discharge process was stopped before the capacitor reached the voltage of zero. The total time for discharge was obtained based on the fitting curve using a polynomial as shown in Figure 4.12. The energy density as a function of power density (Ragone plot) can be obtained and is plotted in Figure 4.13. Experimentally, at low power densities such as <W/L, the deliverable energy density drops rapidly.

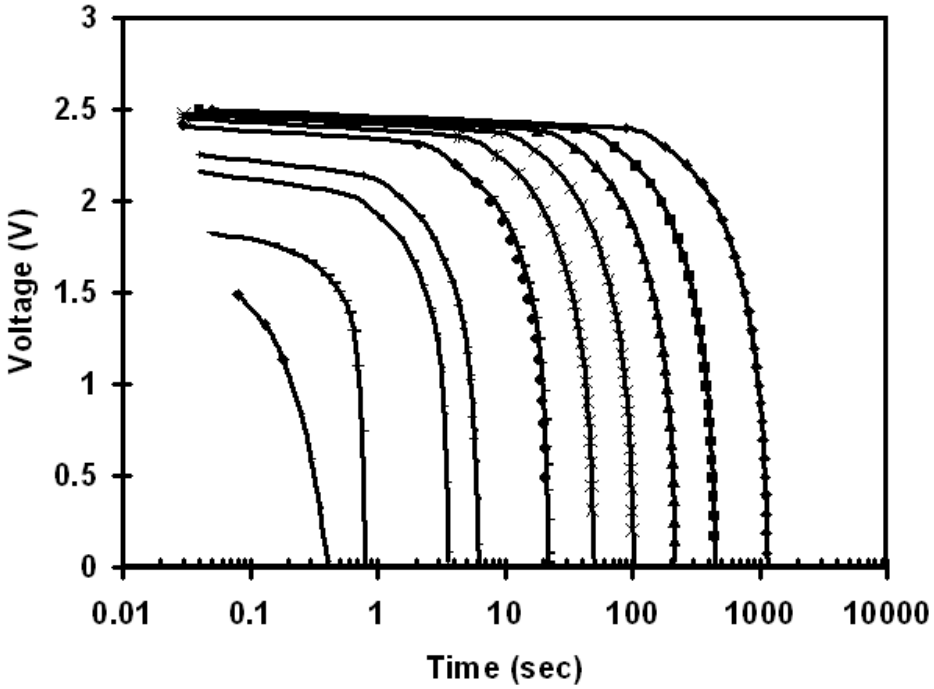

Figure 4.12: The voltage profile for EC capacitor discharged at different power levels. The line is a theoretical fitting using polynomial curves.

To simulate the Ragone plot for a constant power load connect to the EC capacitor, the active power drawn result in a terminal voltage given by:

$$v_L(t) = \frac{P}{i_s(t)} \tag{4.18}$$

It is also determined that the maximum power that can be delivered to the load by the electrochemical capacitor is given by:

$$P_{max} = \frac{V_0^2}{4R} \tag{4.19}$$

and the total energy dissipated is given by:

$$E_c = Pt_\infty \tag{4.20}$$

The same set of equations (4.12)-(4.17) was used during the simulation, but the current i_s was not a constant value and was determined by equation (4.18). The stimulated

Ragone plot was also plotted in Figure 4.13 in order to compare with the experimental results. During the stimulation, a constant value of $R_o = 0.0665\Omega$ and $R_W = 0.033\Omega$ were used; however, a voltage dependent capacitance C_W was used. The capacitance values were determined by EIS measurement and linear fitting within two data points as shown in Table 1. It can be seen that at low power density, simulated result agreed with experimental result well; however, at high power density, > W/L, the deliverable energy density was lower than the projected values by equivalent circuit model. It is believed that the lower value obtained from the experimental power density is due ionic depletion in porous electrode. The total weight of electrolyte in EC capacitor was measured and is about 3.84 g. It is assumed that the salt concentration of electrolyte is 0.75 M/L. The total available charge from the electrolyte is about 234 C if it assumes 100% salvation. When the EC capacitor was fully charged to 2.5 V, the number of cations and anions, which are equivalent to charged of 40 C would be accumulated at the double layer of the negative and positive electrodes, respectively. The charge of such small number of ions should not affect the ionic resistance of the capacitor. It was also proven from the resistance measurements at different bias voltages. Both ohmic and ionic resistances in the electrode are almost constant in the voltage range of 0 to 2.5 V. However it must be pointed out when the capacitor was charged or discharged rapidly, the ion concentration and ionic resistance in EC capacitor were not uniformly distributed, particularly in electrode, which is dependent on the thickness of the electrode and pore size of activated carbon. Therefore, it is believed that at high power discharge and charge condition, for these carbon surfaces with small pore size, the ion diffusion process was too slow that ion was either over saturated or depleted.

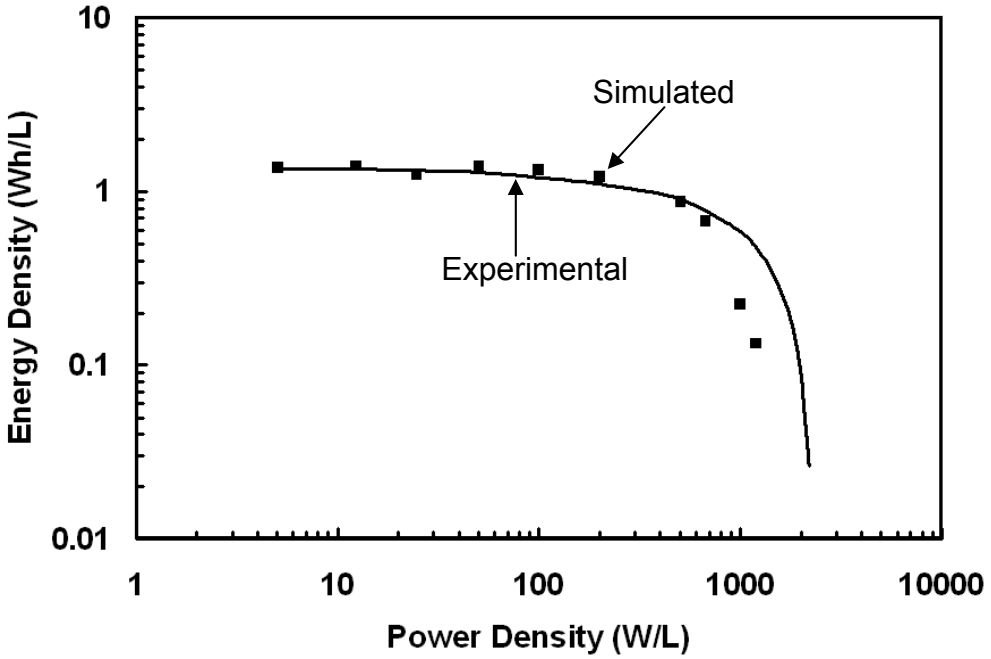

Figure 4.13: Ragone plot of EC capacitor. The data points and the time obtained from experiment and simulation using equivalent circuit model, respectively

4.3.7 Effect of Ionic Resistance on Power Performance

The EC capacitor voltage behavior in response to a dynamic current profile is commonly modeled using the simple equivalent first order circuit shown in Figure 4.6. This circuit consist three passive circuit elements that result in a first order approximation of the dynamic response of the energy lost due to the distributive resistance of the electrolyte, electronic contacts and the porous separator; a double layer capacitance C_{dl}; and an equivalent leakage resistance, R_P, that represents the long term capability of the capacitor to maintain charge. Figure 4.14 shows the Ragone plots stimulated by the simple RC circuit model (R_P was ignored) and transmission line circuit model as shown in Figure 4.15. For simplicity, a constant value of C_W was used. To compare Ragone plots obtained by two different models, it can be seen that when $R_o >> R_W$, the simple RC circuit model will be good enough to describe the energy and

power relationship of EC capacitor; however, when $R_o < R_W$, the RC circuit model cannot accurately project the maximum power density of EC capacitors, which is limited by ionic resistance of R_o. From Figure 4.14, it can also be seen that when R_o reduced, the point of energy density, which starts to decline, increased, and also the ultimate power density increased.

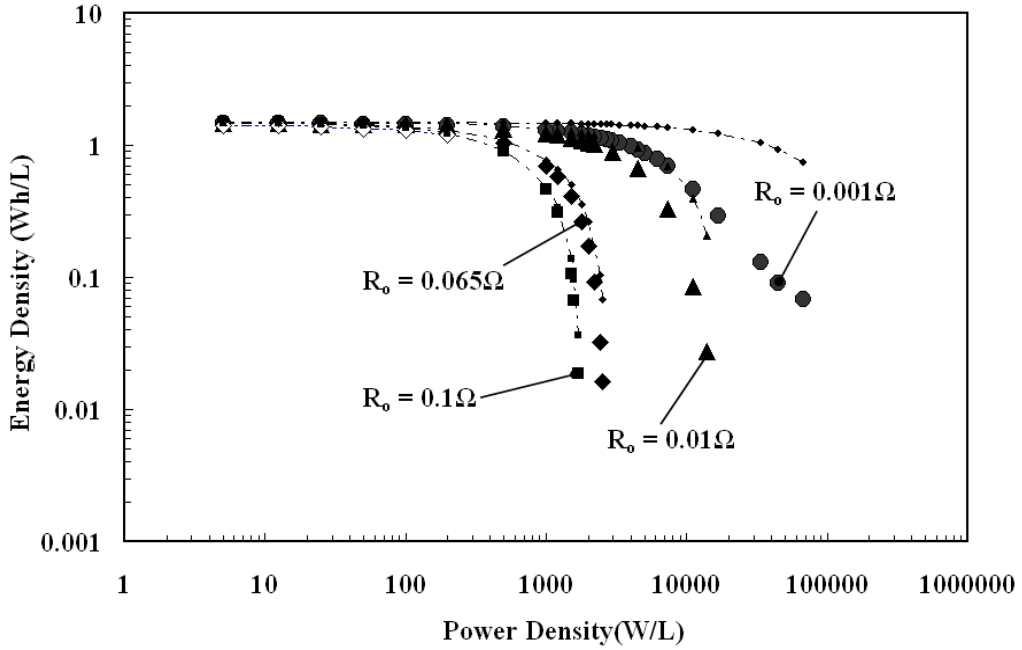

Figure 4.14: Simulated Ragone plots using simple RC circuits (with small symbol) and transmission line circuit (with large symbol) model. For both models, the capacitance of 14F was used and ohmic resistances were varied as indicated. The R_W for the transmission line model is 0.033Ω.

Figure 4.15 shows that stimulated ragone plots for the fixed R_o but variable R_W. It can be seen that when R_W increased, the energy density decreased; however, the ultimate power density was determined by the ohmic resistance only. The relationship between the Ragone plots shown in Figure 4.14 and Figure 4.15 can be understood by the equivalent circuit shown in Figure 4.8. The charges are stored in capacitors which formed the transmission line network. When charges is stored or released from the capacitors, they all must pass through the ohmic resistor R_o; therefore, the value for R_o would determined the ultimate power density of EC capacitors. Charges stored or released from different capacitors in the transmission line network pass through different number of resistor in series as shown in Figure 4.8. For the capacitor c_W which

is closed to R_o less resistance is available to block charge storage or release than those capacitors some distanced from R_o. The greater values of r_W mean that the current decays faster along the capacitor distribution in the transmission line. Therefore, the ionic resistance influences the energy density for the EC capacitor.

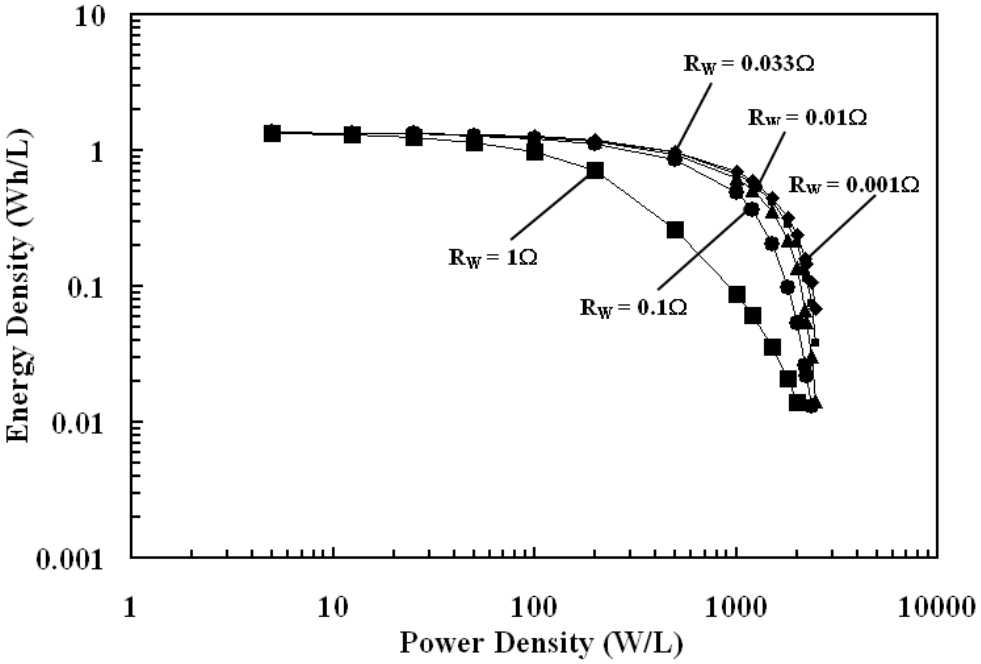

Figure 4.15: Simulated Ragone plots for various Warburg resistances, R_W. The capacitance and ohmic resistance are 10F and 0.066 Ω respectively.

4.4 Conclusion

Because of the large improvement in power performance of EDLCs the emergence for new and diverse applications has improved significantly. The optimum energy-power performance for EDLC can be efficiently determined using computer simulation. An equivalent circuit model for EC capacitors was obtained from the impedance spectra and simulated in Matlab/Simulink. The result shows that accurate simulation of the terminal voltage under dynamic load current and constant power load can be achieve. We have shown that the optimum operating conditions between specific power and specific energy can be determined from simulating of ragone plots. The result also verifies that effectiveness of using CAD based tools in obtaining good

estimates of the performance of EC capacitors under various load conditions. The advantages are cost, time and optimization of cell design.

CHAPTER 5

STUDY DEGRADATION MECHANISM IN Li-POLYMER BATTERIES

5.1 Introduction

Lithium-ion polymer batteries have widely been used in small portable devices such as mobiles phones, notebook computers and PDA's, however, due to their relatively high energy densities it has been proposed for use in high energy density application such as in the aerospace industry, and in hybrid electric vehicles (HEV) [3, 116-119]. Extensive studies have shown that solvent decomposition, exfoliation of the graphite electrode material, and co-intercalation phenomena plays a major role in the irreversible capacity loss with continuous intercalation/de-intercalation of lithium-ions [120-122]. Additionally, passivation of the negative electrode during initial cycling is critical and results in the thermodynamic stabilization of the anode by preventing further reaction with the solvent and salt species. SEI also plays a critical role in blocking the passage of electrons and preventing the co-intercalation of organic species from the electrolyte while allowing the conduction of Lithium-ion.

The SEI film formation and influence on cell performance have been extensively studied. Many techniques including, e.g. Fourier transform infrared spectroscopy (FTIR), X-ray photoelectron spectroscopy (XPS), in situ Atomic force microscopy (AFM) and Scanning electron microscopy (SEM) have been employed to characterize and provide valuable information about the nature of SEI on the electrode surfaces. The properties and chemical makeup of SEI has been the focus of intense scientific investigations with analysis [47, 123] showing that the major constituents of these complex surface films in alkyl carbonate solution are $ROCO_2Li$, ROLi, RCOOLi, LiCl,

LiF, and Li_2CO_3, etc, R represents metal ions; the continuous precipitation of the solution species on the electrode surface are also one on the main reasons for irreversible capacity loss for lithium-ion batteries. Reports have shown that the formation of SEI film on the graphite electrode is strongly dependent on the composition of the electrolyte and on the graphite structure which consequently plays a critical role in the electrochemical performance [11].

G.B Appetecchi et al [124] have studied the interfacial behavior of $Li_{1-x}C_6$ electrode and $LiClO_4$-EC-DMC-Pan polymer electrolyte with lithium as reference electrode. Electrochemical impedance spectroscopy shows two separate semi-circles in the high to medium frequency range and a Warburg behavior in the low frequency range. The bulk resistance of the electrolyte was ascribed to the left intersect of the two semi-circles and the medium-low frequency semicircle was ascribed to passivation of the electrode by reaction between the LiC_6 electrode and the polymer electrolyte. Cycling study was also carried out on the positive electrode for which the initial capacity was not retained with cycling. It was concluded that this lost in capacity in the positive electrode was due to lost in structural integrity or reductive phenomena at the interface. Kim et al [16] concluded a similar study for which they investigated the electrochemical performance of lithium polymer battery consisting $LiCoO_2$ as cathode, mesocarbon microbead as anode and P(VdF-co-HFP) based gel polymer electrolyte. They showed a reduction in coulombic efficiency from 99% to 98.5% in the 1^{st} and 20^{th} cycle respectively. They also ascribed the decrease in capacity and increase in internal impedance to the physical changes at the electrode/electrolyte interface as a result of electrolyte decomposition or change in the electrode structure.

The present study investigates the cycling characteristics and performance of lithium-ion polymer cell using electrochemical impedance spectroscopy (EIS), x-ray diffraction analysis and scanning electron microscopy. Mechanisms for capacity degradation and reduce cell performance of commercial lithium-ion polymer cell are suggested. In addition, Morphological analysis will be use along with EIS to understand the formation of surface film with continuous charge discharge cycling.

5.2 Experimental

The Lithium-polymer batteries used in this experiment is a commercial cell with a nominal discharge capacity of 840 mAh as specified by the manufacture (Sony co.). The cell had an aluminum plastic laminated exterior film with dimensions 38×35×62 mm. The cell structure consist, Cu foil|graphite negative electrode|porous polyethylene separator, gel solution of ethylene carbonate (EC)/propylene carbonate (PC), $LiPF_6$|$LiCoO_2$ positive electrode|Al foil [125]. Table 6.1 lists the physical properties of the cell as specified by the manufacture. The cell was galvanostatically/potentiostatically cycled in a two electrode configuration where Charge/discharge cycling in constant current (CC) and Constant voltage (CV) mode was performed at room temperature using an Arbin multichannel battery tester. For continuous cycling the cell was charged using a CC protocol to an upper potential of 4.2V then potentiostatically polarized until the current dropped to less than 10mA; the cell was then discharged to a lower cutoff potential of 3.0V using CC protocol.

Electrochemical Impedance spectroscopy (EIS) measurements were carried out using solartron 1280B frequency response analyzer with windows PC control and data acquisition software by zplot (Snibber Associates). EIS evaluation was performed at various levels of Lithium-ion intercalation as well as for cells in the continuous cycled state. The corresponding EIS results are then evaluated by fitting the battery response to an equivalent circuit using Zview (Scribner Associates). All EIS spectra were collected using a 5mv sinusoidal stimulus with frequency ranging from 20 kHz-10 mHz. In addition, the spectra was collected under open circuit voltage (OCV) conditions where CC-CV protocol was applied; in this mode the cell was charged using a constant current to the desired OCV then a constant voltage applied and held at equilibrium until the current decayed to less than 10mA.

Table 5.1: Design characteristic for Sony lithium-ion polymer battery, UP383562A. [126]

Size (D × W × H)	3.85 × 35 × 62 mm
Weight	15g
Nominal capacity	760 mAh
Nominal voltage	3.7V
Charge voltage	4.2V
Charge time	90 mins
Energy density (volume)	375 Wh/L
Energy density (weight)	190 Wh/kg
Cycling performance	80% @500 cycles
Temperature range	-20° - 60° C
Cathode	$LiCoO_2$
Anode	Graphite

5.3 Results and Discussion

5.3.1 Charge/Discharge Characterization

Figure 5.1 (a) shows the typical potential discharge curves for various discharge currents. The voltage plateau at high rate discharge is a function of cell over-potential. It can be seen that the discharge voltage has a very smooth profile between 4.0V-3.6V. The discharge capacity was studied using various discharge rates with a maximum discharge rate of C/8 results in a maximum discharge capacity of ~741mAh; this is in good agreement with the nominal capacity provided by the manufactures, 840mAh. Higher c-rate performances are shown in Figure. 5.2, where this cell is shown to have a capacity retention of (615 mAh) 83% at 2C discharge rate. Figure 5.3 show the plot of the discharge capacity as a function of cycle number which shows the gradual decrease in capacity from 771 mAh to 200 mAh after 1600 charge-discharge cycles at 1 C-rate discharge. The cell was then cycled at lower C-rates until the discharge capacity has dropped to less than 100 mAh at a discharge rate of C/8.

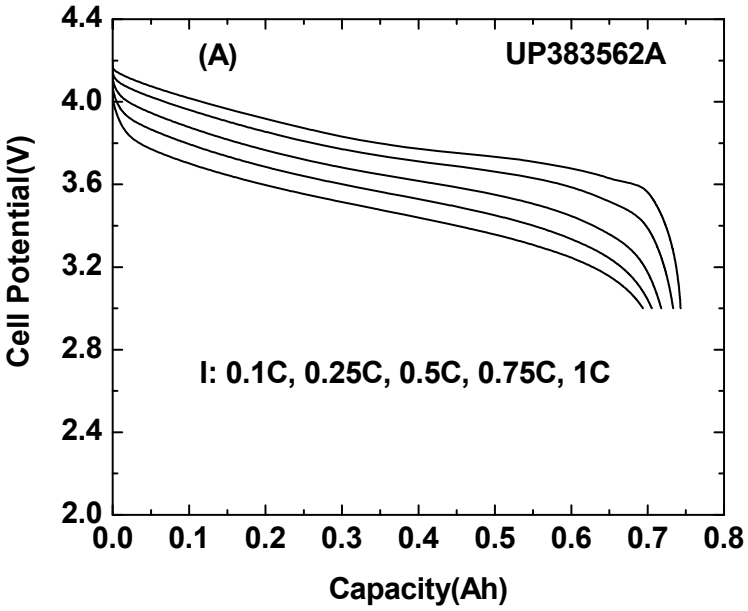

Figure 5.1: Galvanostatic discharge profile for Li_XC_6|Solvent-$LiPF_6$|$Li_{1-X}CoO_2$ at various discharge currents for fresh cell

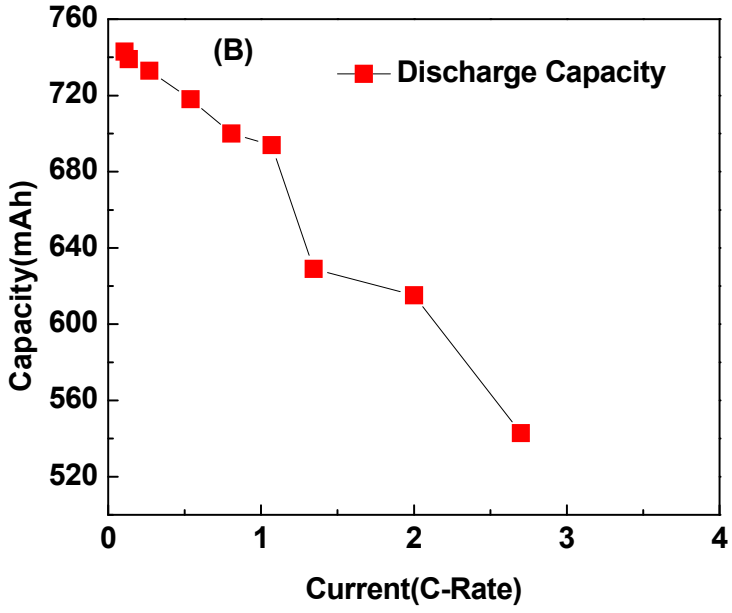

Figure 5.2: Discharge capacity at various C-Rate

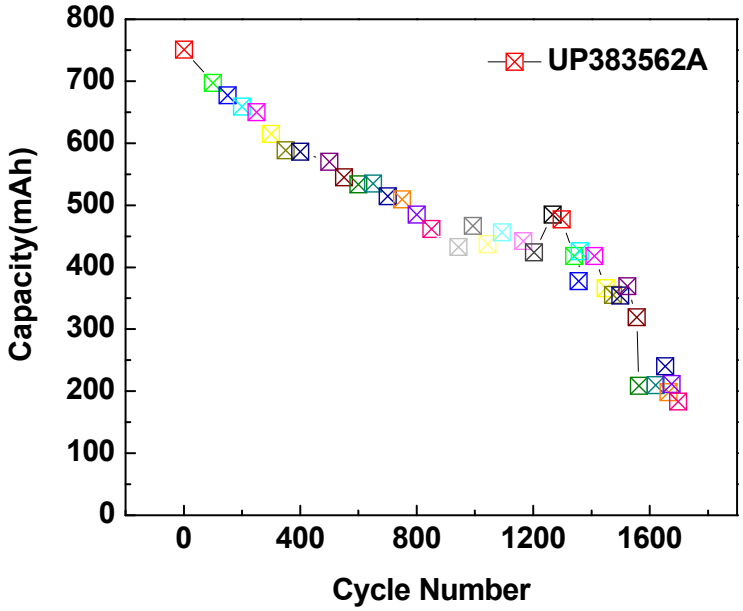

Figure 5.3: Discharge capacity as a function of cycle number, 1C-discharge

5.3.2 EIS Measurements

Figure 5.4 shows the typical Nyquist plot for a fresh electrochemical cell measured at an open circuit potential of 4.0V. The impedance in the complex plane represents the combined impedance contribution from both anode and cathode, therefore all parameters related to mass and charge transport reflects the superposition of both electrodes. The spectra contain a resistance R_s at the interception of the real axis which can be ascribed to the electrolyte, electronic contacts and the separator and correlates with the ohmic polarization of the cell. The spectra indicates an inductive arc at high frequencies (20kHz-15.85kHz) for which previous reports [127, 128] have attributed to the porosity of the electrodes and the mechanical winding of the cell, however some inductive behavior have been observed when conducting EIS on the leads connected to the frequency response analyzer, suggesting that the leads which are attach to the frequency analyzer may contribute to some of the inductive behavior. In this case the inductive behavior will not play a significant role in cell performance. At least three overlapping depressed semi-cycles is observed at high to medium frequencies (15.85 kHz-15.85 Hz). These semi-cycles are associated with the slow migration of Lithium-ion through different SEI layers that covers the active mass and have equivalent surface film resistance (R_f) and corresponding film capacitance (C_f).

The semi-circle at mid-frequency (15.85 Hz-0.05 Hz) is associated with intercalation type reactions and is characterized by charge transfer resistance (R_{ct}) and the associated double-layer capacitance (C_{dl}) at the electrode|electrolyte interface followed by a low frequency (0.05 Hz-0.01 Hz) Warburg slope line that represent the solid state diffusion of Lithium-ion into the porous electrodes. Generally diffusion is much faster in the electrolyte than the bulk electrode therefore this process will be ascribe to the bulk electrode process[129]; this process is usually observed as a 45˚ incline in the complex plane (Z" vs Z').

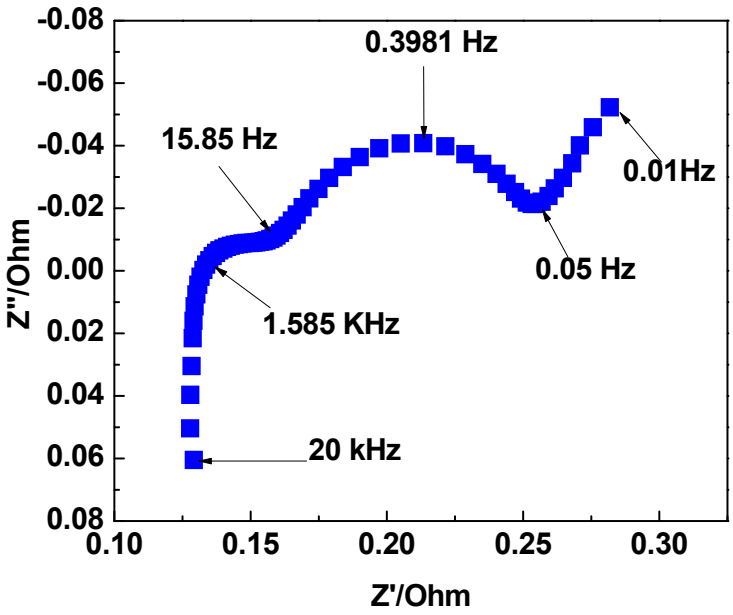

Figure 5.4: Typical impedance spectra for fresh cell performed at OCV 4.0V

The Nyquist plots collected in the potential range 4.2V to 3.0V, Figure 5.5, show that the diameters of the semi-cycles are all potentially dependent. It was observed however that the solution resistance R_s, remained relatively constant at various levels of lithium-ion intercalation. The semi-cycle associated with the charge transfer kinetics showed a largest increase with decreasing polarization potential. This may be attributed to the availability of effective reactive sited for Li-ion during intercalation/de-intercalation [130, 131]. The depress high frequency semi-cycle (1.585 kHz -15.85 Hz) show some moderate dependency on potential voltage. Increase or decrease in high frequency semi-cycle may result from volume changes [132, 133] during de-

intercalation/intercalation resulting in the expansion-contraction in the cross-sectional area of SEI. The overall increase in impedances at low potential also indicated some level of difficulty in the electrochemical kinetics.

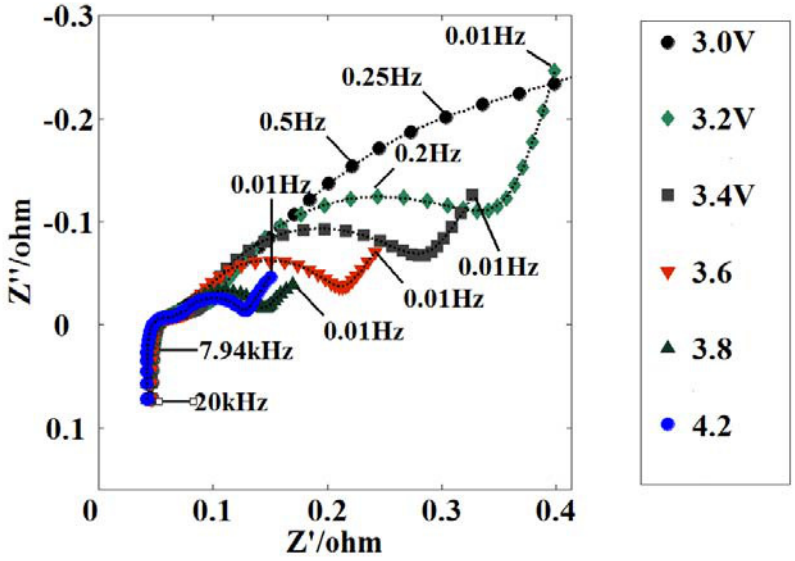

Figure 5.5: Comparison of the experimental and fitted spectra for Lithium-ion polymer cell at various potentials. Frequency range 20 khz to 0.01hz.

In order to elucidate the decrease in cell performance with continuous cycling, postmortem analysis was performance using electrochemical impedance spectroscopy. Figure 5.6 (a) and (b) show the impedance spectra of a fresh and cycled (i.e. 3000 cycles) cell respectively. The spectra were all obtained at OCV (4.0V). It is observed that the diameter of the high frequency semi-cycles which corresponds to the spatial film capacitance and lithium migration through SEI increase with cycling which indicates an increase in film thickness on the electrode surfaces. In addition, an increase in the size of the mid-frequency semicircle is observed indicating a slowing down of electrochemical reactions at the electrode-electrolyte interface which result in an increase in charge transfer resistance. The low frequency Warburg slope that appeared during initial cycling had shifted to much lower frequencies after a few hundred charge-discharge cycles. This suggests an increase in rate limiting time constant associated with other processes (i.e. charge transfer between the electrode and the electrolyte) involved in the cell reaction.

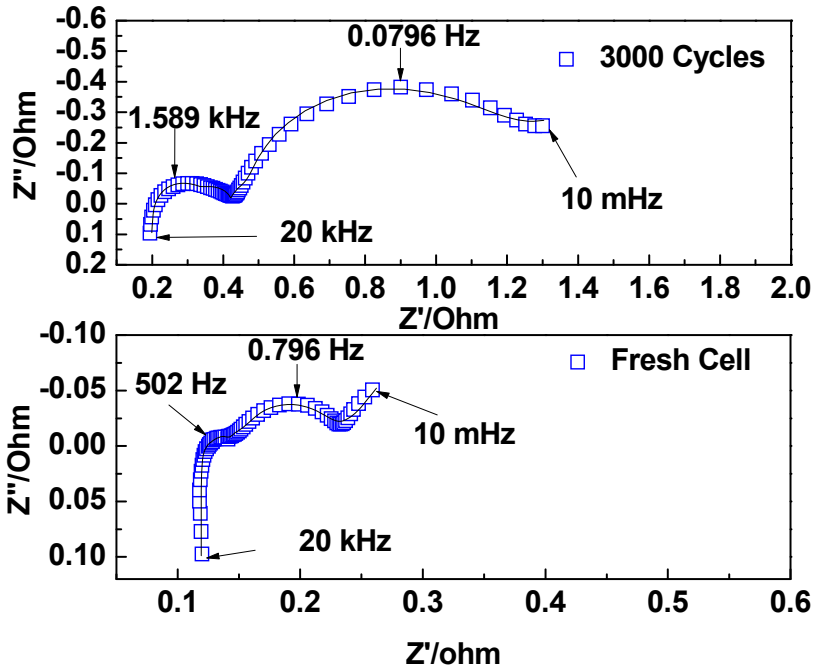

Figure 5.6: (a),(b) Comparison of the experimental spectra for Li-ion polymer cell for fresh and continuous cycled cell. Frequency range from 20 khz to 10 mhz.

5.3.3 Equivalent Circuit Model

Figure 5.7 depicts the modified Randles equivalent circuit used to fit the impedance data and investigate the cell performance by characterization of mass and charge transport processes using discrete electrical equivalent circuit elements. The ohmic impedance of the cell is represented by series resistor R_s. The resistive and capacitive behavior of the passive surface film R_{fn} and C_{fn} is represented by 'voigt type' analog containing 3 parallel RC elements. The charge-transfer kinetics at the electrode-electrolyte interface is represented by a parallel resistor R_{ct} (charge-transfer resistance) and capacitor C_{dl} (Double-layer capacitance). The classical approach to modeling the diffusion process include the use of the finite space Warburg element (FSW) given by equation (1); from this circuit good accuracy can be achieved. The fittings are shown by the solid lines in the Nyquist plot, Figure 5.5 and Figure 5.6. The resistance R_s is observed at the interception of the real axis at the high frequency end of the Nyquist plot and has value 0.125Ω. The charge transfer resistance R_{CT} increase linearly with

potential from 0.0737Ω at 4.15V to 0.2545Ω at 3.15V.The relative time constants attributed to the multi-layer surface films are observed at the mid to high frequency end of the spectra. The solid state diffusion of lithium-ion into the bulk electrode with reflective boundary can be represented by the finite space Warburg element Z_w. This element is given by the following equation [132]:

$$Z_w = \frac{\tau_d}{C_W} \frac{\mathrm{Coth}(j\omega\tau_d)^{1/2}}{(j\omega\tau_d)^{1/2}} \tag{5.1}$$

Where ω is related to the angular frequency of the applied ac stimulus signal, τ_d is associated with the characteristic diffusion time constant, C_W the differential capacitance associated with the intercalation process at low frequencies and p denotes the finite space behavior or porosity of the electrode [133, 134]. In addition, the ionic equivalent resistance can be expressed in the following form:

$$R_W = \frac{\tau_d}{C_W} \tag{5.2}$$

The equivalent circuit use equation. (5.1) to represent the ionic diffusion phenomena at the low end of the frequency spectrum using Zview (Scribner Associates) with non-linear least square (NLLS) fitting procedure.

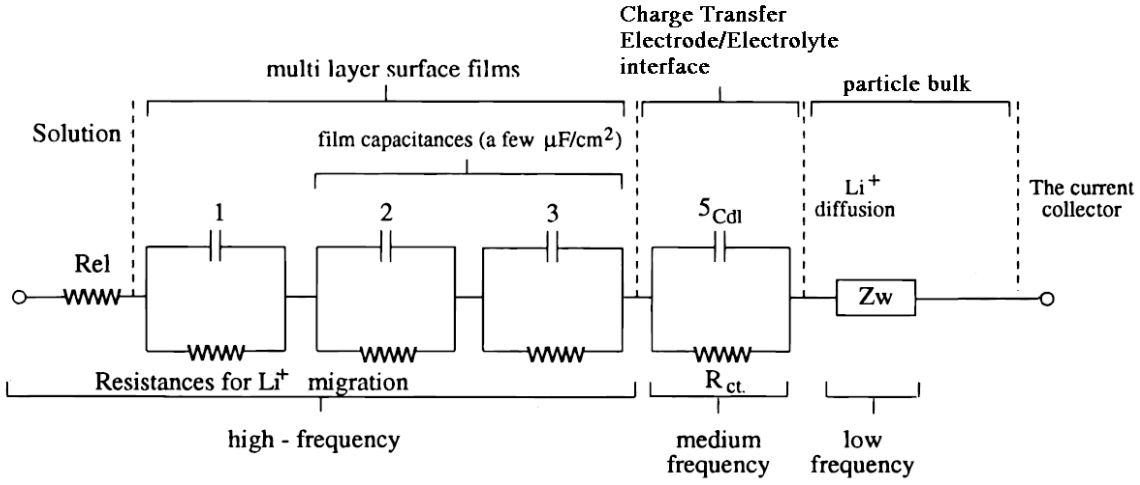

Figure 5.7: Electrical equivalent circuit used for interpretation of the impedance spectra in Fig 5.2.

Figure 5.8 through Figure 5.11 shows the variation of parameters with OCV for the fresh and continuous cycled cell. Figure 5.8 shows that for the fresh cell R_{CT} varied from 0.0737 Ω to 0.2545 Ω in the potential range 4.2 to 3.0 V respectively. However, after 3000 charge discharge cycles R_{CT} had an increase from 0.695 Ω to 1.75 Ω in the same potential range. This indicates a significant decrease in the kinetic rates with continuous cycling. One of the main reasons for increase in charge transfer resistance includes the precipitation of highly resistive surface films on the surface of both anode and cathode electrodes. Figure 5.9 show that the mass transport resistance R_W also increased significantly from 0.1635 Ω to 0.42651 Ω in the range 4.2 to 3.0 V to 2.553 Ω to 11.17 Ω in the same potential voltage range respectively. In addition, Figure 5.10 show that the double layer capacitance C_{dl}, in the nominal operating potential range also decreased slightly with cycling. Since the double layer capacitance is a function of electrode geometry this may indicate that parts of the electrode may have become isolated due to various compounds, e.g., LiF, and Li_2CO_3 etc [44, 54]. In Figure 5.11 the overall surface film impedance also increase which can result from the increase thickness of surface film on the electrode surface.

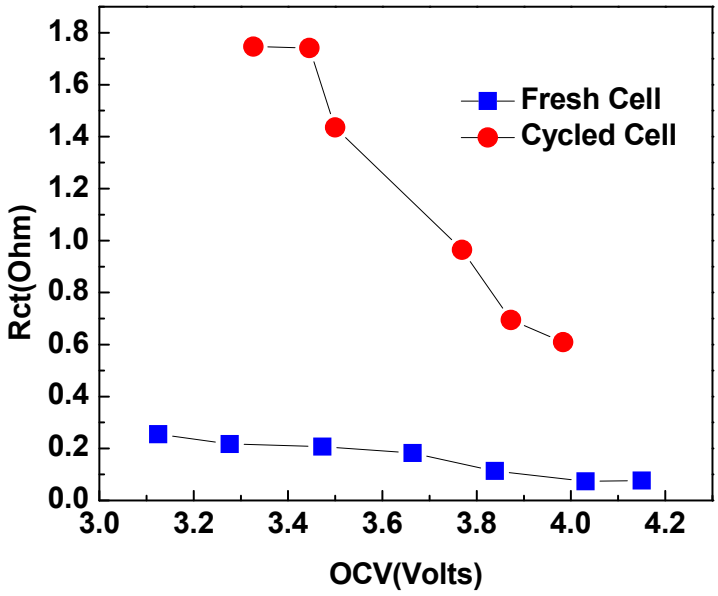

Figure 5.8: Comparison of Charge transfer resistance of fresh and continuous cycled (3000 charge-discharge cycles) cell at various potentials.

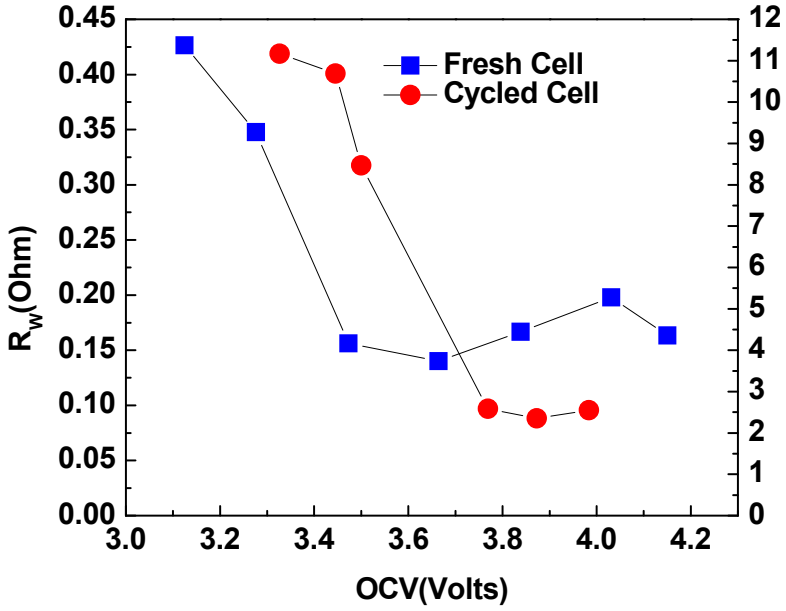

Figure 5.9: Diffusion impedance of fresh and continuous cycled (3000 charge-discharge cycles) cell at various potentials.

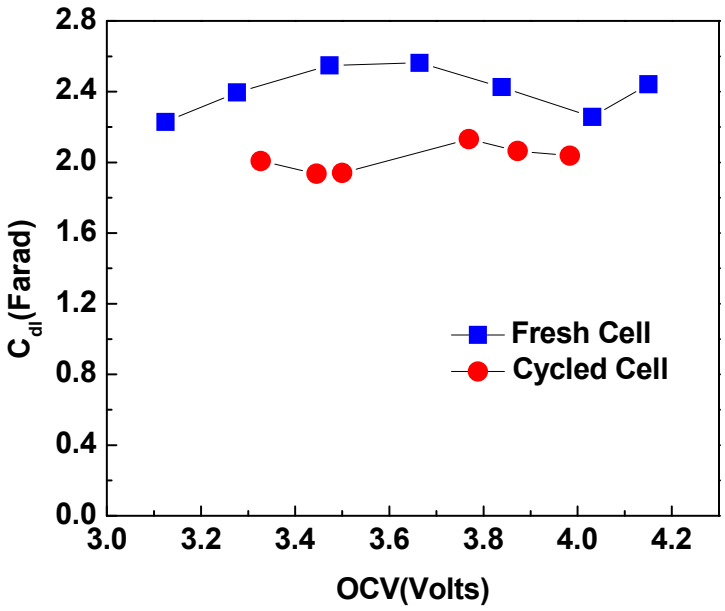

Figure 5.10: Comparison of the double layer capacitance for fresh and continuous cycled (3000 charge-discharge cycled) cell at various potentials.

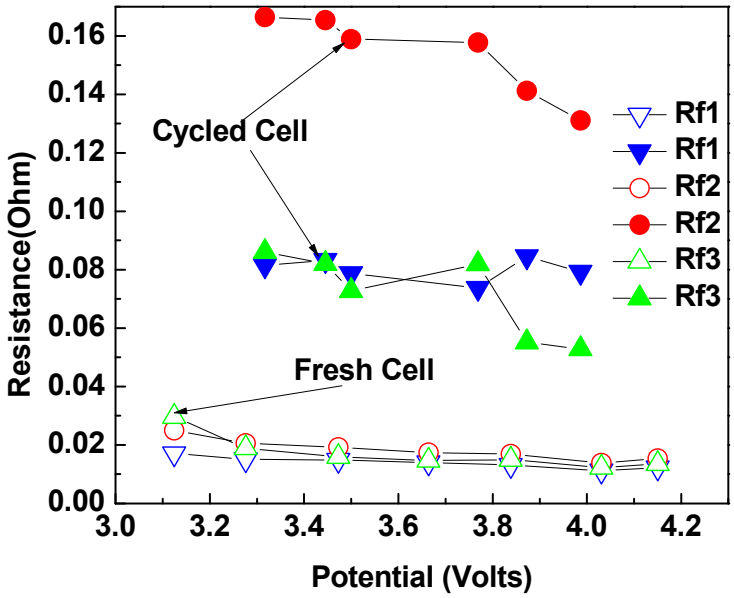

Figure 5.11: Surface film impedance for fresh and continuous cycled (3000 charge-discharge cycles) cell at various potentials.

The increase in total cell impedance can be caused by three facts, (1) the coverage of the electrode surface by highly resistive surface films with continuous cycling; (2) the ionic resistance increased because the lithium-ion concentration in the electrolyte decrease with continuous cycling, and lithium-ions are consumed and deposited on the electrode surface [135-138]; (3) Structural modification of the positive electrode. These facts correlated directly with the increased diameter of the high to mid frequency semi-circles and increase ionic impedance observed in the impedance spectra of the continuous cycled cell. Furthermore, the increase in mass transport impedance R_W is related to modification in the bulk structure which can result in decrease availability of active diffusion path length for lithium-ion intercalation/de-intercalation; pore blockage by reduce products with reduce ionic permittivity can be a major contributor. In general, it is observed that the overall impedance of the cell increases with increasing cycling number as a result of the decrease ionic conductivity of surface films on the electrodes. The reduction in transport properties contributes to increase over-potential resulting in reduce rate capability of the electrochemical cell and contributes greatly to reduce cell performance.

5.3.4 SEM Analysis

SEM analysis was conducted on samples taken from the positive ($Li_{x-1}CoO_2$) and negative electrode (Li_xC_6) to observe morphological changes on the surface of the electrodes after prolong cycling. The electrode samples were collected in the discharge stated in an ultra pure argon filled glove-box which include samples from an un-cycled cell and one that the cycles over 3000 charge-discharge cycles i.e., cell discharge capacity was 100mAh at ~ C/10 discharge. SEM was performed using Joel JSM 5900 electron microscope operated at 20 keV; note, the samples were briefly exposed to air during the SEM insertion process. Figure 5.12 (a)-(d) shows the SEM analysis for the fresh and continuous-cycled cells. The analysis of the fresh cell show that the graphite electrode structure is composed single particle of meso-carbon micro-beads (MCMB). Morphological differences between the graphite electrodes before and after cycling show distinct changes. After 3000 charge-discharge cycles, it can clearly be seen from Figure 5.12 (b), that the surface morphology of the negative electrode had change significantly. This observation is consistent with the conclusion from the ac impedance analysis which shows the hindrance of lithium-ion transport through SEI due to the buildup of surface film on electrodes that act to block the transport of lithium-ion through the porous electrode. Analysis on the positive electrode ($Li_{x-1}CoO_2$) before and after cycling, Figure 5.12 (c),(d) shows large irregular shaped particles of varying sizes. The micrographs reveal no observable change in surface morphology between the un-cycled and continuous cycled cell.

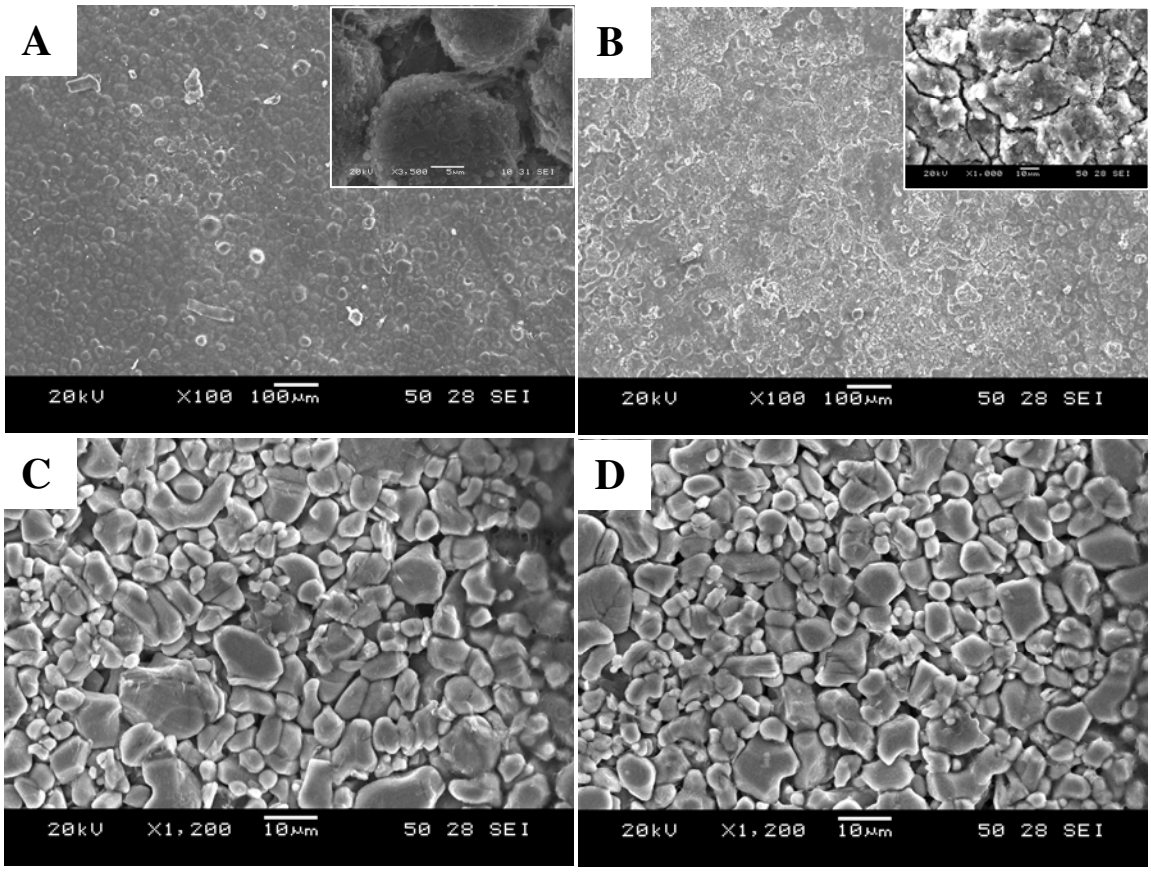

Figure 5.12: SEM micrograph (a) un-cyled Li_xC_6 anode (b) Li_xC_6 anode after 3000 charge discharge cycles (c) un-cycled $Li_{x-1}CoO_2$ cathode (d) un-cycled $Li_{x-1}CoO_2$ after 3000 charge- discharge cycles.

5.3.5 XRD Analysis

X-ray diffraction was employed to evaluate the crystal structure of the anode and cathode of the fresh and continuous cycled cell. Samples were removed from the cells and x-ray diffraction (CuK_α radiation at 45 kV and 30 mA) analysis performed using Siemens D500 diffractometer at ambient temperature. Data were collected in the 2θ range from 10˚ to 90˚ at a scan rate of 0.20˚/min.

The x-ray diffraction patterns for the fresh and continuous cycled cell are presented in Figure 5.13 and Figure 5.14. The sharp peaks indicate that the sample has a high degree of crystallinity. The main peaks positions for the fresh cell conforms to the reference patterns of $LiCoO_2$ having rock salt type structure (space group R3m) with sublattice a = 2.816 Å and c =14.051 Å [139]. The hexagonal structure of Li_xCoO_2 consist a close pack arrangement of oxygen atoms with Li^+ and Co^{3+} ions occupying

alternating (111) plane of octahedral sites that can reversibly intercalated/de-intercalate Li^+ from the structure with corresponding change in cobalt oxidation [139, 140]. The (003) reflection peak position at 2θ = 18.86˚ is more pronounce compare to the other peak positions (i.e. (101), (006), (104), etc), which indicates a preferential orientations of the c-axis (003) lattice planes that is parallel to the substrate (current collector). Figure 5.13 (a), (b) shows that after continuous cycling, the characteristic peaks position remain relatively unchanged, however some relative shift in peak positions (006), and (018) were observed. The relative intensity of the peaks are related to the preferential orientation of the crystallites or structural defects [141]. If the relative increase in peak intensity of the (003) plane is related to the orientation of the crystallites then there should be a corresponding relative change in peak intensities in all (00*l*) planes. However this is not observed when comparing the XRD patterns of the fresh and continuous cycled cell. It is also apparent that the ratio (I_{003}/I_{104}) of peak intensity of the (003) diffraction peak to the (104) diffraction peak increase with increasing cycling which is relates to defect in the rock salt crystal structure, i.e. Co^{3+} ions are substituted by Li^+ ions [141].

Table 5.2: Comparison of peak intensity for pristine and cycled sample of Li_xCoO_2

	Peak Intensity (003)	**Peak Intensity (104)**	**I_{003}/I_{104}**
Pristine Cathode	3734	427	8.74
Cycle Cathode	6912	421	16.41

Similarly, the XRD pattern for the graphite anode of the fresh cell is shown in Figure 5.14 (a) with dominant peaks at (002) and (004). Comparing the XRD patterns of the continuous cycled anode in Figure 5.14 (b) to the XRD pattern of the fresh cell in Figure 5.14 (a) show no change in peak position. From this result we can conclude that no distinct change in structure of the anode occurs during continuous cycling.

Therefore it is reasonable to conclude that the bulk structural characteristics of the anode and cathode are maintained during continuous charge-discharge cycling. However XRD analysis of the lithium cobalt oxide cathode ($Li_{x-1}CoO_2$) indicates some structural disorder in the bulk electrode during continuous cycling.

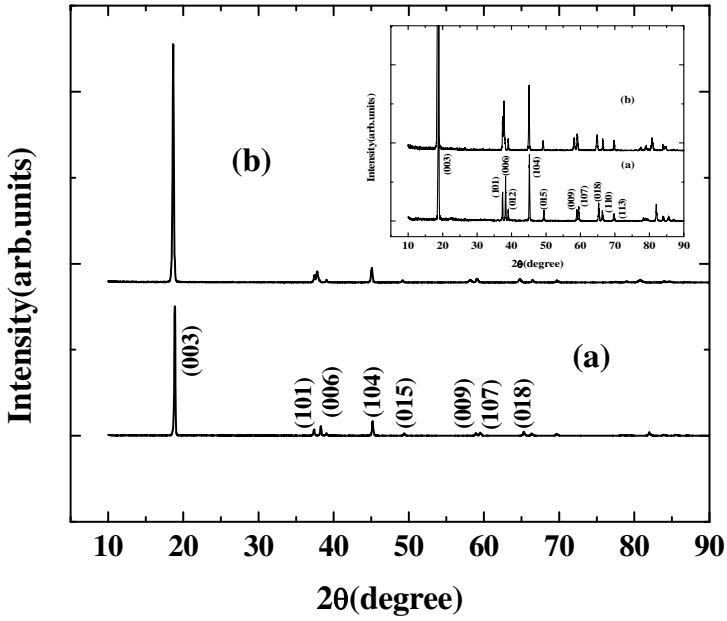

Figure 5.13: X-ray diffraction pattern for $Li_{x-1}CoO_2$ (a) fresh cell (b) continuous cycled cell

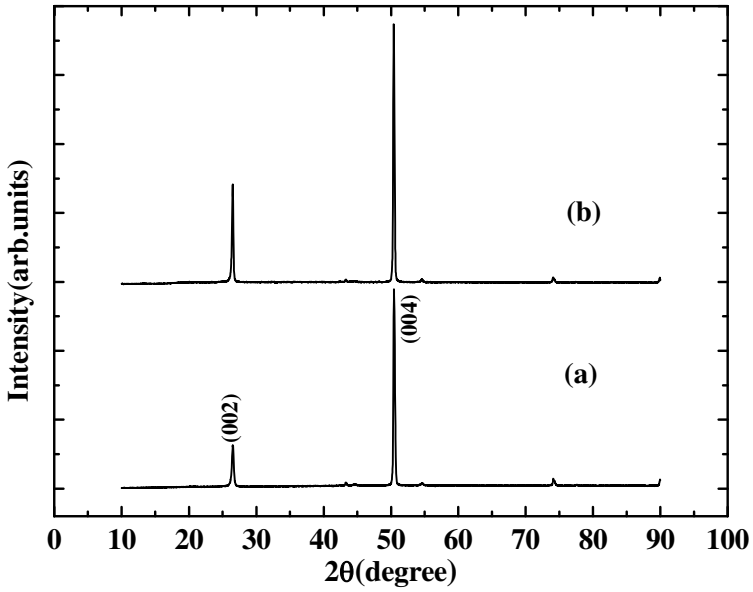

Figure 5.14: X-ray diffraction pattern for Li_xC_6 (a) fresh cell (b) continuous cycled cell

5.3.6 Half Cell Analysis

To understand which electrode contributes more to capacity fade half cell analysis were conducted using disc shaped (diameter =1.27 cm) samples that were punched from the bulk electrodes of a pristine and cycled cell. The puncture anode and cathode were 0.027g and 0.044g respectively. Composite cells were assembled as shown in Figure 5.15 (a) - (d) and include components of both pristine and continuous cycled cell. The cells were assembled in an argon filled gloved box using a Swagelok-typed half cell setup. They were then taken out for charge-discharge experiments. The composite cells were charge to 4.0V using a constant current of +100 μA then discharged to 3.0V using a constant current of -100 μA.

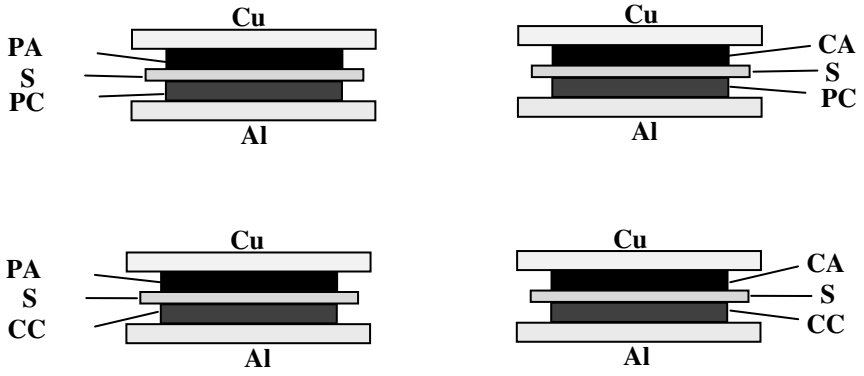

Figure 5.15: For composite cell configuration PA, PC, CA, CC and S stands for Pristine Anode (PA), Pristine Cathode (PC), Cycled Anode (CA), Cycled Cathode (CC), respectively. Cu and Al are the copper and Aluminum current collector.

Figure 5.16 shows the discharge profile for the various half cell configurations. For a pristine cell i.e. pristine anode and pristine cathode material, the discharge capacity was about 1.2 mAh. For the composite cell cycled anode + pristine cathode the discharge capacity was ~ 0.5 mAh. For the cell configuration, cycled anode (CA) + Pristine cathode (PC) the discharge capacity was ~0.700 mAh which show a reduction in discharge capacity compared to the pristine cell. The composite cell comprising cycled anode (CA) + cycled cathode (CC) had a discharge capacity of 0.25 mAh. These

results reveal that both electrodes show reduction in capacity with cycling. Reduction in anode capacity is supported by SEM analysis which shows that one of the main reasons for capacity fade is the reduction of highly resistive films on the anode surface. It can also be observed from Figure 5.16(c), (i.e., cycled cathode) that greater over potential voltage was observed on discharge. It is also noted that the increase in over potential voltage of the cycled cathode is similar to the over potential on the cycled composite cell.

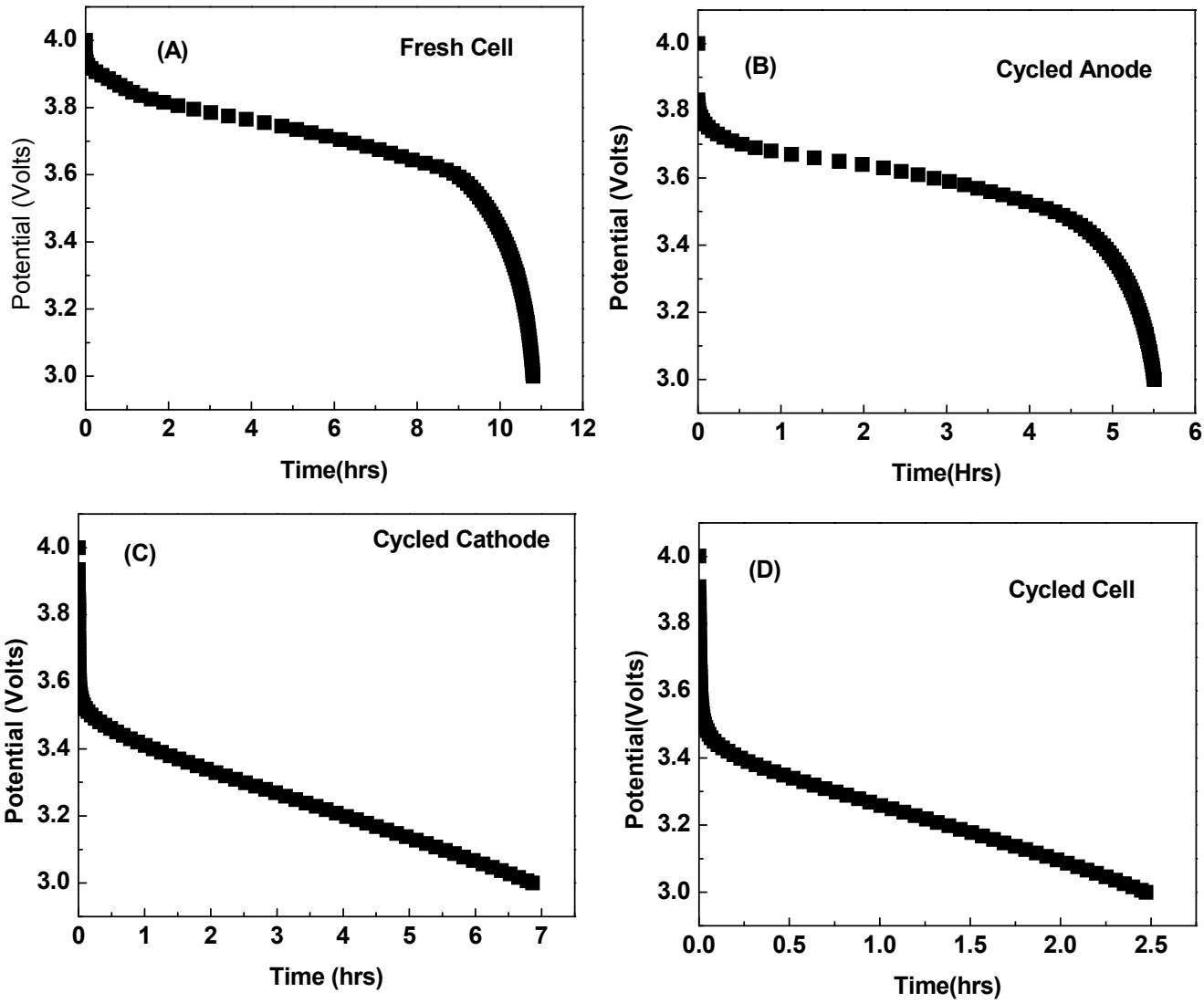

Figure 5.16: Discharge performance from T-Cell (a) Pristine Anode | Pristine Cathode (b) Cycled Anode | Pristine Cathode (c) Pristine Anode | Cycled Cathode (d) Cycled Anode | Cycled Cathode

EIS analysis was also performed on the composite cells with all the various configurations shown in Figure 5.15(a)-(d). It can be observed in Figure 5.17b, that the impedance of the pristine composite cell is similar to the full pristine cell which contains a high frequency semi-cycle associated with surface films, mid-frequency semi-cycle associated with the charge transfer process and 45° incline slope at low frequencies which is ascribed to solid state Warburg impedance. A composite cell was also assembled with electrolyte from the pristine cell + the electrolyte from the cycled cell and the result show similar impedance spectra compare to the pristine cell. We conclude that after continuous cycling the electrolyte including the ionic concentration remain relatively stable. The composite cell comprising cycled anode + pristine cathode has a charge transfer resistance increased by a factor of ~13 compare to the pristine cell. This increase in charge transfer resistance is related to deposition of surface films on the graphite anode observed from the SEM micrograph in Figure 5.12b. The composite cells comprising cycle anode + cycled cathode and pristine Anode + cycled cathode show the largest increase in charge transfer resistance, a factor of ~22. In addition the impedance spectra also show a shift in diffusion processes to lower frequencies compare to the pristine + cycled anode composite cells. It is believed that pore blockage or material defects are the main reasons for this shift. This result is consistent with what was observed during galvanostatic discharge experiments which show that increase overpotential and reduce performance with cycling is attributed more to the Li_xCoO_2 cathode. The increase in electrode impedance would result in an increase in cell overpotential voltages. It is concluded that the overwhelming increase in cell impedance originates from the positive electrode.

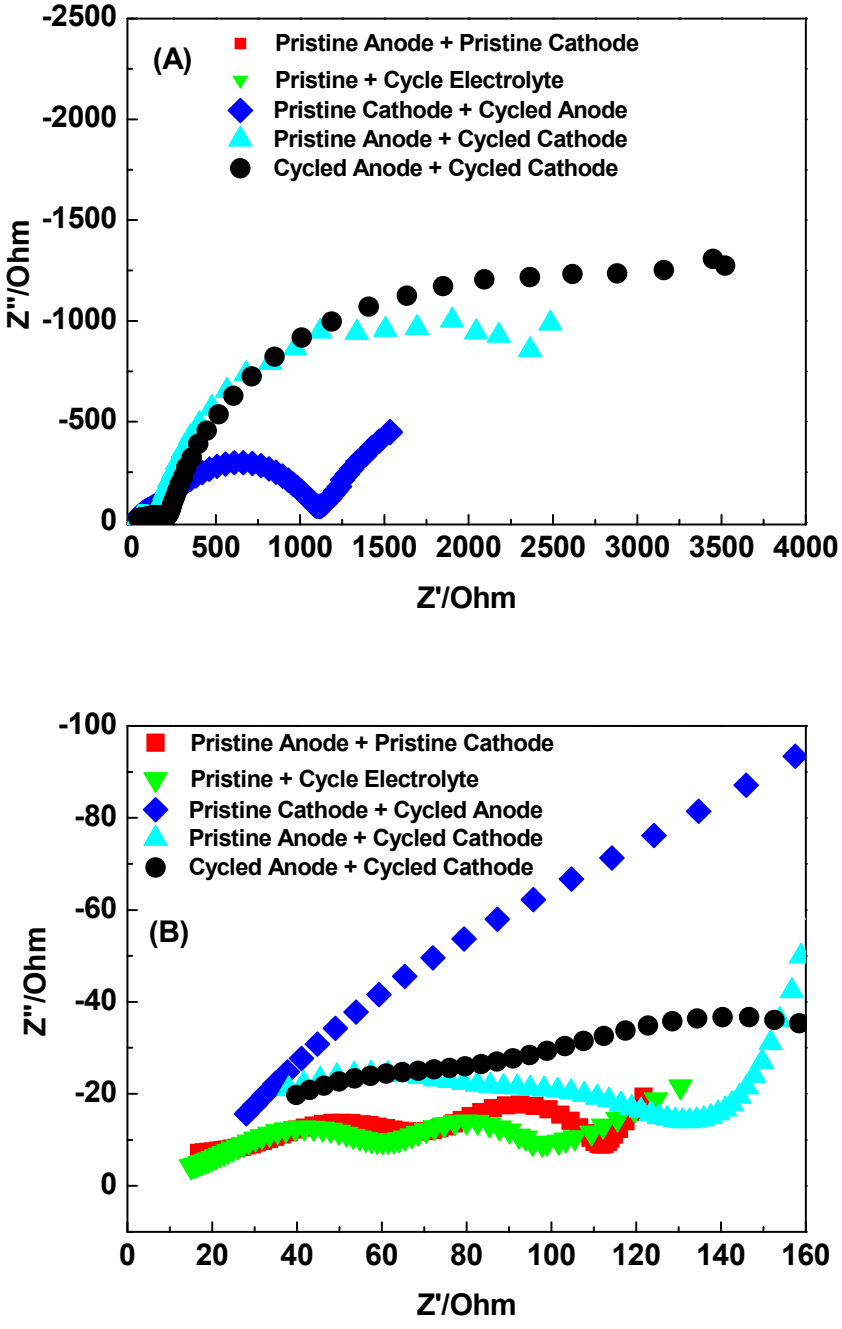

Figure 5.17: Impedance spectra for composites cells (a), (b)

5.4 Conclusion

Sealed lithium-ion polymer cell was investigated at room temperature using techniques of ac impedance spectroscopy and fitted to an equivalent circuit to estimate cell parameter with cycling. The discharge capacity was observed to decrease from an initial value of 771 mAh at a discharge current of 1C to 100 mAh after 3000 charge-discharge cycles at a discharge current of C/16. SEM and XRD were performed to investigate the morphological and structural changes in the negative and positive electrodes during continuous cycling. The resulting EIS data fitted to an equivalent circuit indicates that an increase in interfacial resistance R_{CT} and diffusion resistance R_W occur with increase cycling. These impedances play a key role in the rate of lithium-ion intercalation and are critical in determining cell efficiencies and reversible performance with continuous charge-discharge cycling. SEM analysis on the carbon anode electrode confirms the development of thick surface film during continuous cycling. It is believed that a major increase in interfacial resistance on lithium polymer cells is associated with the reduction of electrolyte species on the carbon electrode. These interfacial phenomenon's are believed to significantly influence cell efficiencies and reversible performance that result in capacity fading and the loss of power capability with continuous cycling.

XRD analysis on the electrodes shows no deterioration of the anode structure, however some structural changed were observed in the cycle cathode. In this case it is believed that the structural changes observed are significant enough to result in significant reduction in cell performance. Therefore we can conclude that the key reason for capacity fade and reduce cell performance of the lithium polymer batteries are the precipitation of surface films on the electrode due to the interaction of the electrodes and the electrolyte solution. SEM analysis revealed that these highly resistive surface films are more pronounce on the graphite anode surface resulting in increase electrode impedance. Half cell analysis, however, have shown that the cathode contributes more to capacity fade and reduce cell performance.

CHAPTER 6

DYNAMIC PPERFORMANCE OF Li-ION POLYMER BATTERY USING TRANSMISSION LINE MODEL

6.1 Introduction

The reduce availability of fossil fuels and increasing environmental concerns has spurred worldwide interest in the use of alternative energy supplies [11, 142]. Due to safety issues and the wide variety of shapes and sizes required for various portable applications, much attention has been focused on the research and development of advanced lithium-ion and lithium-ion polymer systems with increase energy and power densities [143-146]. Lithium-ion polymer batteries are capable of large energy storage, and therefore, they are predicted to play an increasing role as alternative energy and power sources, particularly in hybrid-electric vehicle applications. Optimization of battery performance is determined by various material properties. Therefore, modeling the effects of transport properties on electrochemical performance can result in improved cell design, reduce testing time and accurate modeling of battery behavior which is required for embedded power systems [147]. One of the primary challenges is the development of simple electrochemical models that are cost effective and can accurately predict important battery parameters, i.e. mechanisms that contribute to aging, battery run-time, power response and energy consumption. These parameters are critical to cell efficiency and should easily be implemented in circuit based simulator programs (e.g. Pspice, electronic workbench) for prototype evaluation and hardware optimization.

The galvanostatic charge discharge behavior of lithium-ion batteries was model by M. doyle et. al [148] using concentration solution theory which use a mathematical model to describe lithium-ion transport in three regions of operation. These regions include transport in solution, and the two solid phase of the composite electrodes for which boundary conditions are applied. Their mathematical model show accurate agreement in describing the charge discharge behavior of the electrochemical cell. However many of these models require a detail understanding of the complex physical and chemical process which may not be available or may not be understood by the electrical engineers [149]. Additionally to many engineers these equations present addition complexities that can significantly increase simulation time.

A time domain model mapped from impedance data in the frequency domain was developed by Buller et al. [150] which accurately modeled the dynamic behavior of an electrochemical capacitor and a lithium-ion battery. However for these models non-linear distribution properties in the low frequency portion of the impedance spectrum and battery run-time is not considered. These circuit based models are very useful and simple because they allow the complex electrochemical process to be replaced by simple electrical circuit which correlates well with battery dynamics.

The current model presented takes into account the non-homogeneous distribution properties of diffusion including the non-linear response to current magnitude and direction, i.e. positive and negative currents. The proposed model also includes an accurate representation of the DC nonlinear behavior in addition to the dynamic and transient response of the electrochemical cell under various load conditions. Additionally, similar techniques [151] proposed in previous work is used to elucidate the power and energy performance of the electrochemical cell. The model involves the non-linear mapping of impedance spectra for the electrochemical cell at various states-of-charge in the frequency domain to the time domain. A non-linear circuit which includes resistors, capacitors, inductors and non-linear electrical components are used to describe the cell at various equilibrium points. In this work, we focused our attention on modeling the performance of a lithium-ion polymer battery (UP3834562A) manufactured by Sony Corporation. This cell has typical electrode structure Li_xC_6 as negative electrode and $Li_{1-x}CoO_2$ as positive electrode material.

6.2 Experimental

Electrochemical impedance spectroscopy measurements were carried out on the polymer cell at various states-of-charge (SOC) using Solartron 1250B frequency response analyzer controlled by Zplot and Corrware software (Scribner Associated). The nominal capacity for this battery was 840 mAh at ambient temperature. Additionally, positive charge and negative discharge currents were used elucidate the dependency on charge transfer resistance R_{ct} on dc current. The frequency spectrum for this current work was limited to frequencies in the range 20 khz to 1 mhz, operating in galvanostatic mode with signal amplitude of 100 mA and I_{dc} form +0.8A to -0.8A in increment of 0.1A. Additionally, impedance spectra were performed in the bias potential window of 4.2V to 3.0V in increments of 0.2V. Impedance measurements were conducted only after the dc potential had a 6hr stabilization period at 25° C.

After collecting the experimental impedance spectrum, the various processes were fitted to an equivalent circuit using frequency limits from the experiment. The model is then validated by comparing the simulated and experimental voltage profile for several current pulse profiles.

6.3 Results and Discussion

6.3.1 Impedance Response of Li-Ion Polymer Battery

Figure 6.1 shows the result of the typical impedance spectra taken at 4.0V (84.3% SOC) for a fresh commercial polymer cell, where Z' and Z'' are the real resistance and reactant of the battery respectively. The impedance spectra compose an inductive tail at high frequencies relating to the porosity of the electrode [128, 143] and spirally wounded structure of the battery; The high frequency intercept (~1.262 kHz) on the real axis represents the total ohmic resistance (~ 0.12Ω) of the cell which includes the electrolyte resistance, contact resistance and electronic contacts, etc; depressed semicircles at mid to high-frequencies (25.18 to 502 Hz) can be ascribed to the solid electrolyte interface (SEI) layer of the electrodes (at the film electrode/solution interface); the semicircle in the mid-frequency (0.0796 to 25.18 Hz) range is characteristic of the charge-transfer kinetics at the electrode electrolyte interface [152,

153]; the low-frequency (0.0796 Hz to 1 mHz) portion of the impedance can be assigned to the solid state Warburg diffusion of lithium-ions into the porous material matrix. At extremely low frequencies (C_{int} = -1/ωZ", ω → 0) the impedance response is associated with the differential intercalation capacity of the electrode which describes the accumulation of lithium-ions within the host material [154].

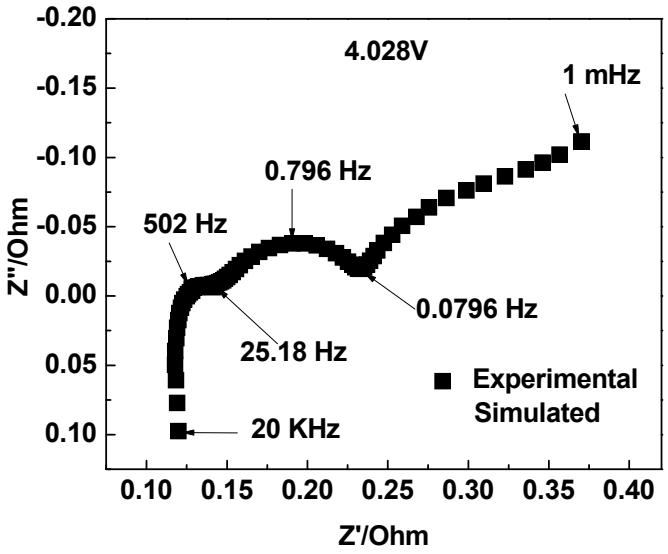

Figure 6.1: Nyquist plot of impedance spectra obtained at 4.0V (84.3% SOC)

To investigate the non-linear dependency of impedance on dc (I_{dc}) positive and negative charge-discharge currents, the impedance spectra shown in Figure 6.2 were collected in the frequency regime of 20 kHz to 0.1 Hz at 84% SOC. It can be observed that the charge-transfer resistance is strongly dependent on charge and discharge currents. A non-linear change in the charge transfer resistance was observed, which slowly increase with increasing negative discharge currents and decrease with positive charge currents.

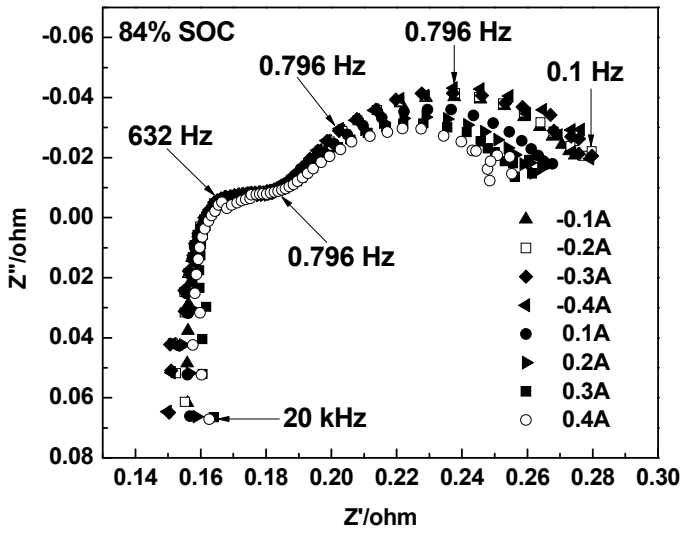

Figure 6.2: Impedance spectra at various charge-discharge currents.

6.3.2 Equivalent Circuit Modeling and Parameter Estimation

The charge transfer kinetic reaction between an ionic and an electronic conductor is inherently slow and can only proceed at an accelerated rate when the potential energy barrier between the two conductors has been overcomed by the reaction species [155]. This potential barrier is term *activation polarization* and is the rate limiting step for charge transfer between the electronic and ionic conductor. Generally the relationship between current density, the faradiac exchange current density and the electrode surface over potential η can be described by the Butler-Volmer equation which is given by [64]:

$$i = i_0 \left(\exp\left(\frac{n \cdot \alpha \cdot F}{RT} \eta \right) - \exp\left(- \frac{n \cdot (1-\alpha) \cdot F}{RT} \eta \right) \right) \tag{6.1}$$

Here, *i* is the current density i_0 is the exchange current density, α is the charge transfer coefficient, n is the number of electrons per molecule reduced or oxidized, F is Faraday's constant, R is the gas constant and T the absolute temperature in Kelvin. The two exponential terms on the right side of equation (6.1) represent the forward and reversible electrode reaction process respectively. At equilibrium potentials, the

exchange current density is the current exchanged between the ionic and electronic conductor [63].

The typical non-linear dependency of faradaic charge transfer resistance R_{ct} on current (i.e., positive and negative) was observed in the impedance spectra in Figure 6.2. The charge-transfer resistance at the electrode-electrolyte interface can then be determined by differentiating equation (1) and taking its reciprocal, which results in the following equation.

$$R_{ct}^{-1}(I) = \frac{\partial I}{\partial \eta} = \frac{I_0.n.F}{RT} \cdot \left(\alpha \cdot \exp\left(\frac{n \cdot \alpha \cdot F}{RT} \eta \right) - (1-\alpha) \cdot \exp\left(-\frac{n \cdot (1-\alpha) \cdot F}{RT} \eta \right) \right) \quad (6.2)$$

Similarly, the Warburg diffusive behavior that is usually observed in the low portion of the impedance spectra with 45° incline can be represented by a transmission line model having value given by [156]:

$$Z_W = R_W \frac{\coth\sqrt{i\omega\tau_d}}{\sqrt{i\omega\tau_d}} \quad (6.3)$$

Here, R_W is the effective distributed ionic impedance of the electrodes, τ_d is the diffusion time constant and ω is the angular frequency. Figure 6.3 (a) show the schematic representation commonly used for porous electrodes which consist cylindrical pore and the equivalent transmission line model purposed by de Levi [157]. Assuming uniform distributed double layer capacitance behavior along the inner wall of a cylindrical pore, then the classical 45° Warburg type response in the complex plane would be observed, (#4) [2, 66]. However the low frequency portion of the impedance spectra in the complex plane (Figure 6.1 and Figure 6.2) cannot adequately be model using the classical finite space Warburg (FSW) impedance element given by Equation 6.3. The non-linear diffusion response observed in the complex plane at low frequencies is believed due to the non-uniform diffusion properties of the electrodes which include particle size, pore size and shape (pore geometry), etc [134, 158-160]. Fig. 6.3 (b)

shows the typical impedance response for the various pore geometries, where low frequency arcs are observed (#2, #3, and #4).

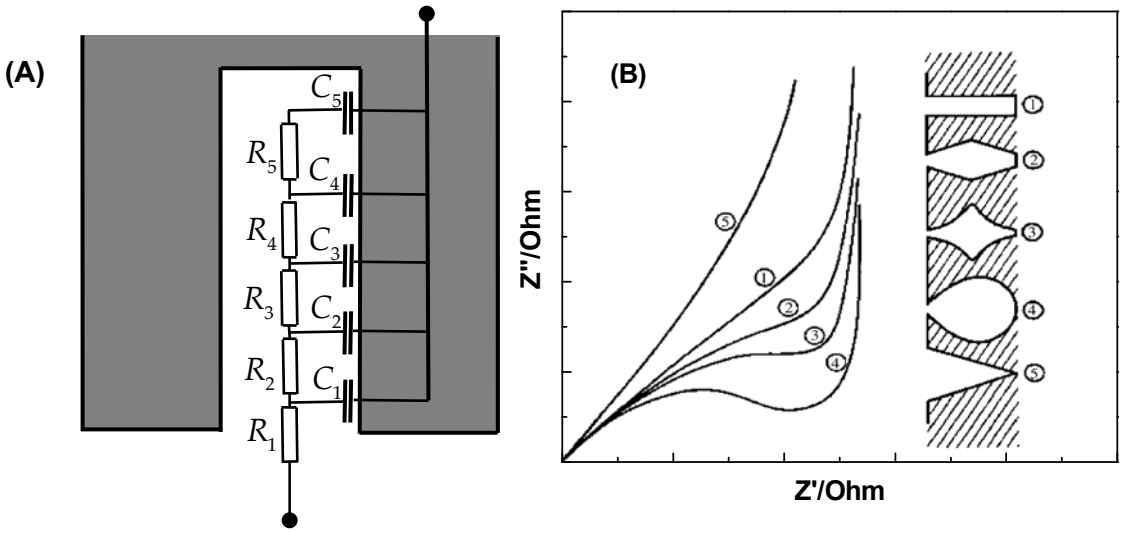

Figure 6.3: (a) Porous electrode with transmission line equivalent circuit representation (b) Impedance response for various single pore geometries. Source [2]

To more accurately model the low frequency portion of the impedance spectra which consists, non-uniform solid state diffusion of Li^+ under finite transmission lines condition with reflective boundary conditions, we adopted the equivalent circuit proposed by D. Levi et al [134] which consists the finite length Warburg (FLW) element (FLW) in series with intercalation capacitance, C_{int}. The governing equation for the FLW element can be expressed in terms of the distributed impedance of a transmission line containing three parameters with well defined physical meaning and is given by equation (7.4) [115].

$$Z_W = R_W \frac{\tanh\left(\sqrt{j\omega\tau_d}\right)}{\sqrt{j\omega\tau_d}} \qquad (7.4)$$

Here, R_W is the ionic impedance of the porous electrode, $\tau_d = \ell^2/D$ is the diffusion time constant with D as the diffusion coefficient, ℓ is the length of the diffusion region in the

electrode and ω (rad/s) is the angular frequency. The major difference between the FSW and the FLW element is that the later resembles a resistor at low frequencies and the former a capacitor, shown in Figure 6.4.

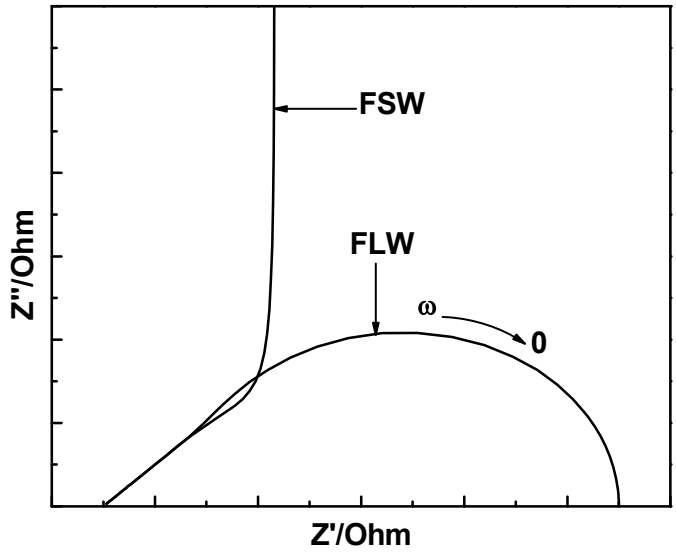

Figure 6.4: Impedance representation of finite-state and finite-length Warburg elements.

Figure 6.5 shows the equivalent circuit used to fit the ac impedance spectra at a range of potential voltages from 3.42V to 4.15V (measurements were taken at open circuit potential after a 6hrs rest period) and is shown in Figure 6.6. The impedance of the porous electrodes can be represented by a modified Randle equivalent circuit which consist series resistance R_s that represents the ohmic resistance of the battery, including the electrolyte, electronic contacts, and bulk particle, etc; R_n and C_n describes the slow migration of Li^+ through the surface films on the electrode surface [134, 152, 153, 161, 162]; R_{ct} and C_{dl} represents the faradaic charge transfer resistance and double layer capacitance of the electrodes, respectively. The solid-state diffusion of Li^+ is described by the FLW (finite length Warburg) element, while the accumulation of Li^+ within the electrode matrix is described by intercalation capacitance C_{int}. The effective impedances including charge transfer resistance R_{ct} and diffusion impedance Z_W of the anode and the cathode cannot be separate and resolve into their individual spectrum

therefore, their impedances are lump together to effectively represent the total impedance of the electrochemical cell [163].

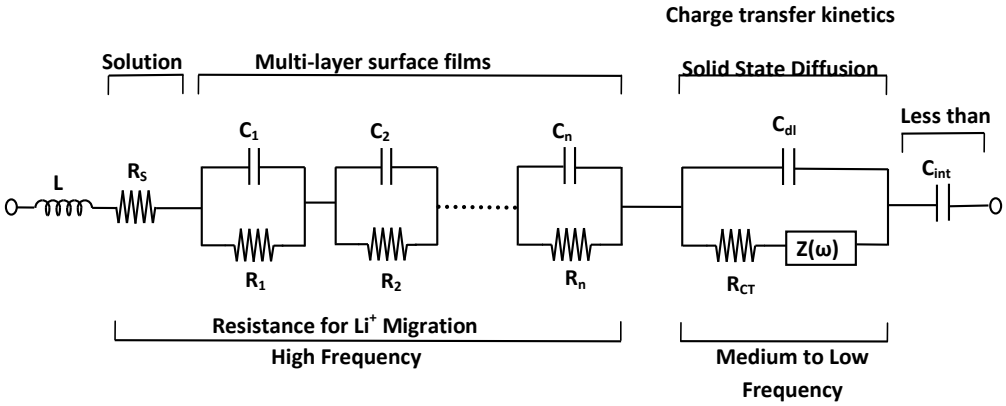

Figure 6.5: Equivalent circuit used to model the impedance spectra

The parameters in the circuit were determined by the method of non-linear least square (NLLS) fitting procedure. The solid lines which result from simulations show a relatively good agreement compared to the experimental impedance spectra over the hold range of frequencies. A non-linear least square algorithm was used to optimize the relevant parameters in the equivalent circuit. The use of intercalation capacitance C_{int} in the model takes into account the accumulation and consumption of Li^+ that result in the variation of open circuit potential with SOC. The Warburg diffusion impedance in the complex plane occurs with a distinguishable and non-overlapping time constant therefore, the Warburg impedance in this model can be placed in series with the parallel faradiac charge transfer resistance and double layer capacitance. From the experimental impedance spectra shown in Figure 6.6 (a) - (d), good agreement can observed over a wide range of frequencies and SOC.

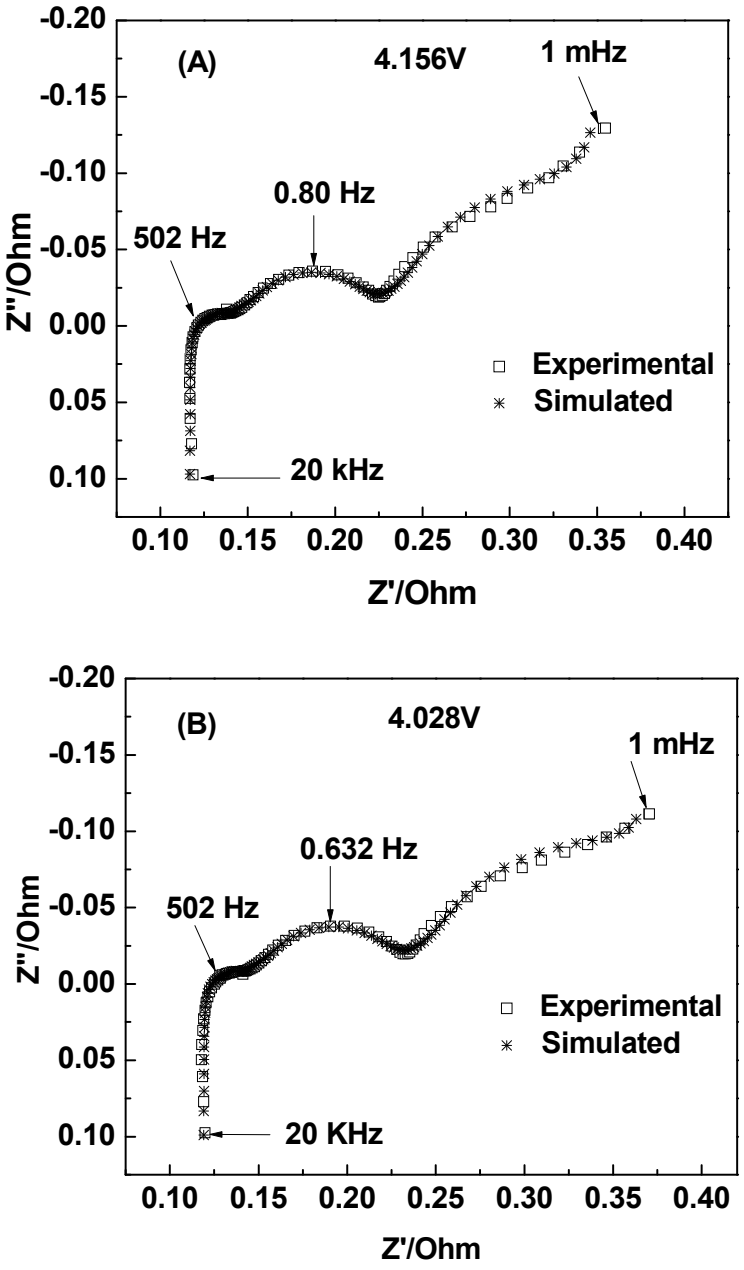

Figure 6.6: (a)(b) Impedance at various open circuit voltages. Impedance was simulated using the circuit from Fig 6.4 in the frequency range 20 kHz to 1 mHz.

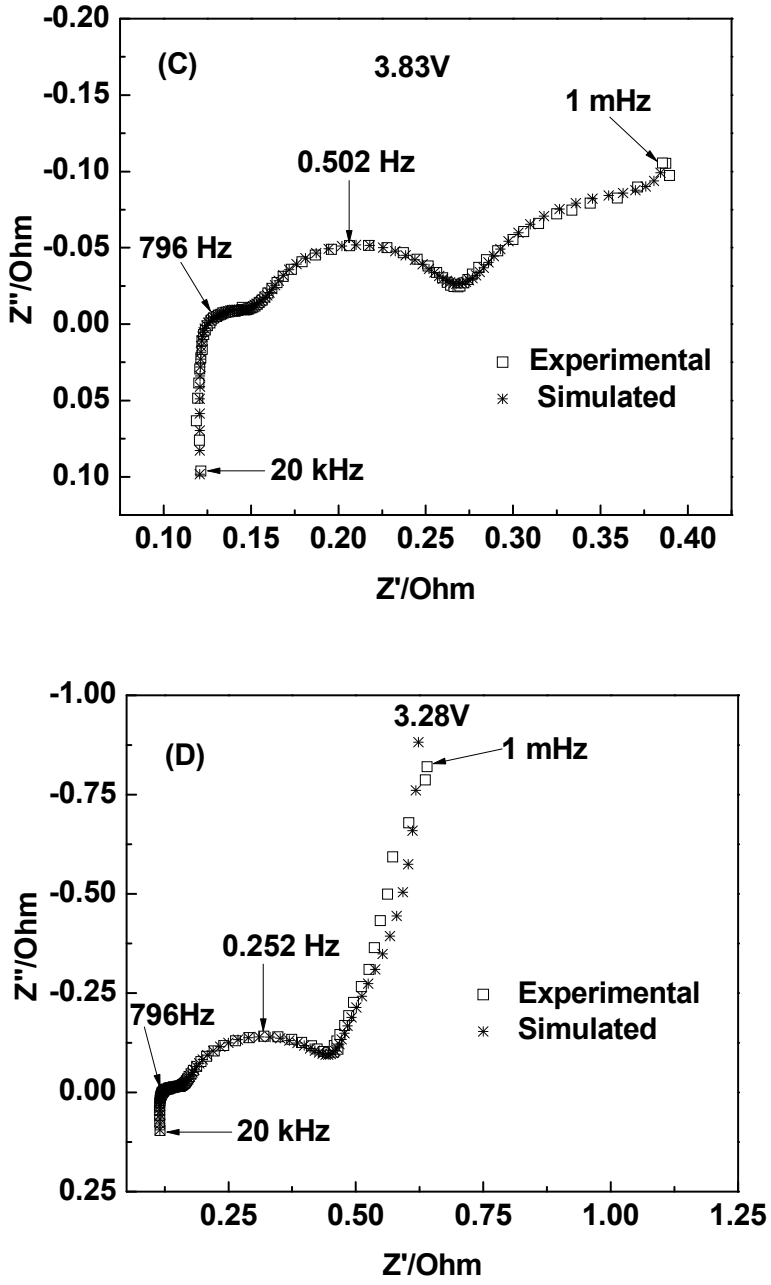

Figure 6.7: (c)(d) Impedance at various open circuit potential voltages. Impedance was simulated using circuit from Fig 6.4 in the frequency range 20 kHz to 1 mHz.

The simulation of the non-linear change of R_{ct} with various SOC and dc (I_{dc}) currents is shown in Figure 6.7. Equation (6.2) can be used to estimate the charge transfer resistance as a function of charge-discharge currents. These curves were constructed using parameters arbitrarily assigned similar to [156], i.e., $\alpha = 0.64$, $n = 0.62$ and I_0 a function of SOC. The results show that equation (6.2) can be used with great accuracy to calculate R_{ct}. A minor dependency on parameters relating to ohmic resistance R_s, surface film resistance and capacitance R_n and C_n, was observed at various SOC.

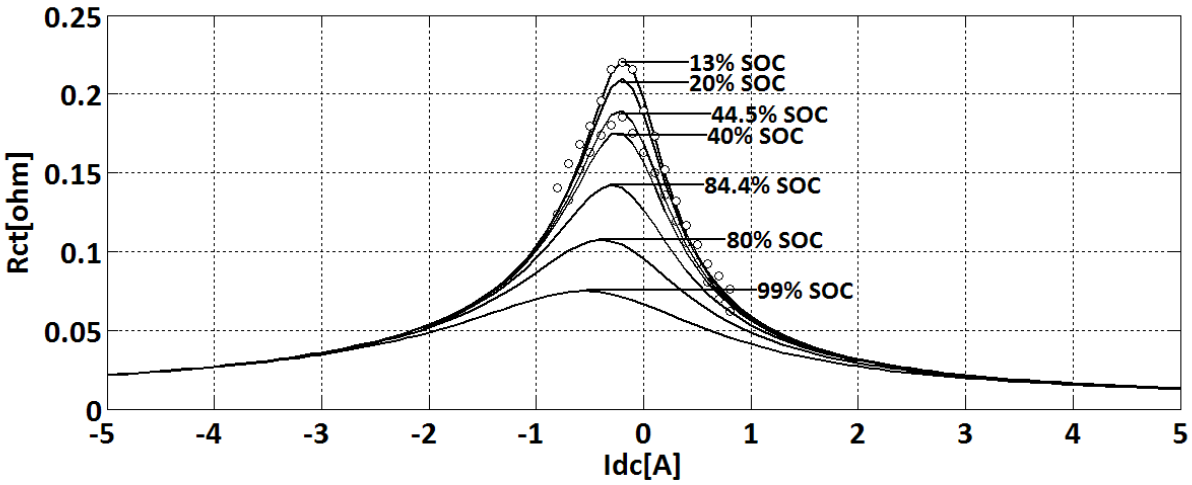

Figure 6.8: Non-linear change in charge transfer resistance R_{ct} at various SOC (25°C) and charge-discharge currents (o-Experimental data)

The optimum values of the complete impedance parameters at various SOC (99%, 87.85%, 59.78%, 7.31%, 2.88% and 1.33%) and I_{dc} = 0 is summarized in table 6.1. The results show that the elements are SOC dependent, however the charge transfer resistance show the most significantly dependency on SOC. It should also be noted that the solution resistance R_s and double layer capacitance C_{dl} show minimal variation with state of charge.

Table 6.1: Fitted parameters with state-of-charge variation

Idc	0A					
SOC	99%	87.85	59.78%	7.31%	2.88%	1.33
L(uH)	0.7769	0.792	0.78722	0.49685	0.50253	0.756
R_s (mΩ)	116.96	119.0	120.56	82.074	88.106	115.5
R_{f1} (mΩ)	10.498	10.49	13.122	14.998	15.596	17.11
R_{f2}(mΩ)	13.015	13.01	14.02	17.92	19.874	22.41
R_{f3}(mΩ)	12.759	12.75	11.785	15.654	16.279	19.09
C_{f1}(mF)	12.593	12.59	11.672	8.2548	8.4584	10.44
C_{f2} (mF)	93.656	93.65	105.74	98.663	96.163	123.0
C_{f3} (F)	1.361	1.361	1.421	1.989	1.699	1.996
C_{dl} (F)	2.700	2.624	2.528	2.635	2.578	2.576
R_{ct} (mΩ)	63.236	67.76	97.347	211.30	237.44	258.3
R_w (mΩ)	139.67	152.1	138.03	165.51	157.98	204.7
Tau	120.7	129	124.9	110.9	103.5	118.3
P	0.5	0.5	0.5	0.5	0.5	0.5
C_{int}	1669	2269	2429	613.4	319	191.3

The experimental data points for each circuit element in table 6.1 can be estimated by inserting parameter value with SOC in a lookup table. Equations obtained from fitting can also be used, which related the continuous charge in magnitude of each element to the change in battery state of charge. These equations can then used in a numerical simulator to represent the polarization impedance for mass and charge transport processes. In this particular experiment the latter was chosen. The change in magnitude for each element with state of charge in addition to linear and non-linear curve fitting is shown in Figure 6.8 (a) - (h). The solid line represents the estimated change in magnitude of parameter with SOC using the inserted equations. The observed plots from fitting are closely matched to the discrete experimental data points obtained from impedance measurements. Note that the charge transfer resistance not only depends on SOC but also on the current magnitude and direction, therefore it is omitted from the following figures. Parameters with minimal SOC dependency can be set to constant values during charge-discharge simulations.

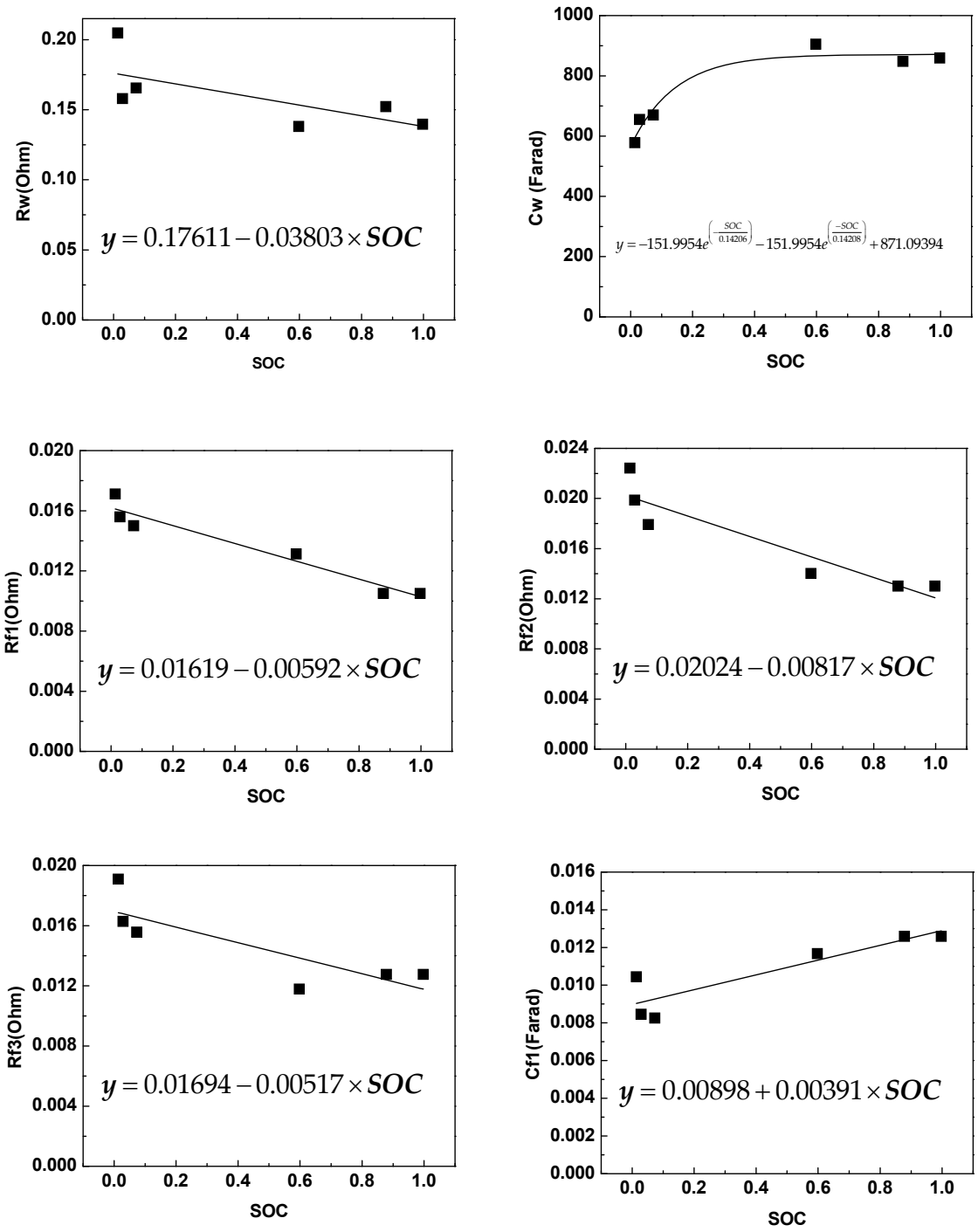

Figure 6.9: Estimate of change in circuit parameters with SOC

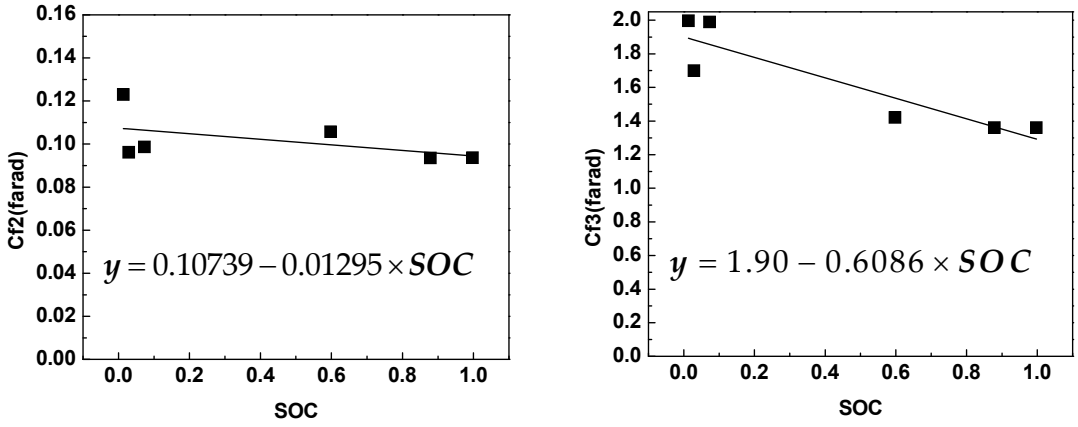

Figure 6.10: Estimate of change in circuit parameters with SOC

6.3.3 Transmission Line Model Li-Ion Polymer Battery

According to our previous analysis the FLW element is a suitable approach to describe the low frequency portion of the impedance spectra which consists solid state diffusion of lithium-ions and charge accumulation in the electrode matrix at low frequencies. To illustrate the use of this impedance model in real time application requires the time domain representation of the impedance spectra in the frequency domain. According to ref. [115] the impulse response of the Warburg impedance in equation (6.4) is given by:

$$\frac{k_2}{\sqrt{j\omega}}\tanh\left(\frac{k_1}{k_2}\sqrt{j\omega}\right) \bullet\text{-o} \frac{2k_2}{k_1}\sum_{n=1}^{\infty}\exp\left(\frac{(2n-1)^2\pi^2k_2^2}{4k_1}t\right) \tag{6.5}$$

Comparing the parameters on the left side of equation (6.5) to equations (6.4) leads to constant values for k_1 and k_2.

$$k_1 = \frac{\tau}{C_W} = R_W \tag{6.6}$$

$$k_2 = \frac{\sqrt{\tau}}{C_W} = \sqrt{\frac{R_W}{C_W}} \tag{6.7}$$

The impulse response for a simple parallel R-C circuit shown in equation (6.8), has the same characteristic response as that of equation (6.5). Therefore, from the comparison of the two equations it is possible to represent the Warburg impedance as a series combination of parallel connected R-C circuit elements.

$$\frac{1/C}{j\omega + 1/RC} \bullet\text{-o} \frac{1}{C} \exp\left(\frac{-t}{RC}\right) \tag{6.8}$$

Comparing the constants in equations (6.8) with those in equation (6.5) lead to values for the resistors and capacitors in the parallel R-C network, which is given by:

$$C_n = \frac{k_1}{2k_2^2} \tag{6.9}$$

$$R_n = \frac{8k_1}{(2n-1)^2 \pi^2} \tag{6.10}$$

The equivalent R-C circuit that can describe lithium-ion diffusion is depicted in Figure 6.9. The discrete components are distributed over the length of the network. The more voight elements that are added to the network the higher the order of accuracy in the dynamic response.

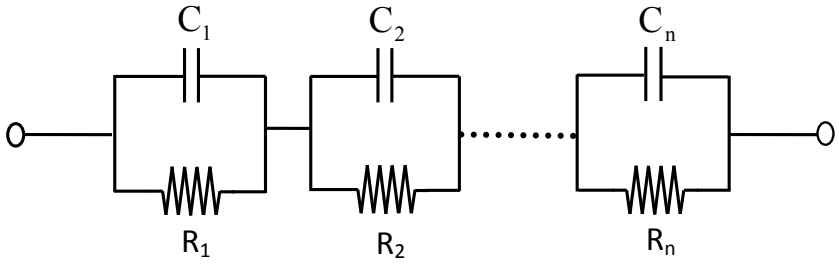

Figure 6.11: Parallel R-C circuit used to approximate lithium-ionic diffusion

The equation that describes the voltage behavior across each parallel R-C network is given by:

$$v_n(t) = I_L \times R_n \times \left(1 - e^{-\frac{t}{R_n C_n}}\right) \tag{6.11}$$

Figure 6.10 presents the complete representation of the electrochemical system using discrete non-linear electrical components. The equilibrium potential shown in Figure 6.9 is model by a SOC dependent voltage source U_0[SOC] which depends on the availability of active material or energy stored in the electrodes [164]. This dependent voltage source can be determined by charging the cell to various SOC, then after a rest period of 6hrs fixed values of the open-circuit-voltage (OCV) is stored in a look-up table [156]. The disadvantage of using this method for SOC estimation is that it can be time consuming and dependent on other factors, e.g. temperature, age, pressure and history of operating point. However, these additional dependent factors are not considered in this model. For this experiment, the OCV shown in Figure 6.12 was determined experimentally at operating point after a rest period of 6hrs using CC-CV charge protocol and a cutoff current of 50mA.

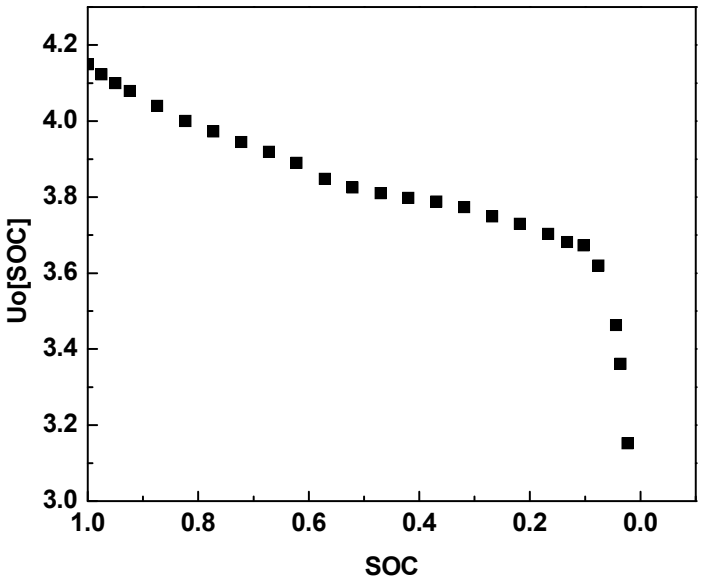

Figure 6.12: Dependency of open circuit voltage (OCV) on state of charge (SOC)

Equation (6.12) shows one common technique employed to estimate SOC. This simple technique better known as columbic counting (i.e. current integration) relates the charge or current drawn from the cell to the open circuit potential of the cell. The charge consumed during charge-discharge in a direct indictor of remaining SOC and is given by [165]:

$$SOC(T) = 1 - \frac{1}{3600 \times Q_0} \int_0^T i(t)dt - SOC(0) \tag{6.12}$$

Here, $i(t)$ is the charging/discharging current, $SOC(0)$ is the initial state-of-charge of the battery, and Q_0 is the nominal capacity of the battery with SOC $\leq$ 1. The battery is considered fully charge when SOC(T) = 1 which in this case correspond to an open circuit voltage of 4.17V.

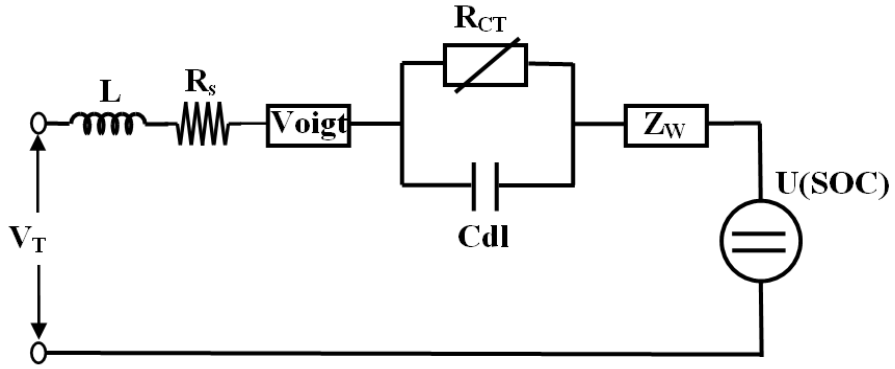

Figure 6.13: Schematic representation of lithium polymer battery derived from impedance response.

The dynamic load response to arbitrary load current can be described by the following equivalent circuit in Figure 6.10. In this equivalent circuit the “voigt” element describes the depress semi-circles observed at the high frequency in the impedance spectra and can be approximated by three R-C circuit elements. The terminal voltage can then be described by the following equation:

$$V_T = U_0[SOC(t)] - i_L \times R_s - \sum_n V_{fn} - L\frac{di_L}{dt} - R_{ct} \times i_L \times \left(1 - e^{\frac{-t}{R_{ct} \times C_{dl}}}\right) - V_w \tag{6.13}$$

Here, U_0[SOC(t)] is the open circuit potential of the battery, V_{fn} is the voltage drop associated with surface films at the electrode-electrolyte interface and V_w the voltage drop ascribe to the slow diffusion process. The effect of inductor voltage on the model is minimal because only pulse current or constant current charge-discharge is used in this model which will result in an inductor voltage zero.

6.3.4 Model Evaluation using Matlab/Simulink

To investigate the validity of the present model under constant current discharge and pulse load (i.e. charge-discharge) conditions the model was implemented in numerical simulator Matlab/Simulink. We applied several discharged current (C/10, C/4, 3C/4, 1C) at 100% SOC (Fully charged, ~4.15V) to the model until it reached a cut off voltage of 3.0V. Figure 6.13 shows the comparison between the experimental and simulated cell potential. The following characteristics were observed; at high and low discharge rates a steep voltage drop is observed reflecting the ohmic polarization of the cell, an almost linear region reflecting additional overvoltages, i.e. activation overpotential and concentration overpotential, followed by a very steep slope at the end of discharge which reflect the depletion in the available active material. The simulated terminal voltage in response to current demands, agrees accurately with the experimental result at high and low discharge rates.

In order to confirm the validity of the impedance model to large current pulse applications, step current profile (0.6A, 1s) to (-0.1A, 1s) to (-1A, 1s) to (0.5A, 1s) was applied to the test cell (UP383562A) at 94% SOC. The experimental and simulated voltage in response to step profile during a 20s time duration is depicted in Figure 6.14. In this range the experiment voltage varied from a maximum value of 4.14V to a minimum value of 3.78V. In addition, a maximum error of 1.9% between the experimental and simulated terminal voltage was observed. It can be observed that the experimental terminal voltage and simulated voltage response show relatively accurate agreement.

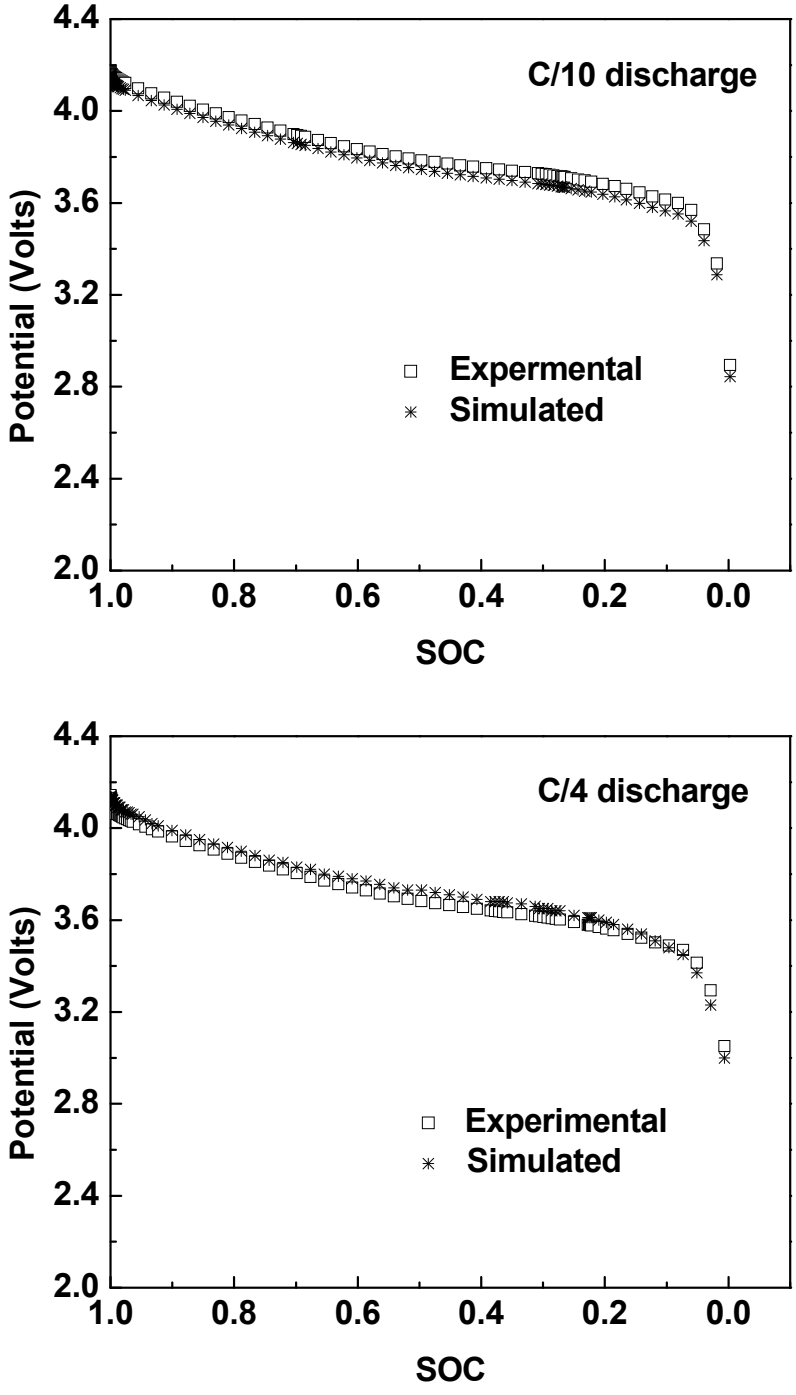

Figure 6.14: Dependency on battery voltage on SOC at several discharged currents (A) C/10, (B) C/4.

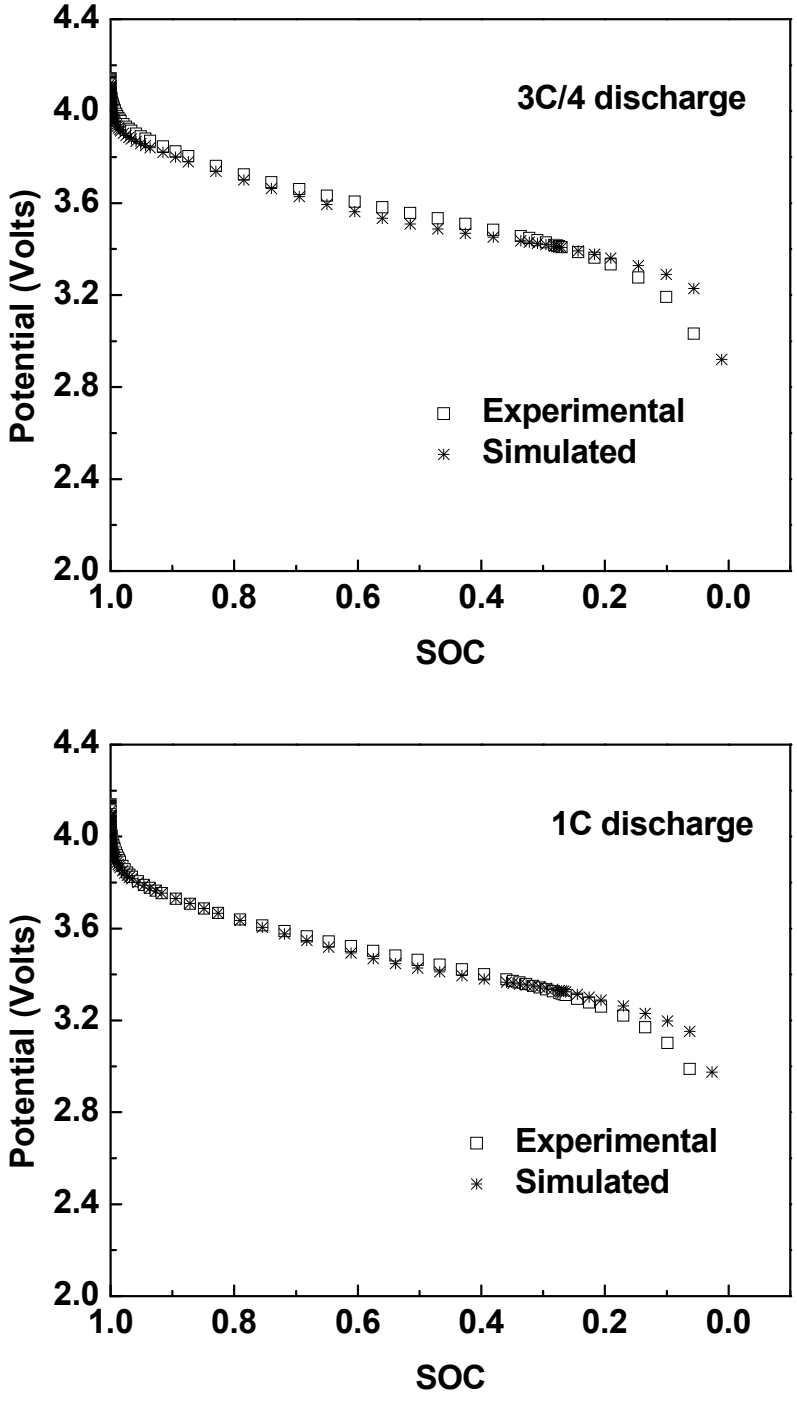

Figure 6.15: Dependency on battery voltage on SOC at discharged currents (C) 3C/4 (D) 1C.

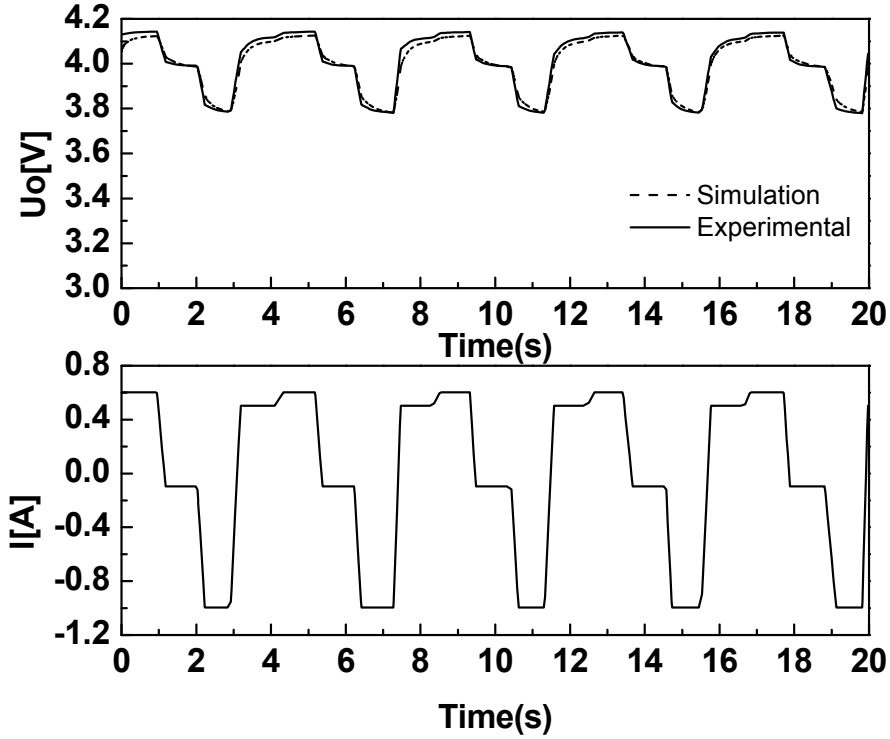

Figure 6.16: Terminal voltage in response to applied current pulse.

6.3.5 Power Performance Li-Ion Polymer Batteries

An important parameter for energy storage devices (ESD) in various application, include the optimization of energy and power densities. In addition to increase pulse power demands in digital communication devices and in Hybrid electric vehicles applications, batteries are expected to have increase energy densities capability. One method for comparing the battery capability to deliver both maximum power and energy is to use Ragone plots, which display on a log-log plane, the relationship between power and energy densities. From these plots, the optimum working point can be determined, which indicate where the power density (i.e. fast discharge) and energy densities (i.e. slow discharge) are highest [166]. Computer simulation can be a powerful tool for modeling ragone plots for which comparative analysis (e.g. performance) can be made between various batteries [167]. This can prove to be an efficient and effective method for choosing a battery for an application specific design.

For an ideal battery, i.e. without leakage, the energy delivered to a load can be described by the following equation [166]:

$$E = \frac{2R_S Q_0 P}{U_0 - \sqrt{U_0^2 - 4R_S P}} \tag{6.14}$$

Here, U_0 is the battery voltage, R_s is the ohmic impedance of the cell, P is the power delivered to the load and Q_0 the capacity of the battery. From equation (7.14) the maximum energy and power capability for the ideal ESD can also be determined and is given by:

$$E_{max} = Q_0 U_0 \tag{6.15}$$

$$P_{max} = \frac{U_0^2}{4R_s} \tag{6.16}$$

Batteries however, show strong non-linear behavior and are strongly dependent on material properties such as ohmic impedance (e.g. electrolyte conductivity, electronic contacts, etc.), ionic impedance, electrode thickness, and temperature, etc [125]. For ESD these properties can more accurately be mapped from impedance data to model the power and energy density relationship. From the equivalent circuit in Figure 6.11, which was mapped from impedance data in the frequency domain to the time domain, the energy and power density at the load can be defined by the following equations:

$$P = \frac{1}{m}\int_0^T U(t) \times i(t)dt \tag{6.17}$$

$$E = \int_0^T P(t)dt \tag{6.18}$$

Where m is the mass of the energy storage device, U(t) is the time dependent load voltage and i(t) is the time varying current which is dependent on the following equation:

$$i(t) = \frac{P(t)}{U(t)} \tag{6.19}$$

In order to evaluate the power and energy capabilities of Sony UP383562A LIP battery, Equations (6.17) and (6.18) were integrated into the equivalent circuit model of our battery, Figure 6.11. Simulation started at a maximum voltage of 4.15V (fully charged) then discharged to a cutoff voltage of 3.0V using constant power discharge i.e. the power is held constant by continuously adjusting the voltage and current. At the end of discharge the specific energy was determined using equations (6.18). To generate the Ragone plot from simulation, the measurements in the previous step were repeated using constant power discharge in the range 0.5 to 22 watts.

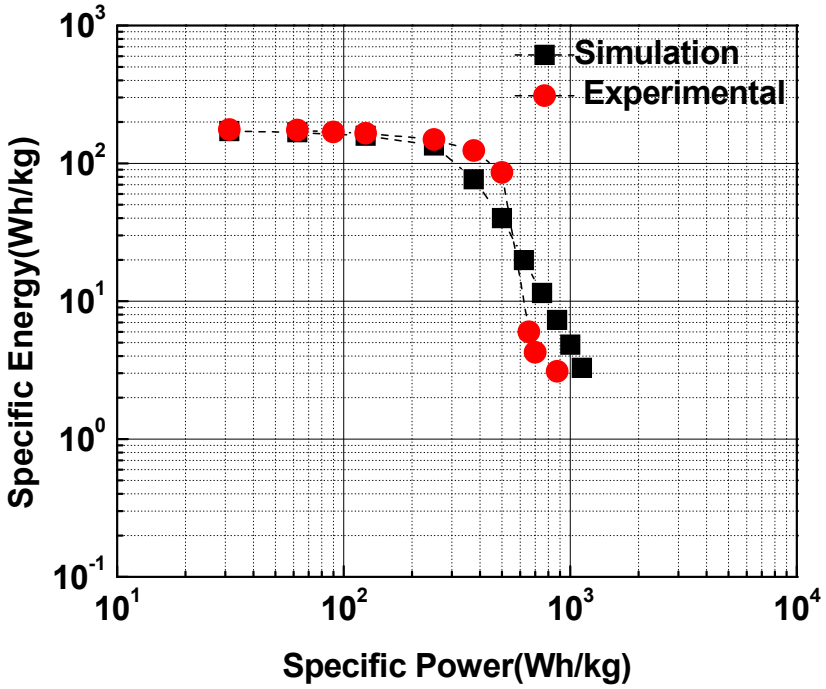

Figure 6.17: Computer simulation of Ragone plot for Sony UP383562A LIP cell

Figure 7.15 shows a Ragone plot (specific energy vs. specific power) which was generated from experimental and simulated data for cell UP383562A. From this plot key observations are made. Our simulation indicates that this cell can achieved a maximum energy density of ~171 Wh/kg compared to the experimental value of 167 Wh/g. To determine the Ragone plot experimentally, the cell was discharge from the fully discharge state (4.15V) for minimum discharge potential (3.0V) at constant current. From these discharge curves specific power and energy were determined and plotted in

Figure 7.15 alone with values obtained from simulation. The predicted maximum deliverable specific power obtained from simulation was ~1400 W/kg. The manufacture has rated the capability for this ESD to have maximum specific energy of 190 Wh/kg [126] for vanishing power levels during discharge.

6.4 Conclusion

A generalized impedance based model which takes into account non-homogeneous battery dynamics has been developed using non-linear lumped elements. Experimental results have demonstrated that the equivalent circuit in Figure 7.5 can accurately be used to model the dynamic and transient response of lithium-ion polymer batteries. The equivalent circuit model was obtained by collecting impedance data over a range of frequencies and SOC then the method of NLLS fitting was used for the optimization of circuit parameters. The charge transfer resistance R_{CT} was the only parameter observed to be a function of both SOC and current magnitude and direction. This relationship can be elucidated by conducting EIS analysis using a constant dc current with a small sinusoidal stimulus current superimposed. The time domain model can then be developed from the frequency response, which can adequately model the non-linear performance during pulse charge-discharge sequence and constant dc charge-discharge current. The terminal voltage can be described well theoretically over a wide range of potentials. The experimental results showed that computer simulation can be useful in understanding real time battery performance which can result in reduce cost and accelerated design cycle, optimization of battery software and hardware control for diverse applications. Additional, components of this model include accurately modeling battery run-time and correctly predicting the overall trend in specific energy vs. specific power densities (Ragone plot). It has also been shown that computer simulation can also be useful when device capability is limited, i.e. the ESD is in this experiment had a limited maximum discharge current, however, simulation doesn't have this limitation which allow the projection of power vs. energy at higher discharge rates.

CHAPTER 7

SUMMARY AND SUGGESTION FOR FUTURE RESEARCH

7.1 Introduction

The Li ion concentration in the electrodes and the capacity of the battery cells versus the number of charge/discharge cycles will be characterized by a computer controlled battery cycling system. This battery cycling system can be used at constant current, voltage, and power modes. The voltage and current profiles during the charge/discharge cycles will be recorded for capacity analyses. This system will also be used to determine the charge states of the battery cells for the *ex situ* high-resolution NMR experiments and the *in situ* STRAFI imaging experiments.

An ac impedance spectrometer will be used to characterize the impedance of the Li-polymer rechargeable batteries. The impedance spectrum provides some important physical information regarding the electrolyte degradation, dendritic growth, and SEI film formation at the surfaces of the electrode materials. The measured NMR data will be correlated with the physical and chemical properties of the battery cells in order to understand further the degradation mechanism of the Li-polymer rechargeable batteries.

We propose to investigate elements of Li^+ and their concentration inside lithium-polymer battery by using high resolution nuclear magnetic resonance (NMR). In this analysis individual components of the battery (Anode, cathode, polymer electrolyte) is place in a strong magnetic field B_o then irradiated with frequencies in the radio spectrum where the atomic nucleus is excite from ground state to a higher energy state . During the relaxation to the lower energy state an electromagnetic wave is reemitted at the

frequency of excitation. From this analysis, the chemical change and molecule structure and composition of materials can be reflected in NMR spectra measurements such as chemical shift and T1 of the ^{7}Li NMR signal. Other NMR spectral measurements such as ^{59}Co will provide addition information on cathode electrodes such as the valence of cobalt nucleus in the structure. Temperature dependence of T_1 measurements will also provide useful information about mobility of Li ions in the electrodes. Usually, Li ions in the reversible phases should be more mobile than that in irreversible phases. The high-resolution NMR spectra along with the nuclear spin-lattice relaxation times will provide the necessary information for later determining the pulse sequence during the in-situ STRAFI NMR imaging in order to distinguish the various compositions inside the battery cell. The in-situ STRAFI and high-resolution NMR spectra will be integrated together through the T_1 measurements.

7.2 TEM and SEM Analysis

SEM image and high-resolution TEM image, energy dispersive x-ray spectroscope (EDX), and selected area electron diffraction (SAED) will be used to identify the physical and chemical properties of the electrode and the electrolyte materials such as physical location, composition, and crystallinity of each phase material. In order to improve the interpretation of NMR spectra and microscopic images, other techniques including x-ray diffraction, ac impedance spectra, and dc charge/discharge cycling will be used to measure the crystalline structure, ionic conductivity, and Li ion concentration (or capacity) in cell, respectively. NMR and microscopic studies, in conjunction with these measurements, will greatly enhance the comprehensive understanding of irreversible phase formation in the Li rechargeable battery.

7.3 NMR Principle

The general principle of NMR is based on the interaction of an atomic nucleus that processes spin with that of an external magnetic field. The absorption of photons by irradiation with pulse radio frequencies (RF) in the electromagnetic spectrum can induce

a transition to a higher energy state. During relaxation to the lower energy state a detectable frequency is transmitted.

Considering an isolated proton (Figure 7.1) that processes spin I and angular momentum P. The relationship between the magnetic moment μ and the angular momentum can be expressed as

$$\mu = \gamma P \tag{7.1}$$

Where, γ is the magnetogyric ration that is dependent on the nuclei of interest. When placed in an external magnetic field B_0, the nuclear moment μ tend to align with direction of the magnetic field with nuclear magnetic moment μ that is related to the angular momentum.

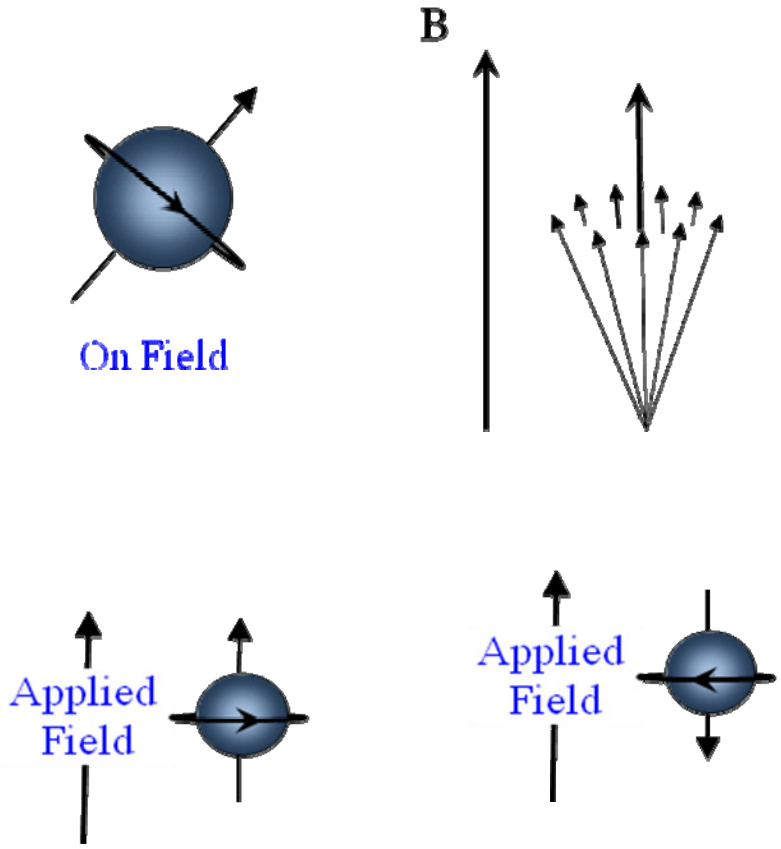

Figure 7.1: Schematic representation of an electron in a magnetic field.

7.4 NMR Analysis

The Li-polymer rechargeable battery cells will be charged at various potentials such as fully charged, fully discharged, or any given number of cycles by the battery cycling system. After charging to a given potential, the battery cell will be opened under an argon atmosphere in a glove box where the cathode and anode materials, as well as the polymer electrolytes of the cell are removed from the current collectors and then packed and sealed separately in different MAS rotors for the *ex situ* high-resolution ^{6}Li NMR measurements.

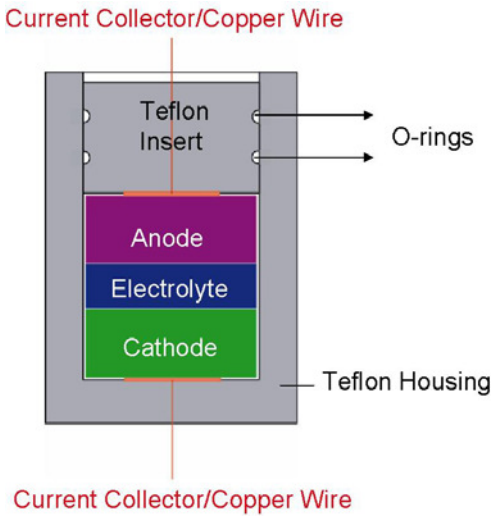

Figure 7.2: Schematic of electro-chemical NMR cell used for in situ experiment.

7.5 In Situ STRAFI NMR

For *in situ* STRAFI NMR studies, an electrochemical NMR cell will be specially designed for the *in situ* NMR measurements of an active or working battery cell. Figure 7.1 shows such an *in situ* NMR cell. Under an argon atmosphere, the active cell will be packed inside a Teflon housing after the metal container of the battery is removed. A Teflon insert with O-rings is then plugged in to a seal Teflon housing. The current collectors made of thin copper are positioned on the surfaces of the inner bottom of the Teflon housing and the inner side (facing the sample chamber) of the Teflon insert, as shown in Figure 7.1. The Teflon insert will be pressed tightly so that the current

collectors make effective contacts with the electrodes of the active cell. While the copper wires connect the current collectors in the *in situ* NMR cell to electronic poles, which will be extended to a potentiostat or a battery cycling system, which is stationed outside the NMR magnet, allowing for the charge/discharge cycling during NMR measurements.

7.6 In Situ ^{7}Li STRAFI NMR

Different from the *ex situ* NMR analyses, where the anode, cathode, and electrolyte materials are separately extracted from a battery cell at different charge potentials, *in situ* NMR [168-170] will allow one to monitor lithium ions activities in an intact battery cell, eliminating uncertainty associated with different starting specimens and electrochemical cells at different charge potentials as used in the *ex situ* NMR experiments. So far, the *spectroscopic* method has been proposed in the *in situ* ^{7}Li NMR [168-170], in which an active or working battery cell is stationed in the center of the homogeneous magnetic field and the wide-line NMR signals are observed during the charge/discharge process. However, since the high-resolution spectra cannot be available using such an *in situ* NMR spectroscopic method, the resulting NMR resonances from the different chemical formations in the battery cells are severely overlapped. Consequently, it becomes difficult to unambiguously identify the changes of the chemical formations upon the charge/discharge process.

The most important aspect in the studies of the degradation of the rechargeable batteries is to know where and what kind of irreversible processes occur at the electrodes and/or electrolyte during the charge/discharge cycling. Here, we propose a novel *in situ* STRAFI NMR spectroscopy (this is an imaging method, rather than the spectroscopic method) to study the Li-polymer rechargeable battery cells. In STRAFI experiments, a battery cell (stationed in the sample chamber of the STRAFI probe head) is placed at the maximum field gradient (e.g., 75 T/m at the 830 MHz magnet, which is much stronger than the gradients typically used in magnetic resonance imaging experiments, rather than in the center of the magnet that exhibits the most homogeneous magnetic field strength). In such a strong field gradient, an excitation pulse can only excite the Li ions within a very thin slice along the field gradient. By

translating the battery cell vertically (through computer-controlled vertical movements of the probehead), the Li ions population can be detected in the thin slice along the field gradient. Figure 7.3 shows the preliminary ^{7}Li STRAFI imaging of a fully charged Li-rechargeable battery cell. This STRAFI imaging profile shows clearly the existence of the Li ions in the cathode even in the fully charged state, which is consistent with the results obtained previously [171, 172].

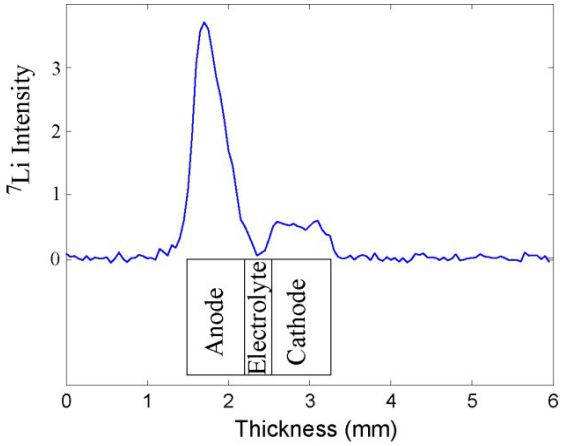

Figure 7.3: ^{7}Li STRAFI imaging of the fully charge $Li_xV_2O_5$ rechargeable battery cell obtained on the ultra-narrow bore 830 MHz magnet using an existing STRAFI probe. The units on the vertical scale are arbitrary.

Interestingly, Figure 7.3 also indicates that in the fully charged state, the Li ions are uniformly distributed in the cathode host but not in the anode host. Such Li ions distributions can hardly be detected by any other techniques. Thus, the STRAFI method allows us to map the ^{7}Li ion concentrations across the anode, electrolyte, and cathode planes. When an active battery cell is placed in an *in situ* NMR cell, the *in situ* STRAFI NMR spectroscopy is capable of visually observing the *in situ* migrations of the Li ions across the anode, electrolyte, and cathode planes in the active battery cell during the charge/discharge cycling. The *in situ* STRAFI NMR spectroscopy proposed here provides a unique opportunity, over other techniques, to detect where and what kind of irreversible processes occur at the electrodes and electrolyte during the charge/discharge cycling.

The existing STRAFI system on the 830 MHz (19.6 T, 29 mm extra-narrow bore superconducting magnet) includes a STRAFI NMR probe, a mechanic control unit that moves the STRAFI probe-head in the vertical direction at 1.56 μm per step using a stepper motor, and an interface between the NMR spectrometer console and the stepper motor. The spatial resolution was about 17 μm for ^{7}Li nucleus (versus 200-1000 μm for the thickness of the electrodes and electrolyte) and is strongly affected by the excitation pulse, field gradient, gyromagnetic ratio, as well as the step resolution and the accuracies of the stepper motor and the mechanic control unit. In this proposal, we will first modify the existing STRAFI system for the *in-situ* ^{7}Li NMR STRAFI experiments. Such modifications include an electrical charge/discharge in the probe, an update of the stepper motor for a better step resolution, and an electrical control unit for the charge/discharge cycling. After the modifications, we will then fabricate the *in situ* NMR cells and perform the *in situ* NMR measurements. The results will be correlated with the material properties and electrochemical processes.

7.7 Dynamic Battery Model

For various applications it is necessary to be able to predict the cycle life and dynamic behavior of an electrochemical cell. A dynamic battery model has been developed from ac impedance spectra analysis that can incorporate mechanism of capacity fade with continuous cycling. Mechanism of capacity fade in the solid electrode and in electrolyte phase will be incorporated into the dynamic model to aid in the prediction of the performance of the cell. Understanding the various mechanisms that leads to irreversible changes, capacity fade and reduce performance with cycling from NMR and SEM will further aid in the development of more accurate models to predict cell failure with continuous cycling. The purpose of this model will further help to, (i) answer the question on how various operation conditions and constraints affect the rate of capacity fade in an effort to design better battery materials with better efficiency; (ii) reduce cost and experimental time by using computer simulation; (iii) selection of battery from manufacture for application specific design [135].

APPENDIX A

PAPER PUBLISHED MAY 31 2007 IN THE JOURNAL OF THE ELECTROCHEMICAL SOCIETY

TRANSMISSION LINE MODEL FOR DESCRIBING POWER PERFORMANCE OF ELECTROCHEMICAL CAPCITORS

Journal of The Electrochemical Society, **154** (11) A1020-A1025 (2007)
0013-4651/2007/154(11)/A1020/6/$20.00 © The Electrochemical Society

Transmission Line Model for Describing Power Performance of Electrochemical Capacitors

P. L. Moss,[a,*] J. P. Zheng,[a,*,z] G. Au,[b,*] P. J. Cygan,[b] and E. J. Plichta[b,*]

[a]*Department of Electrical and Computer Engineering, Florida A&M University and Florida State University, Tallahassee, Florida 32310, USA*
[b]*U.S. Army CERDEC, Fort Monmouth, New Jersey 07703, USA*

A simple equivalent circuit model for electrochemical (EC) capacitors can be established based on electrochemical impedance spectroscopy. The circuit consists of an ohmic resistor and a finite-length Warburg element in series. The EC capacitor's performance including the transient/pulse response and energy density as a function of power density (Ragone plot) can be stimulated by the equivalent circuit model with three useful parameters including an ohmic resistance, total ionic resistance, and total capacitance of the electrodes.
 [DOI: 10.1149/1.2778126]

Manuscript submitted May 31, 2007; revised manuscript received July 11, 2007. Available electronically September 12, 2007.

Electrochemical (EC) capacitors are increasingly being used as electrical energy storage devices in a variety of applications due to their unique characteristics; these include higher energy densities compared to conventional dielectric and electrolytic capacitors, and greater power densities and cycle life compared to rechargeable batteries.[1-6] Great efforts have been focused on increasing the energy density of EC capacitors including, optimization of the specific surface area and pore size of the activated carbon for increase double-layer capacitance;[7-10] the development of pseudocapacitance electrode materials for increased energy storage per unit volume;[11-16] lately, the introduction of asymmetrical cell configuration.[17-21] The theories on energy density of EC capacitors were also developed and successfully applied to double-layer capacitors and asymmetrical cells.[22-26] The theoretical maximum energy density of EC capacitors and asymmetrical cells can be projected based on some basic parameters such as specific capacitance (or capacity) of the electrode, salt concentration in the electrolyte, and operational voltage of the cell. The energy density theories can be used not only for predicting the maximum energy density of the capacitor but also to provide design parameters for achieving the maximum energy density. The parameters include the mass (volume) ratio between the electrode and electrolyte, porosity of the electrode for double-layer capacitors, and mass ratio between capacitive and battery electrode materials for asymmetrical cells. From the energy density theories, it was found that for most current developed systems, the theoretical energy density was mostly limited by the salt concentration in the electrolyte.

The power density of the EC capacitor is determined by the internal resistances which include the electrical and ionic resistances. The detailed resistance distributions for EC capacitors with both bipolar and spiral-wound structures were investigated.[27,28] The sources of electrical resistance originate from the bulk resistance of the electrode material, contact resistance between activated carbon particles, current collector, and contact resistance between the carbon electrode and current collector. The sources of the ionic resistance are separator paper and ionic resistance in the porous electrode. The experimental results also demonstrated that the ionic resistance was a function of capacitor voltage, because the free ion concentration in the electrolyte decreased with the buildup of double-layer charges as capacitor voltage increase. However, even when the sources of internal resistance can be identified, the power density and the internal resistance of the double-layer capacitors cannot be related. The maximum peak power of the capacitor was sometimes defined as the total energy divided by the internal resistance of the capacitor. It is also widely accepted that the best way to define the capacitor's performance is by using a Ragone plot,[3,29,30] which describes the relationship between the energy density and power density. Currently, the Ragone plot can only be obtained experimentally, and no model or theory exists to predict the relation between energy and power densities based on some basic parameters which can be easily obtained experimentally.

In this article, we are going to demonstrate that an equivalent electrical circuit model can be established based on electrochemical impedance spectroscopy (EIS). The model consists of an ohmic resistance which represents all internal resistance within the capacitor except the ionic resistance from the porous electrode. It is demonstrated that the total capacitance obtained from the equivalent circuit model is consistent with the capacitance values measured by dc charge-discharge method. It is also demonstrated that the model can be used to describe the transient behavior of the capacitor, and to project the energy and power densities relationship.

Experimental

Electrochemical impedance spectroscopy (EIS) measurements were carried out for a Panasonic electrochemical capacitor (2.5 V, 10 F: o.d. = 18 mm, L = 35 mm) using a Solartron 1250B frequency response analyzer with windows PC control and data acquisition software by Zplot (Snibber Associates). All spectra were collected at open circuit voltage using a 5 mV sinusoidal stimulus with frequency ranging from 10 mHz to 20 kHz in the potential range of 0–2.5 V with spectra collected in increments of 0.5 V. The spectra are then fitted to an equivalent circuit using Zview software.

The dc charge-discharge was performed at constant current mode when the capacitor was charged and discharged between 0 and 2.50 V at ±20 mA at ambient temperature. The capacitor under transient and pulsed response was measured under a pulse sequence of 1 A (2 s) to − 0.5 A (2 s) to 0 A (1 s) to − 0.5 A (2 s). The voltage profile was recorded by a Maccor battery test system. The capacitor was also discharged under constant power mode. The capacitor was first charged to 2.5 V and held at the voltage until the current was less than 5 mA; then the capacitor was discharged at different constant power from 0.045 to 10.7 W. The voltage profile during the discharge was also recorded by a Maccor battery test system. The maximum current capability of the system was 10 A.

Results and Discussion

Impedance spectroscopy measurements (EIS).— EIS spectrum analysis in Fig. 1 shows that the frequency response of the EC capacitor is similar to that of the Warburg element in series with an inductive element and an ohmic resistance. The inductive behavior (20 kHz–632 Hz) is attributed to leads from the measurement setup and the spirally wound structure of the capacitors; the ohmic resistance is observed at the Z' intercept of the real axis, and the Warburg

* Electrochemical Society Active Member.
[a] Also at Center for Advance Power Systems, Florida State University, Tallahassee, Florida 32310, USA.
[z] E-mail: zheng@eng.fsu.edu

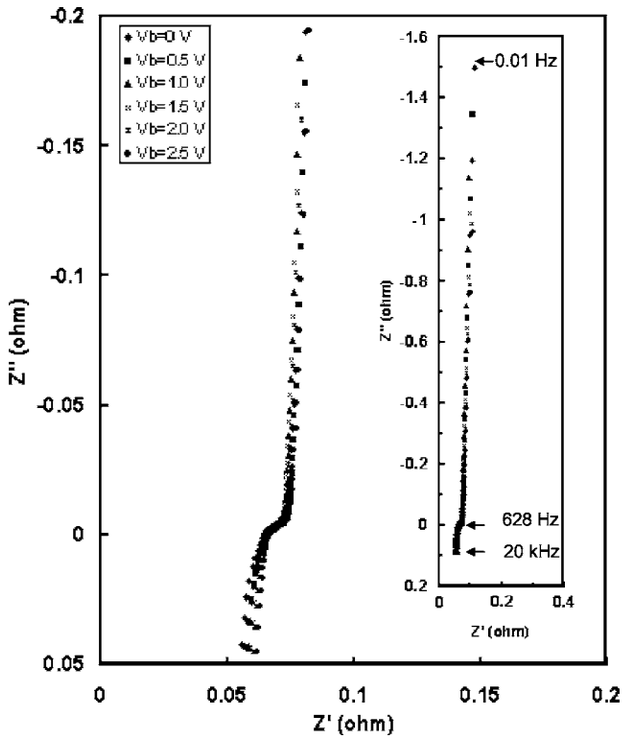

Figure 1. Ac impedance spectra at different bias voltages.

element (632 Hz–10 mHz) with ~45° slope line represents the Warburg diffusion followed by a vertical line (~90°) that represents the accumulation of charge.

The impedance of the EC capacitor in the frequency domain can be represented by a series combination of inductor L, ohmic resistance R_o, and a Warburg impedance element Z_W shown in Fig. 2; in this model it is assumed that the Warburg element exhibits purely capacitive behavior at low frequencies. The response of the Warburg element in the frequency domain is given by the following formula[31]

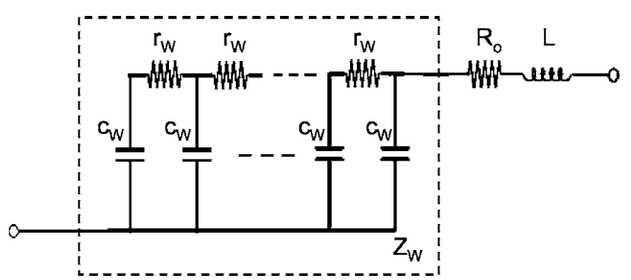

Figure 2. Electrochemical capacitor equivalent circuit model in the frequency domain.

$$Z(j\omega) = \frac{\tau}{C_W}\frac{\coth(\sqrt{j\omega\tau})}{\sqrt{j\omega\tau}} \quad [1]$$

$\tau = R_W C_W$, R_W and C_W are the sum of resistance and capacitance of the Warburg element shown in Fig. 2, respectively. For a porous electrode, R_W represents the effective resistance for ion transporting through the electrode, and C_W represents the total double-layer capacitance of the electrode. The experimental results measured at different bias voltages could be fitted well by an equivalent circuit model. From the fitting, three important parameters were obtained including the ohmic resistance $R_o = 0.0655\ \Omega$, the ionic resistance of the electrode $R_W = 0.033\ \Omega$, and the total capacitance of the electrodes, C_W, which was found to increase with increasing the bias voltage from 10.57 F at 0 V to 16.37 F at 2.5 V. These parameters will also be used to simulate the voltage profiles under pulsed current discharge and energy-power relationship of the capacitor. The inductance was also obtained and was about 0.757 μH_3; however, it will not significantly affect the simulation results since the inductor value is small and its behavior can only be significant at high frequencies, e.g., above 632 Hz. Table I summarizes the resistance and capacitance obtained from the fitting of experimental EIS at different bias voltages.

DC charge-discharge characterization.— From the result of dc charge-discharge cycling, Fig. 3, it can be seen that the *V-t* profile is triangular, with little variation in slope during charge-discharge; this indicates good capacitance characteristic with minimal variation in capacitance within this potential window. Based on the discharge portion of the *V-t* curve the capacitance was calculated using the equation as expressed below

$$C_{dl} = \frac{\Delta Q}{\Delta V} = \frac{i \times \Delta t}{\Delta V} \quad [2]$$

where i is the instantaneous discharge current, ΔV is the potential step and Δt is the differential discharge time. The internal resistance of the EC capacitor which is denoted by the equivalent series resistance is determined from the transition between charge and discharge on the *V-t* curve and is given by

$$R_{ESR} = \frac{\Delta V}{\Delta I} = \frac{\Delta V}{2I} \quad [3]$$

where ΔV is the change in voltage and I is the magnitude of charge and discharge current. The factor of 2 is because the current was switched from $+I$ to $-I$ at charge and discharge modes, respectively. The variation of capacitance with bias voltage was also obtained from the dc measurement and is listed in Table I. It can be seen that within the bias voltage range 0–2.5 V the capacitance increased from a minimum of 14.62 F at 0 V to a maximum of 16.64 F at 2.5 V. At the beginning of discharge (Fig. 3b) there is a sudden transition in potential between charge-discharge. Using Eq. 3 an equivalent series resistance of 0.075 Ω was deduced from this transition.

To compare results obtained from EIS and dc charge-discharge, it can be seen that for both methods, values of capacitance and ohmic resistance can be obtained; however, the ionic resistance of the electrode can only obtained from the EIS method. The effects of R_W from the dc charge-discharge curve can be observed during the tran-

Table I. Summary of resistance and capacitance measured at different bias voltages.

Bias voltage (V)	0	0.5	1.0	1.5	2.0	2.5
R_o (Ω)	0.0655	0.0661	0.0642	0.0637	0.0642	0.0655
R_W (Ω)	0.0361	0.0282	0.0337	0.0332	0.0335	0.0355
C_W (*F*)	10.40	11.60	13.76	15.32	15.89	16.36
C_{dl} (*F*)	14.72	14.16	14.51	15.31	15.91	15.57

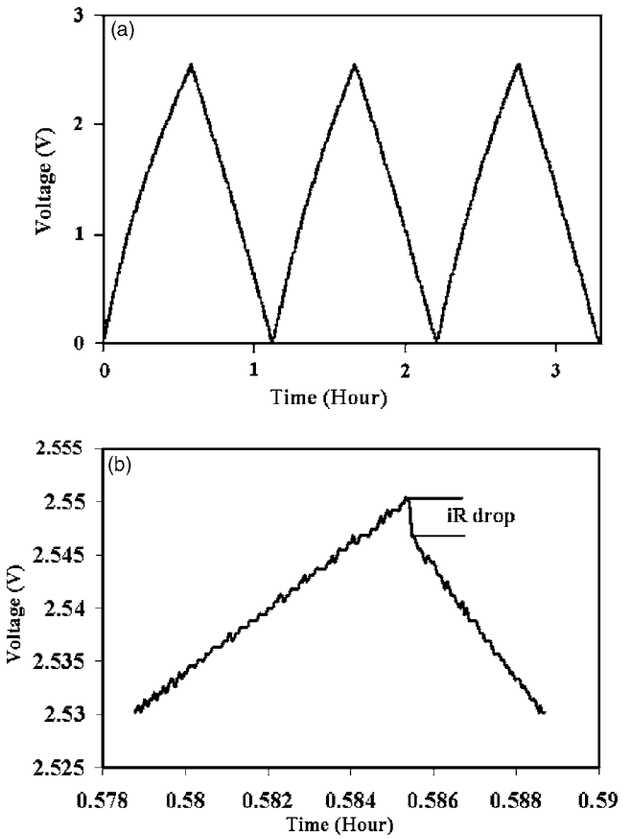

Figure 3. Dc charge and discharge curves at constant current of 20 mA.

sition between charge and discharge on the *V-t* curve as shown in Fig. 3b. The curvature after a sharp voltage drop was due to the ionic resistance of the electrode. A comparison of capacitance obtained by two different methods is shown in Fig. 4. It can be seen that the capacitance value agree well at bias voltages higher than 1 V, however, the capacitance obtained from EIS is lower than that obtained from dc charge-discharge at bias voltages lower than 1 V. The possible explanation for the difference is that a very slow pseudocapacitance reaction occurred at one of electrodes in the capacitor, because it was found that the total capacitance estimated

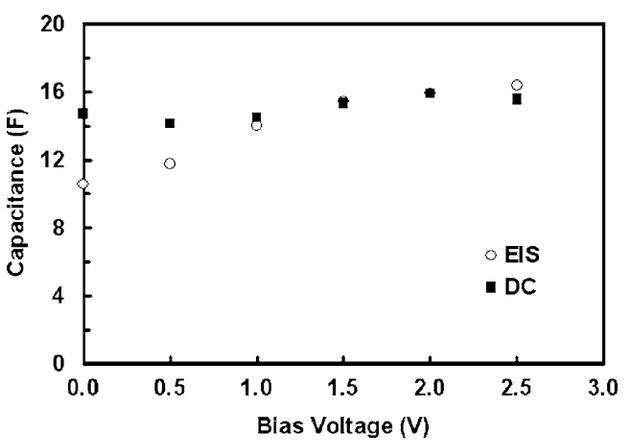

Figure 4. The values of capacitance as function of bias voltage measured by ac impedance spectra and dc charge and discharge.

based on the accumulated charge at low frequency increased with decreasing frequency, even at <10 mHz. The total capacitance was approximated by following equation

$$C_{dl} \approx \frac{1}{\omega Z''} \quad [4]$$

where ω is the frequency in rad/s and Z'' is the imaginary component of the impedance in the complex plane.

Modeling system in time domains.— A time domain representation of the equivalent circuit can be obtained by taking the inverse transformation of the impedance spectra in frequency domain. According to Mauracher, the transformation or equivalent time domain representation (Eq. 4) can be represented by[32,33]

$$\frac{k_1}{\sqrt{j\omega}} \coth\left(\frac{k_2}{k_1}\sqrt{j\omega}\right) \bullet\!-\!\circ \frac{k_1^2}{k_2} + \frac{2k_1^2}{k_2}\sum_{n=1}^{\infty} e^{-(n^2\pi^2 k_1^2/k_2^2)t} \quad [5]$$

Comparing the parameters in Eq. 4 and left side of Eq. 5 resulted in

$$k_1 = \frac{\sqrt{\tau}}{C_W} = \sqrt{\frac{R_W}{C_W}} \quad [6]$$

and

$$k_2 = \frac{\tau}{C_W} = R_W \quad [7]$$

Then considering the impulse response for a parallel *RC* circuit given below by Eq. 8 and Eq. 5 it can be concluded that the Warburg element in the frequency domain has an equivalent time domain representation and can be expressed as a series combination of parallel resistive and capacitive elements[34]

$$\frac{1/C}{j\omega + 1/RC} \bullet\!-\!\circ \frac{1}{C} e^{-t/RC} \quad [8]$$

Also from Eq. 5, it is defined as

$$C_o = \frac{k_2}{k_1^2} = C_W \quad [9]$$

Then, comparing Eq. 5 and 8 equates to the capacitance in each parallel branch given by Eq. 10

$$C_n = \frac{k_2}{2k_1^2} = \frac{C_o}{2} \quad [10]$$

It can also be deduced from Eq. 5, 8, and 10 that

$$R_n = \frac{2\tau}{n^2\pi^2 C_o} = \frac{2R_W}{n^2\pi^2} \quad [11]$$

Finally, Fig. 5 shows the equivalent circuit of the EC capacitor in the time domain. The circuit includes a Warburg equivalent network, a series ohmic resistance R_o, and an inductive contribution *L*. Note that the leakage resistance is ignored in this model. The Warburg equivalent element represents diffusion into the porous electrode using a series/parallel *RC* network.

Transient response.— Figure 6 shows the voltage profile of EC capacitor in response to a sequence of pulse currents of 1 A (2 s) and −0.5 A (2 s). The equivalent circuit model of Fig. 5 was applied using an experimental current input to stimulate the voltage profile. For the modeling using an equivalent circuit model as shown in Fig. 5, consider the condition when the EC capacitor is under constant-current load discharge, then the voltage around the loop results in a terminal load voltage given by

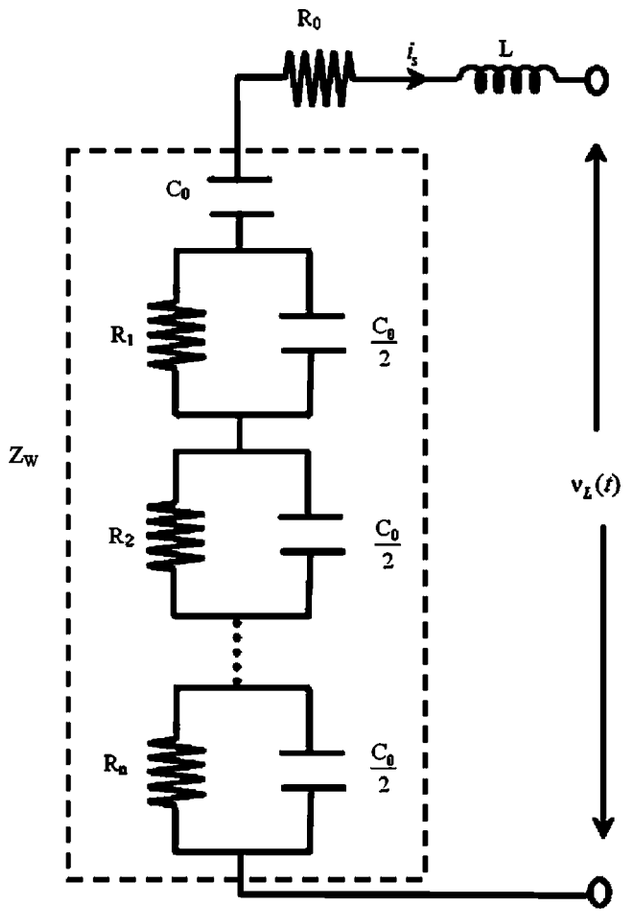

Figure 5. Electrochemical capacitor equivalent circuit model in the time domain.

$$v_L(t) = V_W - i_s R_o - L\frac{di_s}{dt} \quad [12]$$

where, i_s is the current through the capacitor, V_W is the voltage across the Warburg equivalent network and is given by

$$V_W = \sum_{n=0}^{N} V_n \quad [13]$$

The voltage on the capacitor C_o is the given by

$$V_o = V_i - \frac{1}{C_o}\int_0^t i_s(t)dt \quad [14]$$

where V_i is the initial voltage on the double-layer capacitor, C_o, The current in each parallel RC network is then given by

$$i_c = i_W - i_p \quad [15]$$

and

$$i_p = \frac{V_n}{R_n} \quad [16]$$

where i_c and i_p are the currents in the parallel RC network, respectively. The voltage on each parallel capacitor is then given by

$$V_n = -\frac{2}{C_o}\int_0^t i_c(t)dt \quad [17]$$

The stimulated V-t profile was obtained using Matlab/Simulink and is also plotted in Fig. 5 to compare with the experimental results. It is clearly seen that the simulated terminal voltage shows good agreement with the terminal voltage from the experimental. Buller et al.[33] have successfully applied the transmission line model to a practical load with much more dramatically current profile.

Power performance.— Figure 7 shows the V-t profiles of an EC capacitor discharged at constant power mode. Due to the maximum current limitation of the test system, the discharge process was stopped before the capacitor reached the voltage of zero. The total time for discharge was obtained based on the fitting curve using a polynomial as shown in Fig. 7. The energy density as a function of power density (Ragone plot) can be obtained and is plotted in Fig. 8. Experimentally, at low power densities such as $<W/L$, the deliverable energy density is about 1.3 Wh/L; when the power density is greater than W/L, the deliverable energy density drops rapidly.

To simulate the Ragone plot for a constant power (P) load connect to the EC capacitor, the active power drawn results in a terminal voltage given by

$$v_L(t) = \frac{P}{i_s(t)} \quad [18]$$

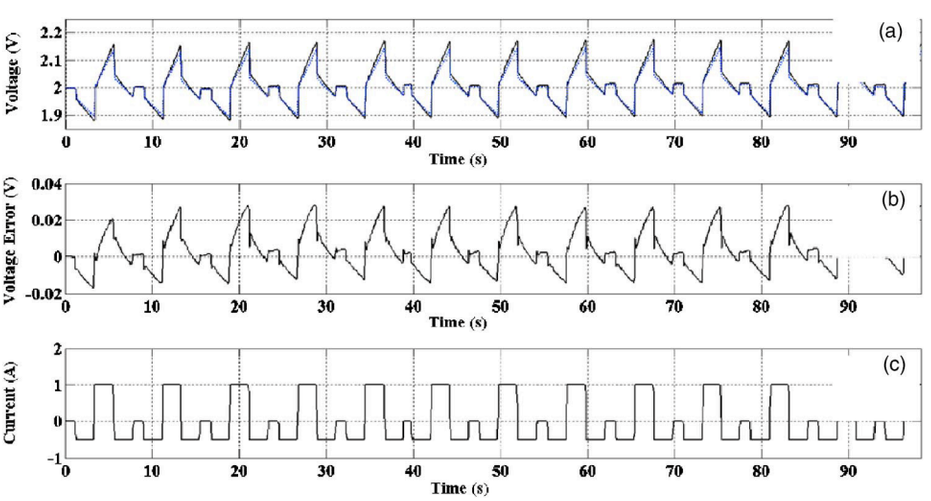

Figure 6. Comparison of (a) simulation capacitor and experimental terminal voltage in response to the pulsed current. The voltage difference between simulation and experimental is shown in (b), the current profile is shown in (c).

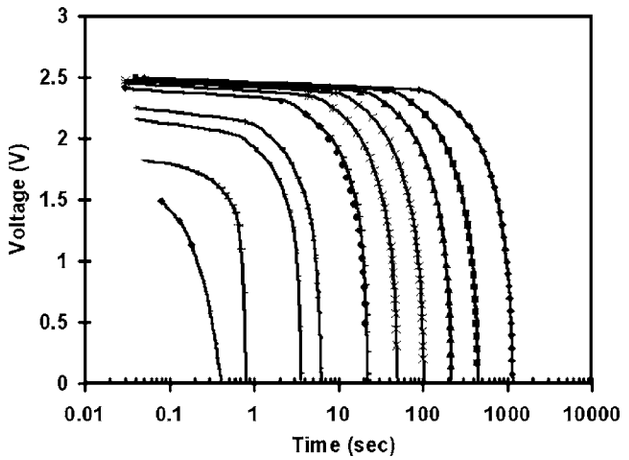

Figure 7. The voltage profile for the EC capacitor discharged at different powers. The line is a theoretical fitting using polynomial curves.

The same set of Eq. 12-17 was used during the simulation, but the current i_s was not constant and was determined by Eq. 18. The stimulated Ragone plot was also plotted in Fig. 8 in order to compare with the experimental results. During the stimulation, constant values of $R_o = 0.0665\ \Omega$ and $R_W = 0.033\ \Omega$ were used; however, a voltage dependent capacitance C_W was used. The capacitance values were determined by EIS measurement and linear fitting within two data points as shown in Table I. It can be seen that at low power density, the simulated result agrees well with the experimental result; however, at high power density, $> W/L$, the deliverable energy density was lower than the projected values by the equivalent circuit model. It is believed that the lower value obtained from the experimental power density is due to ionic depletion in the porous electrode. The total weight of electrolyte in EC capacitor was measured and is about 3.84 g. It is assumed that the salt concentration of the electrolyte is 0.75 M/L. The total available charge from the electrolyte is about 234 C if it assumes 100% solvation. When the EC capacitor was fully charged to 2.5 V, the number of cations and anions, which are equivalent to charge of about 40 C would be accumulated at the double layer of the negative and positive electrodes, respectively. The change of such a small number of ions should not affect the ionic resistance of the capacitor. It was also proven from the resistance measurements at different bias voltages. Both ohmic and ionic resistances in the electrode are almost constant in a voltage range of 0 and 2.5 V. However, it must be pointed out that when the capacitor was charged or discharged rapidly, the ion concentration and ionic resistance in the EC capacitor were not uniformly distributed, particularly in the electrode, which is dependent on the thickness of the electrode and pore size of activated carbon. Therefore, it is believed that at high power discharge and charge conditions, for these carbon surfaces with small pore size, the ion diffusion process was too slow that ion was either over saturated or depleted.

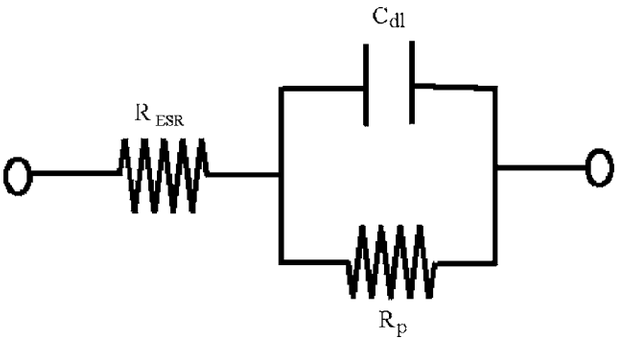

Figure 9. The first order approximation for EC capacitor equivalent circuit.

Effect of ionic resistance to power performance.— The EC capacitor voltage behavior in response to a dynamic current profile is commonly modeled using the simple equivalent first order circuit shown in Fig. 9. This circuit consists of three passive circuit elements that result in a first order approximation of the dynamic response of the EC capacitor. The circuit includes an equivalent series resistance, R_{ESR}, that represents the energy lost due to the distributive resistance of the electrolyte, electronic contacts and the porous separator; a double layer capacitance C_{dl}; and an equivalent leakage resistance, R_p, that represents the long term capability of the capacitor to maintain charge. Figure 10 shows the Ragone plots stimulated by a simple *RC* circuit model (R_p was ignored) and transmission line circuit model as shown in Fig. 5. For simplicity, a constant value of C_W was used. To compare Ragone plots obtained by the two different models, it can be seen that when $R_o \gg R_W$, the simple *RC* circuit model will be good enough to describe the energy and power relationship of the EC capacitor; however, when $R_o < R_W$, the *RC* circuit model cannot accurately project the maximum power density of EC capacitors, which is limited by ionic resistance of R_W. From Fig. 10, it can also be seen that when R_o is reduced, the points at which

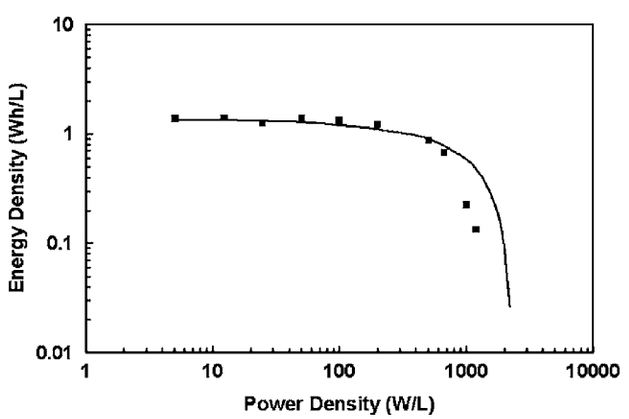

Figure 8. Ragone plot of EC capacitor. The data points and the line obtained from experiment and stimulation using equivalent circuit model, respectively.

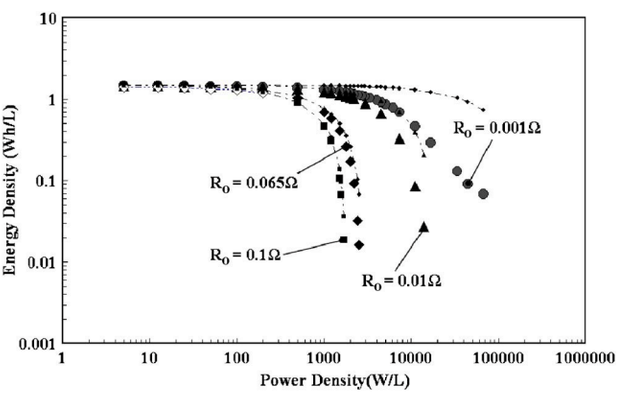

Figure 10. Stimulated Ragone plots using simple *RC* circuit (with small symbol) and transmission line circuit (with large symbol) models. For both models, the capacitance of 14 F was used and ohmic resistances were varied as indicated. The R_W for transmission line mode is 0.033 Ω.

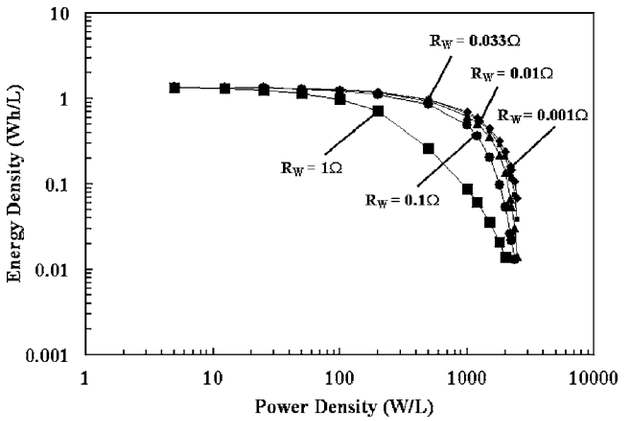

Figure 11. Stimulated Ragone plots for various Warbury resistance R_W. The capacitance and ohmic resistance are 14 F and 0.066 Ω, respectively.

the energy density starts to decline, increase with decreasing R_o, resulting in the increase in ultimate power density.

Figure 11 shows stimulated Ragone plots for the fixed R_o but variable R_W. It can be seen that when R_W increased, the energy density decreased; however, the ultimate power density was determined by the ohmic resistance (R_o) only. The relationship between the Ragone plots shown in Fig. 10 and 11 can be understood by the equivalent circuit shown in Fig. 2. The charges are stored in capacitors which formed the transmission line network. When charge is stored or released from the capacitors, they all must pass through the ohmic resistor R_o; therefore, the value of R_o would determine the ultimate power density of EC capacitors. Charge stored or released from various capacitors in the transmission line network passes through a different number of resistors in series as shown in Fig. 2. For the capacitors c_W that are closest to R_o less resistance is available to block charge storage or release than those capacitors some distance away from R_o. The greater value of r_W means that the current decays faster along the capacitor distribution in the transmission line. Therefore, the ionic resistance influences the energy density of the EC capacitor.

Conclusion

An equivalent circuit model for EC capacitors was obtained from the impedance spectra and simulated in Matlab/Simulink. The result shows that accurate simulation of the terminal voltage under dynamic load current and constant power load can be achieved. The result also verifies the effectiveness of using computer aided design based tools in obtaining good estimates of the performance of EC capacitors under various load conditions. Additionally, the effect of ion concentration change and depletion in porous electrode and separator paper can also be incorporated into the simulation. From Fig. 8, an effective way to simulate the Ragone plot at constant power over a range of energy densities for arbitrary EC capacitors is demonstrated. The advantages are cost, time, and optimization of cell design and performance.

Acknowledgments

This work was partially support by the U.S. Army CERDEC.

Florida A&M University and Florida State University assisted in meeting the publication costs of this article.

References

1. E. Karden, S. Ploumen, B. Fricke, T. Miller, and K. Snyder, *J. Power Sources*, **168**, 2 (2007).
2. J. N. Marie-Francoise, H. Gualous, R. Outbib, and A. Berthon, *J. Power Sources*, **143**, 275 (2005).
3. R. Kötz and M. Carlen, *Electrochim. Acta*, **45**, 2483 (2000).
4. J. M. Miller, D. Nebrigic, and M. Everett, *Proceedings of the 16th International Seminar on Double Layer Capacitors*, p. 22, Deerfield Beach, Florida, Dec. 4–6, 2006.
5. A. Burke, *J. Power Sources*, **91**, 37 (2000).
6. J. P. Zheng, S. P. Ding, and T. R. Jow, *IEEE Trans. Aerosp. Electron. Syst.*, **37**, 288 (2001).
7. D. Qu, *J. Power Sources*, **109**, 403 (2002).
8. J. Chmiola, G. Yushin, Y. Gogotsi, C. Portet, P. Simon, and P. L. Taberna, *Science*, **313**, 1760 (2006).
9. R. K. Dash, A. Nikitin, and Y. Gogotsi, *Microporous Mesoporous Mater.*, **72**, 203 (2004).
10. H. Nakamura and M. Okamura, *Proceedings of the 13th International Seminar on Double Layer Capacitors*, Florida Educational Seminars Inc. (2003).
11. J. P. Zheng and T. R. Jow, *J. Electrochem. Soc.*, **142**, L6 (1995).
12. J. P. Zheng, *Electrochem. Solid-State Lett.*, **2**, 359 (1999).
13. S.-L. Kuo, J.-F. Lee, and N.-L. Wu, *J. Electrochem. Soc.*, **154**, A34 (2007).
14. S.-Y. Wang, K.-C. Ho, S.-L. Kuo, and N.-L. Wu, *J. Electrochem. Soc.*, **153**, A75 (2006).
15. C. Lin, J. A. Ritter, and B. N. Popov, *J. Electrochem. Soc.*, **146**, 3155 (1999).
16. K.-C. Liu and M. A. Anderson, *J. Electrochem. Soc.*, **143**, 124 (1996).
17. G. G. Amatucci, F. Badway, A. DuPasquier, and T. Zheng, *J. Electrochem. Soc.*, **148**, A930 (2001).
18. S. M. Lipka, D. E. Reisner, J. Dai, and R. Cepulis, *Proceedings of the 11th International Seminar on Double Layer Capacitors*, Florida Educational Seminars Inc. (2001).
19. A. Laforgue, P. Simon, J. F. Fauvarque, J. F. Sarrau, and P. Lailler, *J. Electrochem. Soc.*, **148**, A1130 (2001).
20. T. Aida, I. Murayama, K. Yamada, and M. Morita, *J. Power Sources*, **166**, 462 (2007).
21. S. Nohara, T. Asahina, H. Wada, N. Furukawa, H. Inoue, N. Sugoh, H. Iwasaki, and C. Iwakura, *J. Power Sources*, **157**, 605 (2006).
22. J. P. Zheng, J. Huang, and T. R. Jow, *J. Electrochem. Soc.*, **144**, 2026 (1997).
23. J. P. Zheng and T. R. Jow, *J. Electrochem. Soc.*, **144**, 2417 (1997).
24. J. P. Zheng, *J. Electrochem. Soc.*, **150**, A484 (2003).
25. X. Wang and J. P. Zheng, *J. Electrochem. Soc.*, **151**, A1683 (2004).
26. J. P. Zheng, *J. Electrochem. Soc.*, **152**, A1864 (2005).
27. J. P. Zheng, *J. Power Sources*, **137**, 158 (2004).
28. J. P. Zheng and Z. N. Jiang, *J. Power Sources*, **156**, 748 (2006).
29. B. Pillay and J. Newman, *J. Electrochem. Soc.*, **143**, 1806 (1996).
30. T. Christen and C. Ohler, *J. Power Sources*, **110**, 107 (2002).
31. *Impedance Spectroscopy*, J. P. Macdonald, Editor, Wiley, New York (1987).
32. P. Mauracher, Ph.D. Thesis, RWTH Aachen, Germany (1996).
33. S. Buller, E. Karden, D. Kok, and R. W. De Doncker, *IEEE Trans. Ind. Appl.*, **38**, 1622 (2002).
34. J. David Irwin, *Basic Engineering Circuit Analysis*, 8th ed., Wiley, New York (2005).

REFERENCES

1. Tarascon, J.M. and M. Armand, *Issues and challenges facing rechargeable lithium batteries.* Nature, 2001. **414**(6861): p. 359-367.

2. Macdonald, D.D., *Reflections on the history of electrochemical impedance spectroscopy.* Electrochimica Acta, 2006. **51**(8-9): p. 1376-1388.

3. Arora, P., R.E. White, and M. Doyle, *Capacity fade mechanisms and side reactions in lithium-ion batteries.* Journal of the Electrochemical Society, 1998. **145**(10): p. 3647-3667.

4. Vetter, J., et al., *Ageing mechanisms in lithium-ion batteries.* Journal of Power Sources, 2005. **147**(1-2): p. 269-281.

5. Weinstock, I.B., *Recent advances in the US Department of Energy's energy storage technology research and development programs for hybrid electric and electric vehicles.* Journal of Power Sources, 2002. **110**(2): p. 471-474.

6. Dixon Lloyd, P.I., Kulick Jonathan, *Driving Emissions to Zero*. 2002, Rand Science and Technology: Santa Monica, CA. p. 1-8.

7. Simonis, D.A. and C. Hertzenberg, eds. *Lives & Legacies*. 1999, Orxy Press: Phoenix. 256.

8. Daintith, J., *A Dictionary of Scientist*. 1999: Oxford; New York Oxford University Press (UK). 463.

9. McNeil, I., *An Encyclopaedia of the History of Technology*. 2002, London: New York Routledge. 1033.

10. Chang, R., *Chemistry*. 5th ed. 1994: McGraw Hill Companies. 543.

11. Fu, L.J., et al., *Surface modifications of electrode materials for lithium ion batteries.* Solid State Sciences, 2006. **8**(2): p. 113-128.

12. Endo, M., et al., *Recent development of carbon materials for Li ion batteries.* Carbon, 2000. **38**(2): p. 183-197.

13. Rydh, C.J. and B. Svard, *Impact on global metal flows arising from the use of portable rechargeable batteries.* Science of the Total Environment, 2003. **302**(1-3): p. 167-184.

14. Ministry of Economy, T.a.I. *Secondary battery sales statistics by value*. 2006 [cited.

15. Heitner, K.L., *The search for the better polymer electrolyte.* Journal of Power Sources, 2000. **89**(2): p. 128-131.

16. Kim, H.S., P. Periasamy, and S.I. Moon, *Electrochemical properties of the Li-ion polymer batteries with P(VdF-co-HFP)-based gel polymer electrolyte.* Journal of Power Sources, 2005. **141**(2): p. 293-297.

17. Choi, N.S., Y.G. Lee, and J.K. Park, *Effect of cathode binder on electrochemical properties of lithium rechargeable polymer batteries.* Journal of Power Sources, 2002. **112**(1): p. 61-66.

18. Miller, T.J., *Lithium ion battery automotive applications and requirements*, in *Battery Conference on Applications and Advances, 2002. The Seventeenth Annual*. 2002, IEEE: Long Beach, CA, USA. p. 113-118.

19. Espinosa, D.C.R. and J.A.S. Tenorio, *Recycling of nickel-cadmium batteries - Thermogravimetric behavior of electrodes.* Journal of Power Sources, 2006. **160**(1): p. 744-751.

20. Reddy, B.R., D.N. Priya, and K.H. Park, *Separation and recovery of cadmium(II), cobalt(II) and nickel(II) from sulphate leach liquors of spent Ni-Cd batteries using phosphorus based extractants.* Separation and Purification Technology, 2006. **50**(2): p. 161-166.

21. Rydh, C.J. and M. Karlstrom, *Life cycle inventory of recycling portable nickel-cadmium batteries.* Resources Conservation and Recycling, 2002. **34**(4): p. 289-309.

22. Choi, S.H., J. Kim, and Y.S. Yoon, *A TEM study of cycled nano-crystalline HT-LiCoO2 cathodes for rechargeable lithium batteries.* Journal of Power Sources, 2004. **135**(1-2): p. 286-290.

23. Wohlfahrt-Mehrens, M., C. Vogler, and J. Garche, *Aging mechanisms of lithium cathode materials.* Journal of Power Sources, 2004. **127**(1-2): p. 58-64.

24. Ratnakumar, B.V., M.C. Smart, and S. Surampudi, *Effects of SEI on the kinetics of lithium intercalation.* Journal of Power Sources, 2001. **97-8**: p. 137-139.

25. Galobardes, F., C. Wang, and M. Madou, *Investigation on the solid electrolyte interface formed on pyrolyzed photoresist carbon anodes for C-MEMS lithium-ion batteries* Diamond and Related Materials, 2006. **15**(11-12): p. 1930-1934.

26. Osaka, T. and M. Datta, eds. *Energy Storage Systems for Electronics*. New Trends in Electrochemical Technology. Vol. 1. 2000, Taylor & Francis.

27. Park, M.-S., et al., *Si–Ni–Carbon composite synthesized using high energy mechanical milling for use as an anode in lithium ion batteries* Meterials Chemistry and physics, 2006. **100**(2-3): p. 496-502.

28. Kang, Y.M., et al., *The effect of Co-Co3O4 coating on the electrochemical properties of Si as an anode material for Li ion battery.* Electrochimica Acta, 2006. **52**(2): p. 450-454.

29. Liu, W.R., et al., *Enhanced cycle life of Si anode for Li-ion batteries by using modified elastomeric binder.* Electrochemical and Solid State Letters, 2005. **8**(2): p. A100-A103.

30. Khomenko, V.G., et al., *Lithium-ion batteries based on carbon-silicon-graphite composite anodes.* Journal of Power Sources, 2007. **165**(2): p. 598-608.

31. Dimov, N., S. Kugino, and M. Yoshio, *Carbon-coated silicon as anode material for lithium ion batteries: advantages and limitations.* Electrochimica Acta, 2003. **48**(11): p. 1579-1587.

32. Im, D. and A. Manthiram, *Lithium manganese oxide-conductive carbon nanocomposite cathodes for rechargeable lithium batteries.* Solid State Ionics, 2003. **159**(3-4): p. 249-255.

33. Sivaprakash, S., et al., *Crystal chemistry modification of lithium nickel cobalt oxide cathodes for lithium ion rechargeable batteries.* Journal of Power Sources, 2007. **170**(2): p. 433-440.

34. Spahr, M.E., et al., *Characterization of layered lithium nickel manganese oxides synthesized by a novel oxidative coprecipitation method and their*

electrochemical performance as lithium insertion electrode materials. Journal of the Electrochemical Society, 1998. **145**(4): p. 1113-1121.

35. Yi, S.B., H.T. Chung, and H.G. Kim, *A novel preparation method of active materials for the lithium secondary battery.* Electrochemistry Communications, 2007. **9**(4): p. 591-595.

36. Ohzuku, T. and R.J. Brodd, *An overview of positive-electrode materials for advanced lithium-ion batteries* Journal of Power Sources, 2007. **174**(2): p. 449-456.

37. Ritchie, A.G., et al., *Future cathode materials for lithium rechargeable batteries.* Journal of Power Sources, 1999. **80**(1-2): p. 98-102.

38. Bin Park, S., et al., *An alternative method to improve the electrochemical performance of a lithium secondary battery with LiMn2O4.* Journal of Power Sources, 2007. **166**(1): p. 219-225.

39. Alcantara, R., et al., *X-ray diffraction and electrochemical impedance spectroscopy study of zinc coated LiNi0.5Mn1.5O4 electrodes.* Journal of Electroanalytical Chemistry, 2004. **566**(1): p. 187-192.

40. Suresh, P., A.K. Shukla, and N. Munichandraiah, *Capacity stabilization of layered Li0.9Mn0.9Ni0.1O2 cathode material by employing ZnO coating.* Materials Letters, 2005. **59**(8-9): p. 953-958.

41. Aurbach, D., et al., *Design of electrolyte solutions for Li and Li-ion batteries: a review.* Electrochimica Acta, 2004. **50**(2-3): p. 247-254.

42. Scrosati, B., *Recent advances in lithium ion battery materials.* Electrochimica Acta, 2000. **45**(15-16): p. 2461-2466.

43. Ye, H., et al., *Li ion conducting polymer gel electrolytes based on ionic liquid/PVDF-HFP blends.* Journal of the Electrochemical Society, 2007. **154**(11): p. A1048-A1057.

44. Aurbach, D., et al., *A short review of failure mechanisms of lithium metal and lithiated graphite anodes in liquid electrolyte solutions.* Solid State Ionics, 2002. **148**(3-4): p. 405-416.

45. Soo, P.P., et al., *Rubbery block copolymer electrolytes for solid-state rechargeable lithium batteries.* Journal of the Electrochemical Society, 1999. **146**(1): p. 32-37.

46. Blazejczyk, A., et al., *Novel solid polymer electrolytes with single lithium-ion transport.* Journal of the Electrochemical Society, 2004. **151**(10): p. A1762-A1766.

47. Schalkwijk, W.V. and B. Scrosati, eds. *Advances in Lithium-ion Batteries*. 2002, Kluwer Academic/Plenum Publisher 36.

48. Abe, T., et al., *Lithium ion transfer at the interface between lithium-ion-conductive solid crystalline electrolyte and polymer electrolyte.* Journal of the Electrochemical Society, 2004. **151**(11): p. A1950-A1953.

49. Jeon, J.D., S.Y. Kwak, and B.W. Cho, *Solvent-free polymer electrolytes - I. Preparation and characterization of polymer electrolytes having pores filled with viscous P(EO-EC)/LiCF3SO3.* Journal of the Electrochemical Society, 2005. **152**(8): p. A1583-A1589.

50. Song, J.Y., Y.Y. Wang, and C.C. Wan, *Review of gel-type polymer electrolytes for lithium-ion batteries.* Journal of Power Sources, 1999. **77**(2): p. 183-197.

51. Aoki, T. and T. Fujinami, *Lithium ion conductivity of polymer electrolytes based on insoluble lithium tetrakis(pentafluorobenzenethiolato)borate and poly(ethylene oxide).* Journal of the Electrochemical Society, 2005. **152**(12): p. A2352-A2356.

52. Jiang, G.X., et al., *Lithium-polymer electrolytes based on polyurethane acrylate prepared by a solvent-free method.* Journal of the Electrochemical Society, 2004. **151**(11): p. A1886-A1890.

53. Kanevskii, L.S. and V.S. Dubasova, *Degradation of lithium-ion batteries and how to fight it: A review.* Russian Journal of Electrochemistry, 2005. **41**(1): p. 1-16.

54. Kerlau, M., et al., *Studies of local degradation phenomena in composite cathodes for lithium-ion batteries.* Electrochimica Acta, 2007. **52**(17): p. 5422-5429.

55. Kumaresan, K., et al., *Cycle life performance of lithium-ion pouch cells.* Journal of Power Sources, 2006. **158**(1): p. 679-688.

56. Aurbach, D., et al., *On the correlation between surface chemistry and performance of graphite negative electrodes for Li ion batteries.* Electrochimica Acta, 1999. **45**(1-2): p. 67-86.

57. Kong, F., et al., *In situ studies of SEI formation.* Journal of Power Sources, 2001. **97-8**: p. 58-66.

58. Zane, D., A. Antonini, and M. Pasquali, *A morphological study of SEI film on graphite electrodes.* Journal of Power Sources, 2001. **97-8**: p. 146-150.

59. Li, J., et al., *Studies on the cycle life of commercial lithium ion batteries during rapid charge-discharge cycling.* Journal of Power Sources, 2001. **102**(1-2): p. 294-301.

60. Yuan, X., et al., *Ac Impedance technique in PEM fuel cell diagnosis - A review.* International Journal of hydrogen Energy, 2007. **32**(1): p. 4365-4380.

61. Huang, Q.A., et al., *A review of AC impedance modeling and validation in SOFC diagnosis.* Electrochimica Acta, 2007. **52**(28): p. 8144-8164.

62. Fan, J. and P.S. Fedkiw, *Electrochemical impedance spectra of full cells: Relation to capacity and capacity-rate of rechargeable Li cells using LiCoO2, LiMn2O4, and LiNiO2 cathodes.* Journal of Power Sources, 1998. **72**(2): p. 165-173.

63. Oldham, H.B. and J.C. Myland, *Fundamental of Electrochemical Science*. 1994, New York: Academic Press, INC. 474.

64. Zhang, D., B.N. Popov, and R.E. White, *Modeling lithium intercalation of a single spinel particle under potentiodynamic control.* Journal of the Electrochemical Society, 2000. **147**(3): p. 831-838.

65. Yu, P., et al., *Ni-composite microencapsulated graphite as the negative electrode in lithium-ion batteries - II. Electrochemical impedance and self-discharge studies.* Journal of the Electrochemical Society, 2000. **147**(6): p. 2081-2085.

66. Conway, B.E., *Electrochemical Supercapacitor: Scientific Fundamental and Technology Applications*. 1999, New York: Kluwer Academic/ Plenum Publisher 698.

67. Kotz, R. and M. Carlen, *Principles and applications of electrochemical capacitors.* Electrochimica Acta, 2000. **45**(15-16): p. 2483-2498.

68. Qu, D.Y. and H. Shi, *Studies of activated carbons used in double-layer capacitors.* Journal of Power Sources, 1998. **74**(1): p. 99-107.

69. Armstrong, R.D. and B.R. Horrocks, *The double layer structure at the metal-solid electrolyte interface.* Solid State Ionics, 1997. **94**(1-4): p. 181-187.

70. Torres, A., R. van Roij, and G. Tellez, *Finite thickness and charge relaxation in double-layer interactions.* Journal of Colloid and Interface Science, 2006. **301**(1): p. 176-183.

71. Varela, M.L., M. Garcia, and V. Mosquera, *Extract mean-field theory of ionic solution: Non Debye screening.* Physics Reports, 2003. **382**(1-2): p. 1-111.

72. Palasantzas, G. and G.M.E.A. Backx, *Roughness effects on the double-layer charge capacitance: the case of Helmholtz layer induced roughness attenuation.* Surface Science, 2003. **540**(2-3): p. 401-406.

73. Hendriks, M.G.H.M., et al., *The electrochemical double-layer capacitance of yttria-stabilised zirconia.* Solid State Ionics, 2002. **146**(3-4): p. 211-217.

74. Wang, Z.-W., et al., *A functional theoretical approach to the electric double layer of a spherical colloid particle.* Chemical Physics, 2001. **274**(1): p. 57-69.

75. Balbuena, B.P. and Y. Wang, *Lithium-ion Batteries: Solid-Electrolyte Interphase*. 2004, London: Imperial Press. 407.

76. Gao, J., et al., *Suppression of PC decomposition at the surface of graphitic carbon by Cu coating.* Electrochemistry Communications, 2006. **8**(11): p. 1726-1730.

77. Ein-Eli, Y., *A new perspective on the formation and structure of the solid electrolyte interface at the graphite anode of Li-ion cells.* Electrochemical and Solid State Letters, 1999. **2**(5): p. 212-214.

78. Gnanaraj, J.S., et al., *Formation and growth of surface films on graphitic anode materials for Li-ion batteries.* Electrochemical and Solid State Letters, 2005. **8**(2): p. A128-A132.

79. Peled, E., D. Golodnitsky, and G. Ardel, *Advanced model for solid electrolyte interphase electrodes in liquid and polymer electrolytes.* Journal of the Electrochemical Society, 1997. **144**(8): p. L208-L210.

80. Jung, D.Y., et al., *Development of ultracapacitor modules for 42-V automotive electrical systems.* Journal of Power Sources, 2003. **114**(2): p. 366-373.

81. Briat, O., et al., *Power cycling tests for accelerated ageing of ultracapacitors.* Microelectronics Reliability, 2006. **46**(9-11): p. 1445-1450.

82. Chu, A. and P. Braatz, *Comparison of commercial supercapacitors and high-power lithium-ion batteries for power-assist applications in hybrid electric vehicles I. Initial characterization.* Journal of Power Sources, 2002. **112**(1): p. 236-246.

83. Holland, C.E., et al., *Experimental characterization of hybrid power systems under pulse current loads.* Journal of Power Sources, 2002. **109**(1): p. 32-37.

84. Burke, A., *Ultracapacitors: why, how, and where is the technology.* Journal of Power Sources, 2000. **91**(1): p. 37-50.

85. Gao, L.J., R.A. Dougal, and S.Y. Liu, *Power enhancement of an actively controlled battery/ultracapacitor hybrid.* Ieee Transactions on Power Electronics, 2005. **20**(1): p. 236-243.

86. Taberna, P.L., P. Simon, and J.F. Fauvarque, *Electrochemical characteristics and impedance spectroscopy studies of carbon-carbon supercapacitors.* Journal of the Electrochemical Society, 2003. **150**(3): p. A292-A300.

87. Gualous, H., et al., *Experimental study of supercapacitor serial resistance and capacitance variations with temperature.* Journal of Power Sources, 2003. **123**(1): p. 86-93.

88. Qu, D.Y., *Studies of the activated carbons used in double-layer supercapacitors.* Journal of Power Sources, 2002. **109**(2): p. 403-411.

89. Chmiola, J., et al., *Anomalous increase in carbon capacitance at pore sizes less than 1 nanometer.* Science, 2006. **313**(5794): p. 1760-1763.

90. Dash, R.K., A. Nikitin, and Y. Gogotsi, *Microporous carbon derived from boron carbide.* Microporous and Mesoporous Materials, 2004. **72**(1-3): p. 203-208.

91. Nakamura, H. and M. Okamura, Proceedings of The 13th International Seminar on Double Layer Capacitors, Florida Educational Seminars, Inc. , 2003.

92. Zheng, J.P. and T.R. Jow, *A New Charge Storage Mechanism for Electrochemical Capacitors.* Journal of the Electrochemical Society, 1995. **142**(1): p. L6-L8.

93. Zheng, J.P., *Ruthenium oxide-carbon composite electrodes for electrochemical capacitors.* Electrochemical and Solid State Letters, 1999. **2**(8): p. 359-361.

94. Kuo, S.-L., J.-F. Lee, and N.-L. Wu, *Study on Pseudocapacitance Mechanism of Aqueous MnFe2O4 Supercapacitor.* Journal of the Electrochemical Society, 2007. **154**(1): p. A34-A38.

95. Wang, S.Y., et al., *Investigation on capacitance mechanisms of Fe3O4 electrochemical capacitors.* Journal of the Electrochemical Society, 2006. **153**(1): p. A75-A80.

96. Lin, C., J.A. Ritter, and B.N. Popov, *Development of carbon-metal oxide supercapacitors from sol-gel derived carbon-ruthenium xerogels.* Journal of the Electrochemical Society, 1999. **146**(9): p. 3155-3160.

97. Liu, K.C. and M.A. Anderson, *Porous nickel oxide/nickel films for electrochemical capacitors.* Journal of the Electrochemical Society, 1996. **143**(1): p. 124-130.

98. Nohara, S., et al., *Hybrid capacitor with activated carbon electrode, Ni(OH)(2) electrode and polymer hydrogel electrolyte.* Journal of Power Sources, 2006. **157**(1): p. 605-609.

99. Amatucci, G.G., et al., *An asymmetric hybrid nonaqueous energy storage cell.* Journal of the Electrochemical Society, 2001. **148**(8): p. A930-A939.

100. Lipka, S.M., et al., Proceedings of The 11th International Seminar on Double Layer Capacitors, Florida Educational Seminars, Inc., 2001.

101. Laforgue, A., et al., *Hybrid supercapacitors based on activated carbons and conducting polymers.* Journal of the Electrochemical Society, 2001. **148**(10): p. A1130-A1134.

102. Aida, T., et al., *High-energy-density hybrid electrochemical capacitor using graphitizable carbon activated with KOH for positive electrode.* Journal of Power Sources, 2007. **166**(2): p. 462-470.

103. Zheng, J.P., J. Huang, and T.R. Jow, *The limitations of energy density for electrochemical capacitors.* Journal of the Electrochemical Society, 1997. **144**(6): p. 2026-2031.

104. Zheng, J.P. and T.R. Jow, *The effect of salt concentration in electrolytes on the maximum energy storage for double layer capacitors (vol 144, pg 2417, 1997).* Journal of the Electrochemical Society, 1997. **144**(12): p. 4366-4366.

105. Zheng, J.P., *The limitations of energy density of battery/double-layer capacitor asymmetric cells.* Journal of the Electrochemical Society, 2003. **150**(4): p. A484-A492.

106. Wang, X. and J.P. Zheng, *The optimal energy density of electrochemical capacitors using two different electrodes.* Journal of the Electrochemical Society, 2004. **151**(10): p. A1683-A1689.

107. Zheng, J.P., *Theoretical energy density for electrochemical capacitors with intercalation electrodes.* Journal of the Electrochemical Society, 2005. **152**(9): p. A1864-A1869.

108. Zheng, J.P., *Resistance distribution in electrochemical capacitors with a bipolar structure.* Journal of Power Sources, 2004. **137**(1): p. 158-162.

109. Zheng, J.P. and Z.N. Jiang, *Resistance distribution in electrochemical capacitors with spiral-wound structure.* Journal of Power Sources, 2006. **156**(2): p. 748-754.

110. Pillay, B. and J. Newman, *The influence of side reactions on the performance of electrochemical double-layer capacitors.* Journal of the Electrochemical Society, 1996. **143**(6): p. 1806-1814.

111. Christen, T. and C. Ohler, *Optimizing energy storage devices using Ragone plots.* Journal of Power Sources, 2002. **110**(1): p. 107-116.

112. Spyker, R.L., R.M. Nelms, and S.L. Merryman, *Evaluation of double-layer capacitors for power electronics applications.* Predeeding of the eleventh Annual IEEE Applied Power Electronics Conference, 1996: p. 725-730.

113. Spyker, R.L. and R.M. Nelms, *Classical Equivalent Circuit Parameters for a Double -Layer Capacitor.* IEEE Transaction on Aerospace and Electronic Systems, 2000. **36**(2): p. 829-836.

114. Kim, C. and K.S. Yang, *Electrochemical properties of carbon nanofiber web as an electrode for supercapacitor prepared by electrospinning.* Applied Physics Letters, 2003. **83**(6): p. 1216-1218.

115. Mauracher, P. and E. Karden, *Dynamic modelling of lead/acid batteries using impedance spectroscopy for parameter identification.* Journal of Power Sources, 1997. **67**(1-2): p. 69-84.

116. Chen, Z.H., Q.Z. Wang, and K. Amine, *Improving the performance of soft carbon for lithium-ion batteries.* Electrochimica Acta, 2006. **51**(19): p. 3890-3894.

117. Ogumi, Z., et al., *Lithium-ion transfer at interface between carbonaceous thin film electrode/electrolyte.* Journal of Power Sources, 2004. **127**(1-2): p. 72-75.

118. Doi, T., et al., *Lithium-ion transfer at a solid polymer electrolyte/non-graphitizable carbon electrode interface.* Journal of Power Sources, 2005. **142**(1-2): p. 329-332.

119. Matoba, Y., et al., *Electrochemical properties of composite polymer electrolyte applied to rechargeable lithium polymer battery.* Journal of Power Sources, 2004. **137**(2): p. 284-287.

120. Nakamura, H., H. Komatsu, and M. Yoshio, *Suppression of electrochemical decomposition of propylene carbonate at a graphite anode in lithium-ion cells.* Journal of Power Sources, 1996. **62**(2): p. 219-222.

121. Han, Y.K., et al., *Theoretical studies of the solvent decomposition by lithium atoms in lithium-ion battery electrolyte.* Chemical Physics Letters, 2002. **360**(3-4): p. 359-366.

122. Jeong, S.K., et al., *Surface film formation on a graphite negative electrode in lithium-ion batteries: AFM study on the effects of co-solvents in ethylene carbonate-based solutions.* Electrochimica Acta, 2002. **47**(12): p. 1975-1982.

123. Zhang, S.S., et al., *Understanding solid electrolyte interface film formation on graphite electrodes.* Electrochemical and Solid State Letters, 2001. **4**(12): p. A206-A208.

124. Appetecchi, G.B., et al., *Lithium insertion into carbonaceous materials and transition metal oxides from high performance polymer electrolytes.* Electrochimica Acta, 1999. **45**(1-2): p. 23-30.

125. Doyle, M. and Y. Fuentes, *Computer simulations of a lithium-ion polymer battery and implications for higher capacity next-generation battery designs.* Journal of the Electrochemical Society, 2003. **150**(6): p. A706-A713.

126. Nishi, Y., *Lithium ion secondary batteries; past 10 years and the future.* Journal of Power Sources, 2001. **100**(1-2): p. 101-106.

127. Zhou, D.B., et al., *Electrochemical studies of LiB compound as anode material for lithium-ion battery.* Electrochimica Acta, 2006. **51**(26): p. 5731-5737.

128. Rodrigues, S., N. Munichandraiah, and A.K. Shukla, *AC impedance and state-of-charge analysis of a sealed lithium-ion rechargeable battery.* Journal of Solid State Electrochemistry, 1999. **3**(7-8): p. 397-405.

129. Wu, M.S. and P.C.J. Chiang, *High-rate capability of lithium-ion batteries after storing at elevated temperature.* Electrochimica Acta, 2007. **52**(11): p. 3719-3725.

130. Abe, T., et al., *Solvated Li-ion transfer at interface between graphite and electrolyte.* Journal of the Electrochemical Society, 2004. **151**(8): p. A1120-A1123.

131. Ramadass, P., et al., *Development of first principles capacity fade model for Li-ion cells.* Journal of the Electrochemical Society, 2004. **151**(2): p. A196-A203.

132. Levi, M.D., et al., *Solid-state electrochemical kinetics of Li-ion intercalation into Li1-xCoO2: Simultaneous application of electroanalytical techniques SSCV, PITT, and EIS.* Journal of the Electrochemical Society, 1999. **146**(4): p. 1279-1289.

133. Gabrisch, H., R. Yazami, and B. Fultz, *A transmission electron microscopy study of cycled LiCoO2.* Journal of Power Sources, 2003. **119**: p. 674-679.

134. Levi, M.D., Z. Lu, and D. Aurbach, *Application of finite-diffusion models for the interpretation of chronoamperometric and electrochemical impedance responses of thin lithium insertion V2O5 electrodes.* Solid State Ionics, 2001. **143**(3-4): p. 309-318.

135. Zheng, M.S., et al., *Formation and influence factors of solid electrolyte interphase film on the negative electrode surface in lithium-ion batteries.* Journal of the Electrochemical Society, 2005. **152**(11): p. A2207-A2210.

136. Yoshida, T., et al., *Degradation mechanism and life prediction of lithium-ion batteries.* Journal of the Electrochemical Society, 2006. **153**(3): p. A576-A582.

137. Christensen, J. and J. Newman, *Effect of anode film resistance on the charge/discharge capacity of a lithium-ion battery.* Journal of the Electrochemical Society, 2003. **150**(11): p. A1416-A1420.

138. Kwon, K., et al., *Characterization of the SEI on a carbon film electrode by combined EQCM and spectroscopic ellipsometry.* Journal of the Electrochemical Society, 2003. **150**(2): p. A229-A233.

139. Wang, H.F., et al., *Electron microscopic characterization of electrochemically cycled LiCoO2 and Li(Al,Co)O-2 battery cathodes.* Journal of Power Sources, 1999. **82**: p. 594-598.

140. Li, J., et al., *The effects of pulse charging on cycling characteristics of commercial lithium-ion batteries.* Journal of Power Sources, 2001. **102**(1-2): p. 302-309.

141. Kanamura, K., et al., *Preparation and electrochemical characterization of LiCoO2 particles prepared by supercritical water synthesis.* Electrochemical and Solid State Letters, 2000. **3**(6): p. 256-258.

142. Chen, Y.F. and J.W. Evans, *3-Dimensional Thermal Modeling of Lithium-Polymer Batteries under Galvanostatic Discharge and Dynamic Power Profile.* Journal of the Electrochemical Society, 1994. **141**(11): p. 2947-2955.

143. Doyle, M., J.P. Meyers, and J. Newman, *Computer simulations of the impedance response of lithium rechargeable batteries.* Journal of the Electrochemical Society, 2000. **147**(1): p. 99-110.

144. Wu, M.S., P.C.J. Chiang, and J.C. Lin, *Electrochemical investigations on advanced lithium-ion batteries by three-electrode measurements.* Journal of the Electrochemical Society, 2005. **152**(1): p. A47-A52.

145. Abraham, D.P., et al., *Performance degradation of high-power lithium-ion cells-Electrochemistry of harvested electrodes.* Journal of Power Sources, 2007. **170**(2): p. 465-475.

146. Takano, K., et al., *Simulation study of electrical dynamic characteristics of lithium-ion battery.* Journal of Power Sources, 2000. **90**(2): p. 214-223.

147. Ning, G., R.E. White, and B.N. Popov, *A generalized cycle life model of rechargeable Li-ion batteries.* Electrochimica Acta, 2006. **51**(10): p. 2012-2022.

148. Doyle, M., et al., *Comparison of modeling predictions with experimental data from plastic lithium ion cells.* Journal of the Electrochemical Society, 1996. **143**(6): p. 1890-1903.

149. Kuhn, E., C. Forgez, and G. Friedrich, *Modeling diffusion phenomena using non integer derivatives.* The European Physical Journal Applied Physics, 2004. **25**: p. 183-190.

150. Buller, S., et al., *Impedance-based simulation models of supercapacitors and Li-ion batteries for power electronic applications.* Ieee Transactions on Industry Applications, 2005. **41**(3): p. 742-747.

151. Moss, P.L., et al., *Transmission line model for describing power performance of electrochemical capacitors.* Journal of the Electrochemical Society, 2007. **154**(11): p. A1020-A1025.

152. Dokko, K., et al., *Electrochemical impedance study of Li-ion insertion into mesocarbon microbead single particle electrode Part II. Disordered carbon.* Electrochimica Acta, 2001. **47**(6): p. 933-938.

153. Chen, C.H., J. Liu, and K. Amine, *Symmetric cell approach and impedance spectroscopy of high power lithium-ion batteries.* Journal of Power Sources, 2001. **96**(2): p. 321-328.

154. Mohamedi, M., et al., *Explicit analysis of impedance spectra related to thin films of spinel LiMn2O4.* Journal of Power Sources, 2001. **93**(1-2): p. 93-103.

155. Chan, S.H., K.A. Khor, and Z.T. Xia, *A complete polarization model of a solid oxide fuel cell and its sensitivity to the change of cell component thickness.* Journal of Power Sources, 2001. **93**(1-2): p. 130-140.

156. Buller, S., et al., *Impedance-based non-linear dynamic battery modeling for automotive applications.* Journal of Power Sources, 2003. **113**(2): p. 422-430.

157. R.de, L., *Electrochemistry response of porous and rough electrodes*. Advances In Electrochemistry and Electrochemical Engineering. Vol. 6. 1967, New York, London, Sydney: Wiley Interscience. 329-397.

158. Karden, E., S. Buller, and R.W. De Doncker, *A frequency-domain approach to dynamical modeling of electrochemical power sources.* Electrochimica Acta, 2002. **47**(13-14): p. 2347-2356.

159. Levi, M.D., et al., *On electrochemical impedance measurements of LixCo0.2Ni0.8O2 and LixNiO2 intercalation electrodes.* Electrochimica Acta, 2000. **45**(11): p. 1781-1789.

160. Barcia, O.E., et al., *Application of the impedance model of de Levie for the characterization of porous electrodes.* Electrochimica Acta, 2002. **47**(13-14): p. 2109-2116.

161. Li, H., X.J. Huang, and L.Q. Chen, *Electrochemical impedance spectroscopy study of SnO and nano-SnO anodes in lithium rechargeable batteries.* Journal of Power Sources, 1999. **82**: p. 340-345.

162. Kim, J.S. and Y.T. Park, *Characteristics of surface films formed at a mesocarbon microbead electrode in a Li-ion battery.* Journal of Power Sources, 2000. **91**(2): p. 172-176.

163. Cui, N. and J.L. Luo, *An AC impedance study of self-discharge mechanism of nickel-metal hydride (Ni-MH) battery using Mg2Ni-type hydrogen storage alloy anode.* Electrochimica Acta, 2000. **45**(24): p. 3973-3981.

164. Lijun, G., L. Shengyi, and R.A. Dougal, *Dynamic lithium-ion battery model for system simulation.* IEEE Transaction on Component and Packaging Technologies, 2002. **25**(3): p. 495-505.

165. Piller, S., M. Perrin, and A. Jossen, *Methods for state-of-charge determination and their applications.* Journal of Power Sources, 2001. **96**(1): p. 113-120.

166. Christen, T. and M.W. Carlen, *Theory of Ragone plots.* Journal of Power Sources, 2000. **91**(2): p. 210-216.

167. Barsoukov, E., et al., *Universal battery parameterization to yield a non-linear equivalent circuit valid for battery simulation at arbitrary load.* Journal of Power Sources, 1999. **83**(1-2): p. 61-70.

168. Letellier, M., et al., *The first in situ Li-7 nuclear magnetic resonance study of lithium insertion in hard-carbon anode materials for Li-ion batteries.* Journal of Chemical Physics, 2003. **118**(13): p. 6038-6045.

169. Gerald, R.E., et al., *In situ nuclear magnetic resonance investigations of lithium ions in carbon electrode materials using a novel detector.* Journal of Physics-Condensed Matter, 2001. **13**(36): p. 8269-8285.

170. Chevallier, F., et al., *In situ Li-7-nuclear magnetic resonance observation of reversible lithium insertion into disordered carbons.* Electrochemical and Solid State Letters, 2003. **6**(11): p. A225-A228.

171. Fu, R., et al., *High Resolution 7Li Solid-State NMR Study of LixV2O5 Cathode Electrodes for Li-Rechargeable Batteries.* Journal of Physical Chemistry, B, 2003. **107**: p. 9730-9730.

172. Pecquenard, B., D. Gourier, and N. Baffier, *Epr Identification of Lixv2o5 Phases Generated by Chemical and Electrochemical Lithium Intercalation in V2o5.* Solid State Ionics, 1995. **78**(3-4): p. 287-303.

BIOGRAPHICAL SKETCH

Pedro L. Moss received his Bachelors of Science degree in Electrical Engineering from Florida State University in the fall 2000. He furthered his education under the supervision of Dr. Jim P. Zheng and obtained his Masters of Science degree in the fall 2003. He continued to work toward the completion of his Doctor of Philosophy degree with emphasis on characterization of lithium-polymer batteries and modeling the charge-discharge and power performance of energy storage devices. During this time he worked as a graduate research assistant in the Power Sciences laboratory under the direct supervision of Dr. Jim P. Zheng. During this time he also worked as a graduate teacher's assistant in the department of Electrical and Computer Engineering.